



Title	Exploring the near-field properties on coupled plasmonic nanostructures by photoemission electron microscopy
Author(s)	于, 瀚
Citation	北海道大学. 博士(情報科学) 甲第12817号
Issue Date	2017-06-30
DOI	10.14943/doctoral.k12817
Doc URL	http://hdl.handle.net/2115/66530
Type	theses (doctoral)
File Information	Han_Yu.pdf



[Instructions for use](#)

Exploring the Near-Field Properties on Coupled Plasmonic
Nanostructures by Photoemission Electron Microscopy

Thesis by

Han Yu

In Partial Fulfillment of the Requirements

for the Degree of

Doctor of Philosophy



DIVISION OF BIOENGINEERING AND BIOINFORMATICS

GRADUATE SCHOOL OF INFORMATION SCIENCE AND

TECHNOLOGY

HOKKAIDO UNIVERSITY

SAPPORO, JAPAN

2017

Dedication

DEDICATED

TO

MY FAMILY

Table of Contents

Acknowledgements	iv
Thesis Abstract	vi
Chapter 1	1
Introduction	1
1.1 Background and motivation	1
1.2 Surface plasmon resonances	2
1.3 Plasmon coupling of localized surface plasmon resonances	4
1.3.1 Near-field coupling	5
1.3.2 Far-field coupling	7
1.4 Plasmon hybridization and Fano resonances on coupled plasmonic nanostructures	9
1.4.1 Plasmon hybridization	9
1.4.2 Fano resonances	11
1.5 Near field probing techniques	16
1.5.1 Scanning near-field optical microscopy (SNOM)	17
1.5.2 Cathodoluminescence (CL) and electron energy-loss spectroscopy (EELS)	21
1.5.3 Photoemission electron microscopy (PEEM)	26
1.6 Aim and outline of this thesis	33
1.7 References	34
Chapter 2	50
Localized surface plasmon resonance in simple nanostructures probed from near field and the fundamental applications of PEEM	50
2.1 Abstract	50
2.2 Introduction	51

2.3	Experimental details	52
2.3.1	Sample fabrication and characterization.....	52
2.3.2	Near-field measurements	53
2.3.3	Numerical simulations	56
2.3.4	Time-resolved PEEM setup	56
2.4	Results and discussion	59
2.4.1	Characterization of topography and far-field spectra	59
2.4.2	Near-field mapping	60
2.4.3	Near-field spectra	63
2.4.4	Numerical simulation results	64
2.4.5	Dynamics of localized surface plasmon resonance investigated by time-resolved PEEM	66
2.5	Conclusions	72
2.6	References	73
Chapter 3	76
Plasmon hybridization in coupled dolmen structures.....		76
3.1	Abstract.....	76
3.2	Introduction	77
3.3	Experimental details	80
3.4	Results and discussion	82
3.4.1	Characterization of topography and far-field spectra	82
3.4.2	Near-field spectra of Au dolmen structure	85
3.4.3	Near-field mapping of Au dolmen structure.....	88
3.4.4	Finite-difference time-domain simulation results.....	90
3.4.5	Spatially resolved photoemission intensity spectra	93
3.4.6	Discussions	95
3.5	Conclusions	97
3.6	References	98

Chapter 4	102
Far-field coupling and the grating effect in coupled plasmonic nanostructures.....	102
4.1 Abstract.....	102
4.2 Introduction	103
4.3 Experimental details	106
4.4 Results and discussion.....	107
4.4.1 Far-field coupling and grating effect in nanoblock structures.....	107
4.4.2 Far-field coupling and grating effect in coupled dolmen structures.....	110
4.4.3 Far-field coupling and grating effect in complex heptamer structures...	116
4.4.4 Summary and discussions.....	118
4.5 Conclusions	123
4.6 References	124
Chapter 5	126
Conclusions and future perspectives	126
5.1 Conclusions	126
5.2 Future perspectives	129
List of Publications.....	131

Acknowledgements

I would like to express my special appreciation and greatly acknowledge to my supervisor, Prof. Hiroaki Misawa. He gave me the chance for studying in his lab with such good experimental environment. During my doctoral course in his lab, he was always encouraging my research and gave me excellent advices for my experiments. His guidance not only help to develop a positive attitude in performing difficult research, but also deep into my life. He has been a tremendous mentor for me. I would also like to greatly thank Prof. Kosei Ueno for the continuous support, patience, and a lot of advices for my experiments. He taught me how important of the carefulness in working, life, and everything. I would also like to thank Prof. Tomoya Oshikiri for his scientific advice and many insightful discussions and suggestions. He is so kind and helps me at any time I needed. I would also like to express my special thanks to Prof. Quan Sun. During my doctoral course working with him, he has taught me a lot of knowledge and helped me both in research and the life here. He is always kind and patient to me when I need help. And he encouraged me a lot when I met difficulties in research and life. I can say he is the man who leads me to the magical world of surface plasmon. It is my pleasure to work with you. Thanks to their careful and friendly supervision, helps, and advices, I have learnt a lot in these years. Without their constant trust and gentle prodding, this thesis would not have been completed.

I would like to give special thanks to Ms. Yumiko Yamaguchi, who helped me a lot for the documents preparation all the time with her patience and carefulness. Sincere thanks go to Prof. Xu Shi, who taught me the usages of the experimental setups and helped to solve problems in the experiments when I first came to this laboratory. Special thanks also go to Dr. Yuqing Zhong, who helped me in study and life. We came to Japan together and had so much memorable experience in Japan together.

I would also like to express my deep gratitude to other laboratory members, Dr.

Hiyori Uehara, Dr. Jie Li, Dr. Olivier Lecarme, Dr. Ahamed shalan, Mr. Jingchun Guo, Mr. Keisuke Nakamura, Mr. Xiaolong Yang, Mr. Hiroki Sawayanagi, Ms. Ririka Masunaga, Mr. Takaya Tokiwa, Mr. Sho Nozawa, Mr. Yuki Matsuzuka and Mr. Yoshiomi Kamata, Mr. Ryohei Takakura, Mr. Takeshi Mikami, Mr. Kotaro Nakagawa, Mr. Shouhei Yamashita, Ms. Hana Nakamura, Mr. Akira Murayama, Mr. Hiroaki Yamada. They were all very kind to me and helped me a lot about the experiments and also the life here. They are wonderful and generous colleagues and partners. It has been a pleasure working with you. I appreciate help of Mr. Ko Onishi from the research support department for facilities maintenance and their meticulous guidance. I would also like to thank all of my friends who supported me and incited me to strive towards my goal.

I am indebted to the China Scholarship Council (CSC) for their generous funding, which removed financial concerns from my decision to embark on this journey.

As a final note, I owe special thanks to my family. Words cannot express how grateful I am to my parents for all of the sacrifices that they have made for me. Thank you very much for your patient, comprehension and supporting all the time. I would also like to greatly thank to my wife. With your company and supporting, life is so much easier when life gets hard. Specially appreciate to my little baby daughter. Thank you so much for coming to this world and to be my daughter. Your birth is the most wonderful thing in the world. I dedicate this thesis to them.

Thesis Abstract

In the past few decades, the optical properties of localized surface plasmon resonances (LSPRs) that occur on metallic nanoparticles (NPs) have attracted more and more research interests due to the wide applications in many fields. The LSPRs lead to intense light scattering and absorption around the plasmon resonant wavelength in the far field and local field enhancement in the near field. Recent advances in synthesis and nanofabrication techniques allow for the fabrication of metallic NPs with nanometric accuracy and complex shapes. The complex plasmonic NPs that resemble NPs with small gap distance can be fabricated. Complex plasmonic NPs can induce plasmon coupling that may result in greater local field enhancement; they also exhibit some striking properties such as plasmon hybridization, Fano resonance, and electromagnetically induced transparency. So far, optical properties of the complex coupled plasmonic NPs have been characterized mainly by far-field spectroscopy and numerical simulations. Spectral response and field distribution of the coupled plasmonic NPs remain largely unexplored experimentally. This thesis aims at the investigation of near-field spectral property and near-field mapping of the coupled plasmonic NPs using photoemission electron microscopy (PEEM).

First I described the development of multiphoton PEEM in probing the near field of the plasmonic NPs. I elucidated how PEEM can be applied to obtain the near-field mapping and the near-field spectra using simple gold (Au) nanoblock structures as an example. I obtained the near-field mapping of the Au nanoblock structures with high spatial resolution. The near-field spectra were obtained by excitation wavelength dependent PEEM measurements. Selective excitation of dipole and quadrupole plasmon modes was demonstrated by manipulating the polarizations of the oblique incidence light. Additionally, the dynamics of the LSPRs was investigated by time-resolved PEEM using an interferometric pump-probe technique. In particular, it was

demonstrated that the quadrupole mode has longer dephasing time than the dipole mode. (Chapter 2)

I further apply PEEM in more complex coupled plasmonic nanostructures. I selected Au dolmen nanostructures, which have been investigated by several groups as a typical coupled plasmonic system. The spectral property of dolmen structures was previously explained by the Fano resonance as the result of interference between a spectral wide bright dipole plasmon mode and a narrow dark quadrupole mode. However, in this study, I clarified that the spectral response of dolmen structures is primarily attributable to the bonding and anti-bonding plasmon modes resulted from plasmon hybridization. This attribution was supported by near-field spectra measured by PEEM. I obtained the spatially resolved near-field spectral response of dolmen structures and observed that the maximum near-field enhancement is dominated by the bonding and anti-bonding modes. Distinct near-field intensity distribution can be found for different plasmon modes. Based on these results, I further discuss the crossover between plasmon hybridization and Fano resonance in coupled plasmonic nanostructures. (Chapter 3)

The pitch size of a regular two-dimensional array of metallic nanoparticles plays an important role in the plasmonic properties of the array due to the far-field plasmon coupling between nanoparticles. In particular, when the pitch size is comparable to the plasmon resonant wavelength, the grating effect can alter the resonant wavelength and the dephasing time of plasmon resonance. I also examined the effect of the far-field coupling and especially the grating effect on complex Au dolmen structures from the view point of near-field response measured by PEEM. The results demonstrated that the two hybridized plasmon modes on Au dolmen structures could be modified by the grating effect. For comparison, the grating effects in arrays of simple Au nanoblock structures and complex heptamer structures which support a strong bright plasmon mode and a dark plasmon mode, respectively, have also been investigated. The spectral response of the two hybridized plasmon modes on the dolmen structures as the pitch size changed evolved in a manner similar to that of the bright dipole mode on the

nanoblock structures could be observed, whereas the dark mode on the heptamer structures is less sensitive to the pitch size. (Chapter 4)

Herein, the near-field properties on different kinds of Au plasmonic nanostructures have been investigated by using PEEM. Near-field mapping in nanometer resolution and near-field spectral properties of various plasmonic NPs were measured. The results revealed that the dipole mode, quadrupole mode, and even plasmon coupling mode could be measured by PEEM. Otherwise, the different plasmon modes have been demonstrated that they have different sensitivity to the far-field coupling and grating effect. Furthermore, the results demonstrated that the near-field spectrum can be used to distinguish the crossover between plasmon hybridization and Fano resonance. The investigations deepen our understanding of the LSPRs on plasmonic nanostructures and will help for optimizing the design of the structures and developing plasmon-based applications. The work present in this thesis further demonstrates the great potential of PEEM as a promising technique for plasmonics.

Keywords: localized surface plasmon resonance, near-field imaging, plasmon hybridization, Fano resonance, photoemission electron microscopy, femtosecond laser pulses.

Chapter 1

Introduction

1.1 Background and motivation

Localized surface plasmon resonances (LSPRs) that occur on metallic nanoparticles (NPs) are collective oscillations of the conduction electrons which are confined to the surfaces of the metallic NPs. Under the light excitation with the resonant wavelength, metallic NPs exhibit intense light absorption and scattering in the far field, and local field enhancement in the near field due to the LSPRs. The optical properties of LSPRs have been the subject of intense study for the past few decades, since it have potential wide applications in various fields, including sensing,¹⁻³ imaging,^{1, 4} lasing,⁵ energy harvesting,⁶⁻⁸ surface-enhanced Raman scattering,^{9, 10} plasmon-assisted photochemical reactions,¹¹⁻¹³ photocurrent generation,^{14, 15} and artificial photosynthesis.¹⁶⁻¹⁸

Recent advances in synthesis and nanofabrication techniques allow for the preparation of metallic NPs by several methods such as chemical synthesis,¹⁹⁻²¹ electron beam lithography (EBL) together with metal deposition and lift-off process,²²⁻²⁴ and Focused ion beam (FIB) milling.²⁵ For some practical applications, the metallic NPs arranged in two-dimensional (2D) arrays are of particular interest, and they can be easily fabricated by the EBL method with nanometer precision and complex shape. Complex metallic NPs can induce plasmon coupling exhibiting some striking properties such as plasmon hybridization,^{19, 26} Fano resonance,²⁷⁻³⁴ electromagnetically induced transparency (EIT),³⁵ and plasmonic waveguiding.^{36, 37}

To date, the investigations of the optical properties of LSPRs have largely relied on far-field spectroscopic measurements or numerical simulations. However, to further understand the physical mechanism of the LSPRs and to optimize the design of the plasmonic nanostructures for the applications, the near-field properties of the LSPRs are

very essential. For example, for most LSPR based applications, the local field enhancement effect is very important. The local field enhancement sites are usually referred to the plasmonic hot spots, which are considered as the active sites for plasmon enhanced photochemical reactions and nonlinear optical process. The near-field spectra and the spatial distribution of the plasmonic hot spots are highly desired. So far, several experimental approaches have been utilized to visualize the near field, scanning near-field optical microscopy (SNOM),³⁸ electron energy loss spectroscopy (EELS), Cathodoluminescence (CL),³⁹⁻⁴¹ and some indirect methods such as plasmon-assisted nonlinear photopolymerization and the near-field ablation.⁴²⁻⁴⁷ The recent development of multiphoton photoemission electron microscopy (MP-PEEM) using femtosecond laser pulses as the excitation light source has become another powerful approach for pinpointing the near field of LSPRs with spatial and temporal resolutions.⁴⁸⁻⁶⁰

The motivation of this thesis is to employ PEEM in probing the near-field properties of the complex coupled metallic NPs in order to better understand the plasmon coupling in them. In particular, this thesis aims at determining the spatial distribution of the plasmonic hot spots of different modes and near-field spectral properties. It is expected to reveal the mechanism of the plasmon coupling in the coupled plasmonic systems and help to develop the plasmonic nanodevices.

1.2 Surface plasmon resonances

Surface plasmon resonances (SPRs) are coherent electron oscillations confined to the surfaces of conductive materials, and they are well known to play a key role in wide divisions of science, ranging from physics, chemistry and material science to biology. Although the existence of SPRs was first predicted and termed in 1957 by Ritchie,⁶¹ the first observation of SPRs can date back to 1902, when Wood's Anomalies was found in the diffraction light from a metallic grating.⁶² In general, SPRs can be classified into surface plasmon polaritons (SPPs) confined at the interface between metals and

dielectric materials and localized surface plasmon resonances supported on metallic nanoparticles, as skeptically shown in Figure 1.1.

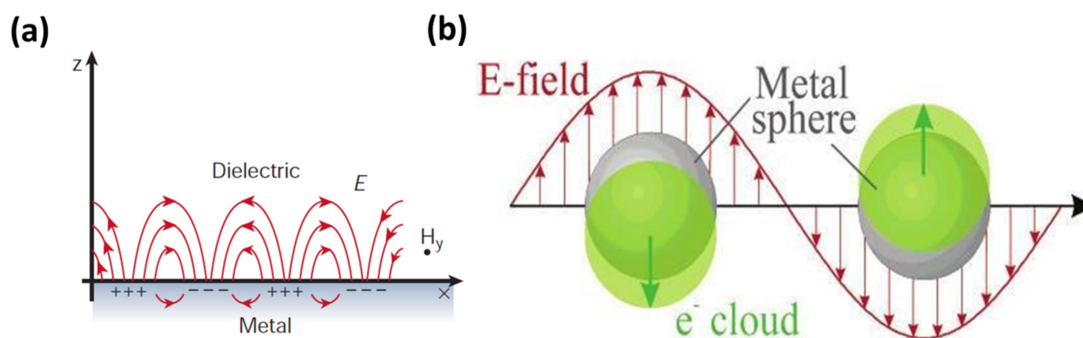


Figure 1.1 The sketch map of surface plasmon polaritons (SPPs) (a) and localized surface plasmon resonances (LSPRs) (b).^{63, 64}

SPPs are a type of surface wave, propagated along the interface in similar way as light can be guided by an optical fiber. Perpendicular to the interface, the SPPs decay very fast thus they have subwavelength-scale confinement, and they can propagate along the interface for a certain distance until their energy are lost due to either the absorption in the metal or the scattering into far field. Typically, SPPs cannot be excited on the metal surface directly by the light excitation because of the wavevector mismatch between SPPs and light. However, coupling of light into SPPs can be achieved using a coupling medium such as a prism or grating.⁶⁵⁻⁷⁰

LSPRs are collective electron oscillations in metallic NPs that can be easily excited by light. In 1904, a model has been developed to describe the colors of metal doped glasses based on the Drude theory of metals.⁷¹ This color change in metal doped glasses rely on the far-field properties of LSPRs, that is, LSPRs can enable intense light absorption or scattering at resonance wavelength. The resonance frequency and amplitude of LSPR on metallic nanostructures are known to depend on the metal materials, shapes, and surrounding media.^{1, 11, 23, 72} For typical gold (Au) or silver (Ag) NPs, the LSPRs usually occur in visible and near infrared wavelength region. In the near field, the LSPRs can confine optical fields in nanoscale space, leading to the

so-called local field enhancement effect. These unique properties promote the application of LSPRs in many fields, such as surface-enhanced Raman scattering (SERS),^{9, 10} sensing,¹⁻³ plasmon-based nonlinear optics process,^{9, 10, 73-76} photochemical reactions,¹¹⁻¹³ artificial photosynthesis,¹⁶⁻¹⁸ and photocurrent generation.^{14, 15}

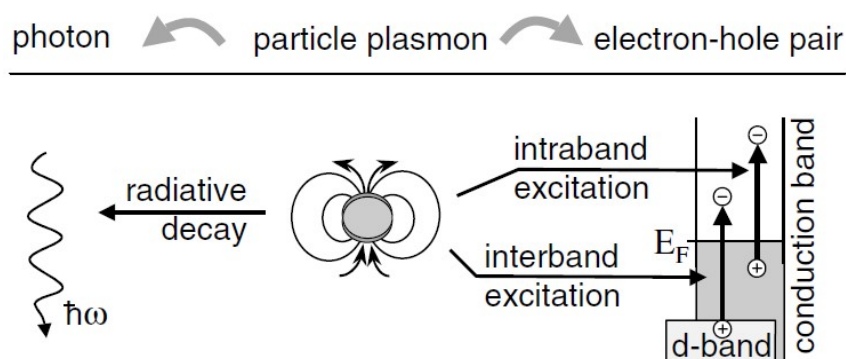


Figure 1.2 Schematic representation of radiative (left) and nonradiative (right) decay of particle plasmons in noble metallic nanostructures.⁷⁷

The LSPR field is highly localized in the spatial domain, and only can last for a certain time in the temporal domain due to the dephasing effect. The dephasing of LSPRs mainly result from the radiative damping that is the scattering loss and the nonradiative decay, which occurs via excitation of electron-hole pairs either by intraband excitation or interband excitation as exploited in Figure 1.2.⁷⁷ In most case, the longer dephasing time is beneficial for plasmonic-based applications. So far, the dephasing time can be estimated from the bandwidth of the far-field spectra or directly measured in temporal domain by pump-probe techniques.^{51, 78} For Au and Ag NPs the dephasing time is only several femtoseconds.

1.3 Plasmon coupling of localized surface plasmon resonances

When the metallic NPs arranged in two-dimensional (2D) array or a NP consists of two or more NP parts with small distances, the optical properties can be different from those of individual NPs. The optical properties can be influenced by the pitch size or the

gap distance between the NPs. Two types of the interaction between nearby NPs can be distinguished. One is the short range interaction which namely near-field coupling and another one is the long range interaction which namely far-field coupling. The optical properties can be influenced by the inter-particle distance, d , it include the gap distance in a single NP. When d is much smaller than the NP size, the interaction between adjacent NPs based on the short range of the electromagnetic field within several tens of nanometers leads the near-field coupling with d^{-3} dependence dominates. When d is larger enough comparable to the NP size and the LSPR wavelengths, the interaction of long range dipole-dipole interaction in the scattered light field leads the far-field coupling with d^{-1} dominates. Thus, the near-field coupling and far-field coupling can be switched by changing the pitch size of the 2D NP array.

1.3.1 Near-field coupling

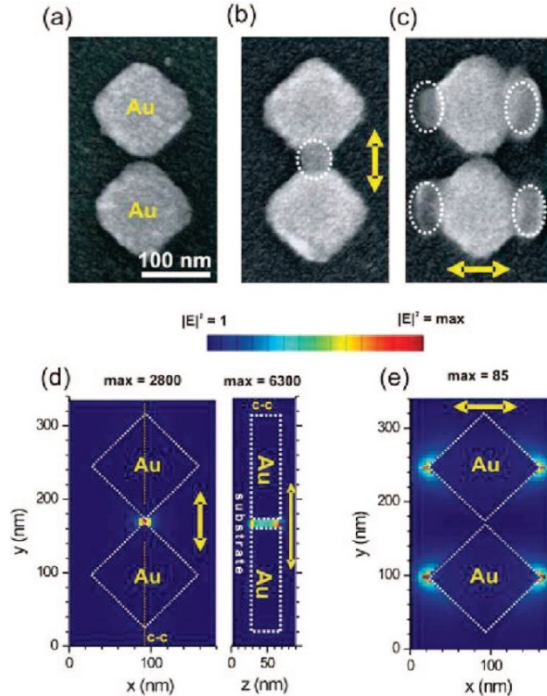


Figure 1.3 Investigation of LSPRs on coupled Au dimer structures *via* two-photon polymerization of the photoresist surrounding the nanoparticles. (a) SEM image of an Au dimer structure with the gap distance is 5.6 nm. (b) SEM image of an Au dimer after 0.01 s exposure to the laser beam under vertical polarized laser irradiation. (c) SEM

image of an Au dimer after 100 s exposure under horizontal polarized laser irradiation. (d) and (e) calculated near-field patterns at selected planes under vertical and horizontal polarization, respectively. The photopolymerized region resulting after the exposure shown in (b) indicate a strong near-field enhancement occurs at the gap position, since the small gap leads a strong near-field coupling of the two nanoblocks under the vertical polarization excitation.⁷⁹

When two metallic NPs close to each other within several tens of nanometers (smaller than the particle size), dramatic near-field coupling may occur. The electromagnetic field of one particle may interact with the electromagnetic field of nearby particle lead to a large enhancement of the LSPRs. Such near-field enhancement may modify the LSPR properties; result in the red shift of plasmon wavelength or generating some striking properties. Figure 1.3 shows the investigation results of LSPRs on coupled Au dimer structures *via* two-photon polymerization of the photoresist surrounding the nanoparticles. The dimer structure consists with two nanoblock parts with small gap distance as shown in Figure 1.3 (a). Here, the gap between the two nanoblocks is very small, only 5.6 nm. After exposure by laser excitation under vertical polarized excitation (along the long axis of the dimer structure), the photopolymer left at the gap position of dimer as shown in Figure 1.3 (b). It indicates that the gap position has stronger near-field enhancement under vertical polarized excitation. Since the small gap leads to a very strong near-field coupling between the two nanoblocks under the vertical polarized excitation, results in the strong near-field enhancement at the gap position. The huge near-field enhancement located at the gap position under vertical polarized excitation with a local enhancement factor of up to 6.3×10^3 can be obtained from the FDTD simulation as shown in Figure 1.3 (d). Such kind of strong local enhancement supported by near-field coupling on coupled plasmonic system can be applied to wide applications. In addition, due to the near-field coupling, some specific plasmon mode can also be induced.

1.3.2 Far-field coupling

Far-field coupling occurs at the large pitch size which comparable to the NP size and LSPR wavelength. It is long range interaction between the dipole-dipole interaction in the scattered field in nanoparticle arrays. Meier, Wokaunm and Liao have theoretically studied of such phenomena.⁸¹ They also found that for a 2D square grating of metal NP, particularly strong dipole interaction arises when the light fields change from evanescent to radiative in character in some particular grating order which called the grating effect.⁸¹ The grating effect is a specific kind of far-field coupling. For 2D square grating of metallic NPs, there is a critical pitch size, d_c , it decided a new diffractive radiation order emerges for a given wavelength, λ . The grating constant dc can be calculated from the following equation:

$$d_c = m\lambda / (n_1 \sin \theta + n_2)$$

where m is an integer defining the grating order, λ is the given wavelength (in plasmonic system, it can be the plasmon oscillation wavelength), θ is the light incident angle in the medium of refractive index n_1 , n_2 is the refractive index of the array substrate or free space.

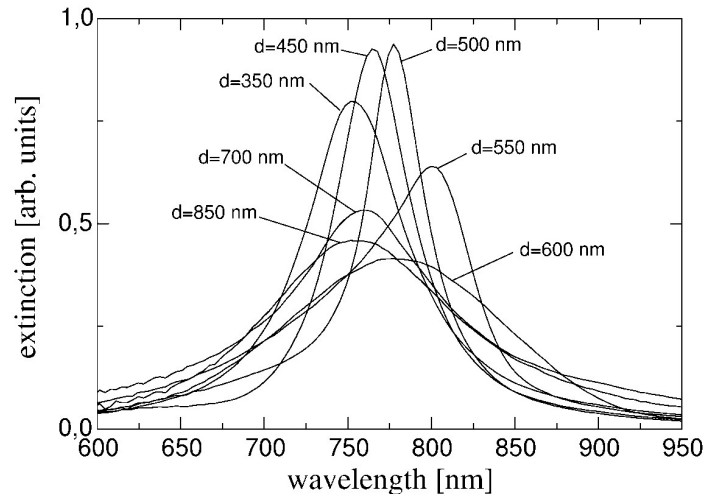


Figure 1.4 Extinction spectra for square 2D grating of Au nanodisks with different pitch sizes.⁷⁸

Lamprecht et al. have investigated the far-field coupling and grating effect on Au

nanodisks arranged in 2D patterns with different pitch sizes.⁷⁸ They found that the plasmon resonant wavelength evolves with the pitch size as shown in Figure 1.4. The plasmon peaks red shift first, then slightly blue shifts, at last red shifts again as increasing the pitch size. Furthermore, they found the extinction spectra show different bandwidths as varying the pitch sizes.⁷⁸ The results experimentally demonstrated that the pitch size of the 2D metallic nanoparticles array could influence the plasmon resonance as well as the plasmon damping dramatically.

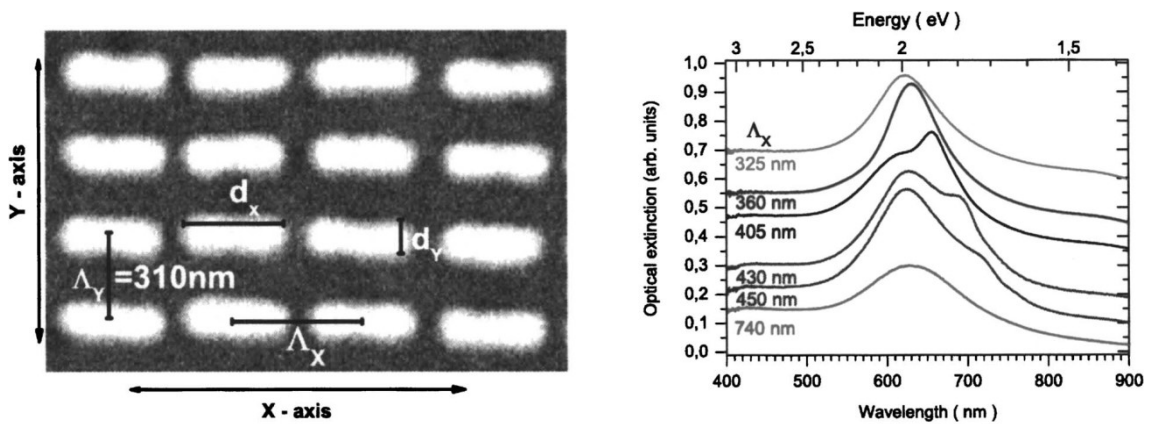


Figure 1.5 Investigation of the far-field coupling and grating effect on Au nanorod array. SEM image of Au nanorod array (left). Optical far-field extinction spectra of Au nanorod arrays with different pitch sizes.⁸²

Another research by Felidj et al. investigated the far-field coupling and grating effect on Au nanorod structures.⁸² They settled the pitch size in Y direction and changed the pitch size in X direction as can be seen in Figure 1.5. The far-field extinction spectra show that for Au nanorod structures the grating effect also influence the plasmon resonant wavelengths and broaden the plasmon peak as the pitch size close to the specific grating constant. Furthermore, new peaks can also be observed when the pitch size close to the specific grating constant. This is due to the interaction between the LSPR and the grating effects.

The two investigations mentioned above demonstrated that the far-field coupling and grating effects play a very important role in 2D metallic nanostructures since the plasmon resonance and plasmon damping can be dramatically modified by the pitch

sizes. Furthermore, due to the grating effects, not only the wavelength and bandwidth of the LSPRs can be modified, and sometimes even new modes can emerge when the pitch size is changed. To make a better design of the 2D metallic nanostructures and optimize the wavelength and bandwidth of LSPRs, it is very important to make a further investigation of the far-field coupling and grating effects.

1.4 Plasmon hybridization and Fano resonances on coupled plasmonic nanostructures

1.4.1 Plasmon hybridization

The model of “Plasmon hybridization” was firstly presented by Prodan et al. in 2003.¹⁹ Plasmon hybridization means the strong interaction between two plasmonic building blocks gives rise to hybridization of their constituent plasmonic modes, in analogy to bonding and anti-bonding combinations in the molecular orbital theory in chemistry. They used metallic nanoshell structures combined from a nano sphere and cavity to understand the plasmon hybridization model.¹⁹ Figure 1.6 shows an energy-level diagram describing the plasmon hybridization in metal nanoshells. The sphere and cavity plasmons are electromagnetic excitations that induce surface charges at the inner and outer interfaces. The plasmons of sphere and cavity interact with each other and the strong interaction results in the splitting of the plasmon resonances into two new plasmon resonances. One is the lower energy symmetric or bonding plasmon mode and another one is the higher energy antisymmetric or anti-bonding plasmon mode as shown in Figure 1.6. The original plasmon modes of sphere and cavity interacted with each other and hybridized into two new plasmon modes of plasmon hybridized bonding mode and plasmon hybridized anti-bonding mode. Using the model investigated above, the principle model of the plasmon hybridization can be described.

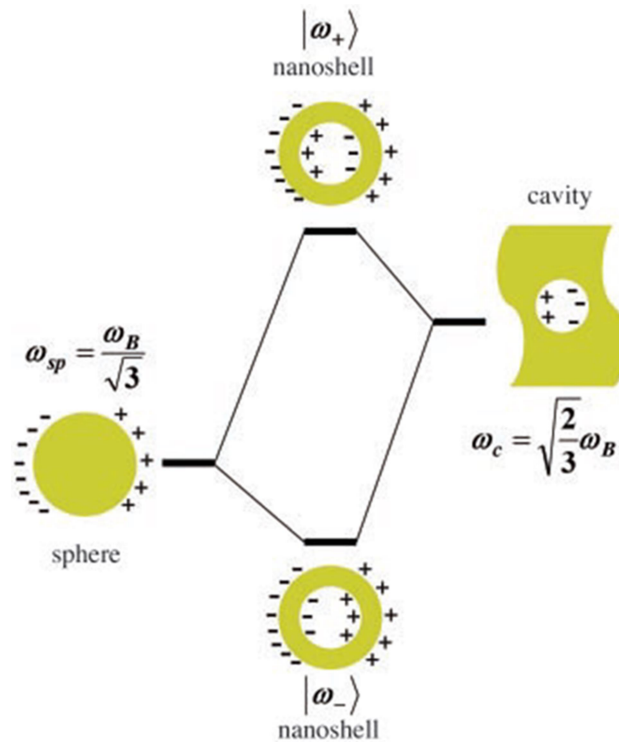


Figure 1.6 An energy-level diagram describing the plasmon hybridization in metal nanoshells resulting from the interaction between the sphere and cavity plasmons. The two nanoshell plasmons are an antisymmetrically coupled (anti-bonding) plasmon mode and a symmetrically coupled (bonding) plasmon mode.¹⁹

The plasmon hybridization model can be used to understand the plasmon response of more complex metallic NPs of “nano-matryushka” structures as shown in Figure 1.7 (a). The original far-field plasmon peaks of inner shell and outer shell can be observed from the spectra in line (1) and line (2), respectively, as shown in Figure 1.7 (b) and marked by short black lines. The interaction between the inner shell and outer shell of “nano-matryushka” structures also result in generating two new plasmon hybridized modes as shown in line (3) of Figure 1.7 (b) and the peaks are marked by short black lines. In “nano-matryushka” structures, the plasmon hybridization result in the hybridized anti-bonding mode and hybridized bonding mode that can be observed in the far field spectrum at lower energy and higher energy, respectively.

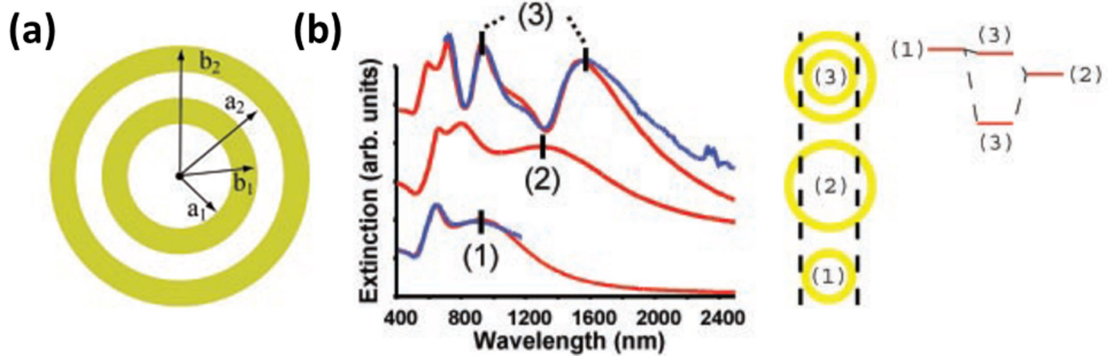


Figure 1.7 (a) Diagrams depicting the concentric nanoshell (nano-matryushka) geometry. (b) Experimental (blue) and theoretical (red) extinction spectra for concentric nanoshells (3) compared to the inner shell (1) and outer shell (2).¹⁹

In a coupled plasmonic nanostructure system which exhibit plasmon hybridization, normally the anti-bonding mode and bonding mode dominate and these two modes can be observed in far-field spectrum.⁸³⁻⁸⁵ Otherwise, in much more complex plasmonic nanostructures systems, the strong interaction between higher-order plasmon modes may result in more hybridized energy states.

1.4.2 Fano resonances

In 1935, Ugo Fano experimentally discovered a new type of resonance with a distinctly asymmetric spectral shape in the absorption profile of noble gases,⁸⁶ and he gave theoretically description of such phenomena in quantum autoionizing states of atoms in 1961.⁸⁷ He described that such phenomena was resulted from the interference between a broad continuum state with a narrow discrete state, where constructive and destructive interferences take place at the similar energy state, and results in the asymmetric spectral shape.⁸⁷ Now such phenomena bear his name which called Fano resonances. Recent investigations of Fano resonances demonstrated that the Fano resonance can be applied to explain a huge number of phenomena in various systems such as the energy-dependent line profile of absorption in molecular systems,^{88, 89} quantum dots and tunnel junctions,⁹⁰⁻⁹² the asymmetric distribution of the density in Anderson impurity systems,⁹³ bilayer graphene nanostructures,^{94, 95} the interaction of

narrow Bragg resonances with broad Mie bands in photonic crystals,^{96, 97} the transmission and reflection properties of photonic-crystal slabs,⁹⁸⁻¹⁰⁵ and terahertz metamaterials.^{34, 106-113}

The Fano resonances in plasmonic nanostructures have been the active subject over the past few years, since it is easy to generate the coherent effects.¹¹³⁻¹²² It has gained a lot of applications by the nanoscale classical oscillator systems including diffraction grating and hole or particle arrays.^{10, 25, 30, 35, 39, 80, 123-142} The Fano resonances supported by the metallic NPs arise from the interference between a spectral wide bright plasmon mode (superradiant) and a narrow dark plasmon mode (subradiant). In normal, the spectral wide bright plasmon mode corresponds to the dipole plasmon mode and the narrow dark plasmon mode corresponds to the higher-order plasmon mode such as the quadrupole mode. Large effort has been put on the design and characterization of plasmonic nanostructures exhibiting Fano resonances.^{129, 143} In previous investigation, the plasmonic Fano resonance has been investigated both theoretically and experimentally for various structures such as split rings,²² sliced disks,¹⁴⁴ dolmen structures,^{39, 80, 142} heptamer structures,^{31, 40, 145, 146} and so on.

Verellen et al. have investigated the Au dolmen structures consists of a planar nanorod monomer and a planar nanorod dimer as shown in Figure 1.8 (d).⁸⁰ They concluded that the far-field line-shape in extinction spectrum under the specific polarized light excitation (i.e. where the electric field vector is perpendicular to the symmetry axis of the dolmen structure) is attributed to the Fano resonance. Figure 1.8 (a) shows the far-field extinction spectra of plasmonic Au dolmen structures both in horizontally polarized incidence light (red) and vertically polarized incidence light (blue). Under the horizontal polarized incidence light excitation, the dipole plasmon mode of the entire structure can be excited (Figure 1.8 (e) shows the charge distribution), results in the broad dipole plasmon band. However, under the vertical excitation light, two peaks and a dip can be observed. They explained such phenomena resulted from the interference between the bright dipole plasmon mode in monomer with the dark

quadrupole plasmon mode in dimer (Figure 1.8 (f) shows the charge distribution of dip wavelength excitation). The destructive interference between the two plasmon modes leads to the Fano resonance and results in the two peaks and a dip (Fano dip) in the far-field extinction spectrum. Here the bright continuum mode is supported by the dipole mode in monomer, and the dark mode is supported by the quadrupole mode in dimer. Normally, this quadrupole mode is a forbidden mode and it cannot be excited. However, when the monomer part close to the dimer part, the dipole plasmon mode in monomer may induce the quadrupole mode in dimer part, thus make it is possible to interference with the dipole mode in monomer. The numerical simulation results shown in Figure 1.8 (b) reproduce well with the experimental results.

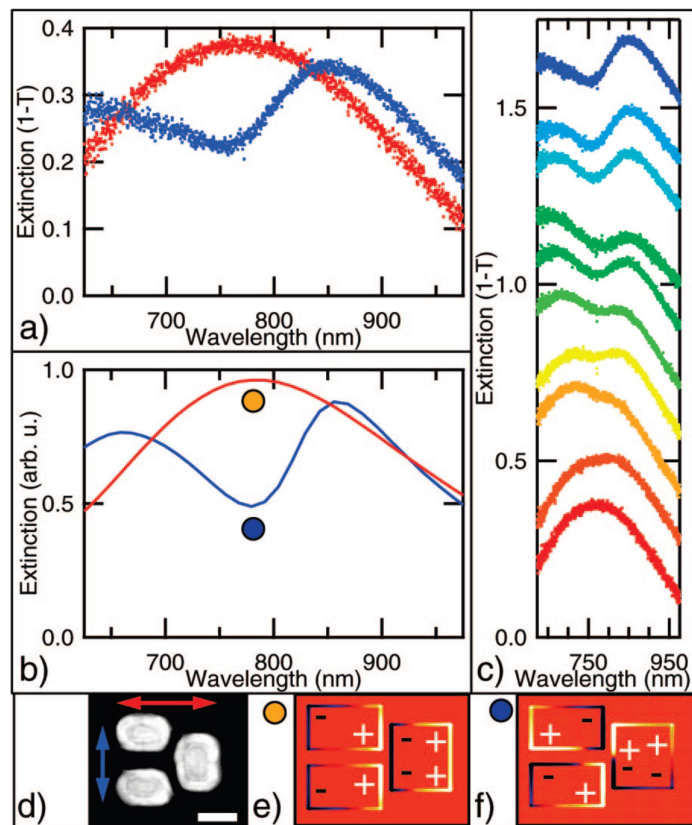


Figure 1.8 Fano resonance of an individual dolmen structures (d). (a, b) Experimentally and numerically obtained far-field extinction spectra, respectively, with horizontal (red) and vertical (blue) polarizations. (c) The evolution of the experimentally measured extinction as the polarization direction is changed. (e, f) Calculated surface charge distributions of the dipole mode and the Fano extinction dip.⁸⁰

Another family of nanostructures that can exhibit sharp Fano resonances is the

plasmonic cluster structures. As an example, Figure 1.9 shows the investigation of the Fano resonances in plasmonic heptamer structure investigated by Lassiter et al.³¹ The heptamer structure consists with seven nanodisks and they were arranged with small gaps as shown in Figure 1.9 (a). Figure 1.9 (b) and (c) shows the experimental and simulated far-field scattering spectra, respectively, in which two peaks and a dip can be observed. They attributed these phenomena to Fano resonance. The small gaps between each circle part lead the plasmon hybridization of the entire structures resulting in hybridized bonding plasmon mode (the charge in each circle parts are all in phase) and hybridized anti-bonding plasmon mode (the charge in outer six circle parts are in phase and the charge in the inner circle part is out-off phase). The interference between the superradiant plasmon mode (bonding mode) and the subradiant plasmon mode (anti-bonding mode) leads to the Fano resonance. Figure 1.10 shows the field vector distributions for shorter-wavelength peak (a), dip (b), and longer-wavelength peak (c). Under dip wavelength excitation, the field vector distribution shows an anti-phase distribution between the inner particle and the outer particles. Under the two peak wavelength excitations, the field vector distributions show the same in phase distribution of the seven particles that indicate such phenomenon arises due to the destructive interference between the superradiant and subradiant plasmon modes.^{31, 146}

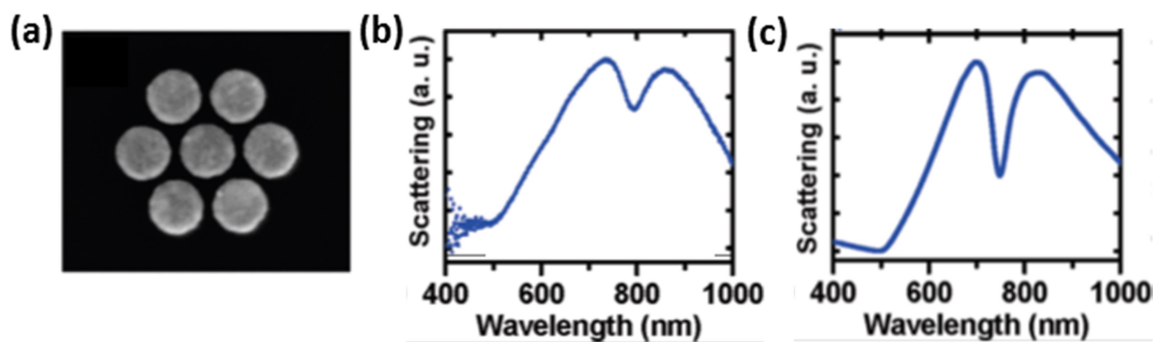


Figure 1.9 Investigation of Fano resonance in heptamer structures. (a) The SEM images of heptamer structure. (b) The experimentally obtained dark-field scattering spectrum, obtained with unpolarized light. (c) FDTD calculations of the dark-field spectral response of the same structure.³¹

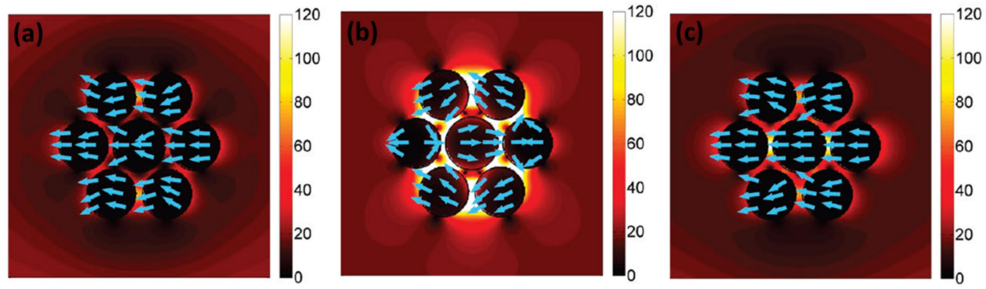


Figure 1.10 Simulated field vector distributions of plasmonic heptamer structures under three characterized wavelengths. (a, c) Field vector distributions for shorter-wavelength peak and longer-wavelength peak, respectively. (c) Field vector distribution for dip.¹⁴⁶

The far-field extinction and scattering spectra supported by plasmon hybridization and Fano resonance described above show the similar line-shape which exhibits two distinct peaks and a dip between the two peaks. In this case, it is very difficult to distinguish the plasmon hybridization or Fano resonance only from far-field extinction or scattering spectra. Such mix of the plasmon hybridization and Fano resonance is like recent investigation of crossover between the EIT phenomena and Rabi splitting in a plasmon molecular-coupled system; a theoretical effort was used to distinguish EIT and Rabi splitting via excitation spectra that reflect molecular absorption spectra.¹⁴⁷ The excitation spectra can be regarded as the optical response reveals the near-field properties. And they demonstrated that the excitation spectra can be used to distinguish the EIT and Rabi splitting.

Considering even the plasmon hybridization and Fano resonance have similar far-field line-shape, however in near field, they may differ. Since for plasmon hybridization the two original energy states hybridized into two new energy states, in near field, the near-field enhancement of these two new modes should be obtained. However, in a Fano resonance system the dark plasmon mode should have much stronger near-field enhancement, thus in near field, such dark plasmon mode should dominate. Herein, it is deduced that the near-field properties can be used to distinguish the plasmon hybridization and Fano resonance.

1.5 Near field probing techniques

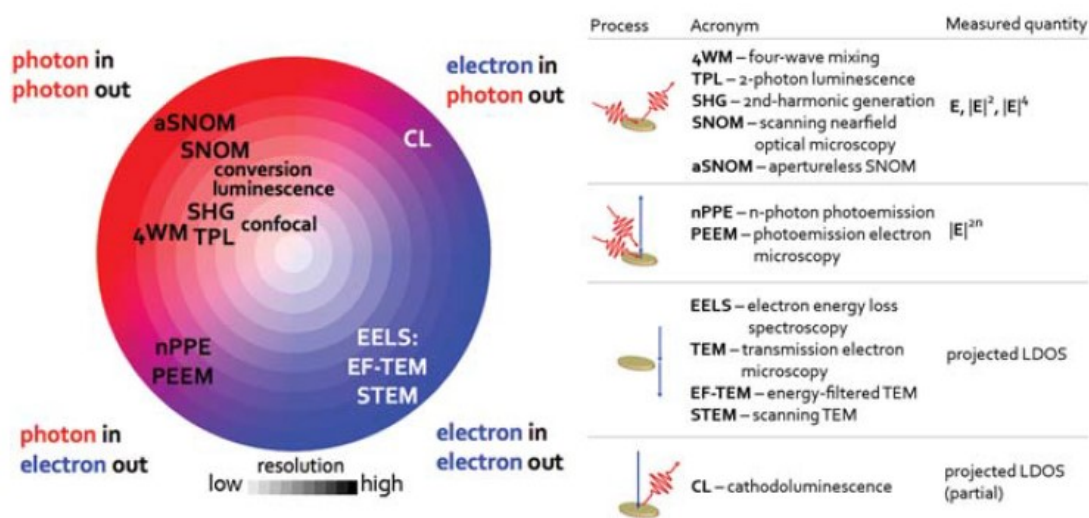


Figure 1.11 The diagram of experimental technique for near field probing. The left part schematically arranged according to incident/emitted particles. The right part shows the simplified depiction of the relevant process and the observed quantity.¹⁴⁸

Nowadays mainly four types of the near-field probing techniques can be divided based on the excitation and detection ways; they are the photon-in photon-out (photon-photon) methods, photon-in electron-out (photon-electron) method, electron-in photon-out (electron-photon) methods, and electron-in electron-out (electron-electron) method as shown in the left part of Figure 1.11.¹⁴⁸ For the photon-in photon-out (photon-photon) method, the photon scanning tunneling microscopy (PSTM), two photon luminescence (TPL), 2nd harmonic generation (SHG), scanning near field optical microscopy (SNOM) can all access to the near field and reveal the near-field properties. For the photon-in electron-out (photon-electron) method, the photoemission electron microscopy (PEEM) have rapidly developing into a powerful approach to study the near field of LSPR in both space and time. Electron energy-loss spectroscopy (EELS) is invented based on the electron-in electron-out (electron-electron) method. It can reveal the quantum of energy loss which is the spectroscopic signature of an eigenmode being excited. And Cathodoluminescence (CL) based on the electron-in photon-out (electron-photon) method can observe the energy transfer from incident electrons to the

plasmonic system through the subsequently emitted photons. These techniques have their own advantages and disadvantages; however, they all play very important roles in the investigation on the near field.

1.5.1 Scanning near-field optical microscopy (SNOM)

In normal, scanning near-field optical microscopy (SNOM) is one kind of microscope which breaks the far-field resolution limit through the usage of the evanescent waves from the sample. The signals from the sample are detected by aperture probes which place very close to the sample surface. The probes normally are the metal-coated optical glass fiber tapers or hollowed silicon atomic force microscope pyramidal tips as shown in Figure 1.12 (a). When the optical excitation (or the detection) passing through the aperture, the excitation (or detection) can be qualified as near field while the detection (or the excitation) is performed in far field. According to this, different configurations in near field and far field excitation and detection can be used as shown in Figure 1.12 (a). The near-field information can be converted into the far field signal and can be measured by the SNOM. In a SNOM system, lots of kinds of optical signals can be measured such as fluorescence, luminescence, light scattered, second or third harmonic generation, and so on. By integrating and analyzing, the specific information of the sample can be measured, especially in the scattering response, local field distribution, and phase information. A lot of the studies on the near field properties of LSPR on metallic nanoparticles have been investigated by SNOM.^{38,}

149-158

To further improve the spatial resolution, apertureless SNOM (aSNOM) using a metallic or metallized tip was established as shown in Figure 1.12 (b). Different configurations of optical excitation and collection were developed to control the input/output polarization, the optical collection, the incidence angle, and the transparency of the sample and substrate. Figure 1.12 (b) shows the side illumination

and collection configuration and the bottom illumination and/or collection configuration. The bottom illumination has much higher optical collection than side illumination, but it requires a transparent substrate. The small apex radius of the tip determines the higher spatial resolution of SNOM,¹⁵⁹ and aSNOM can be used to investigate the individual plasmon nanostructures.^{153, 160-166}

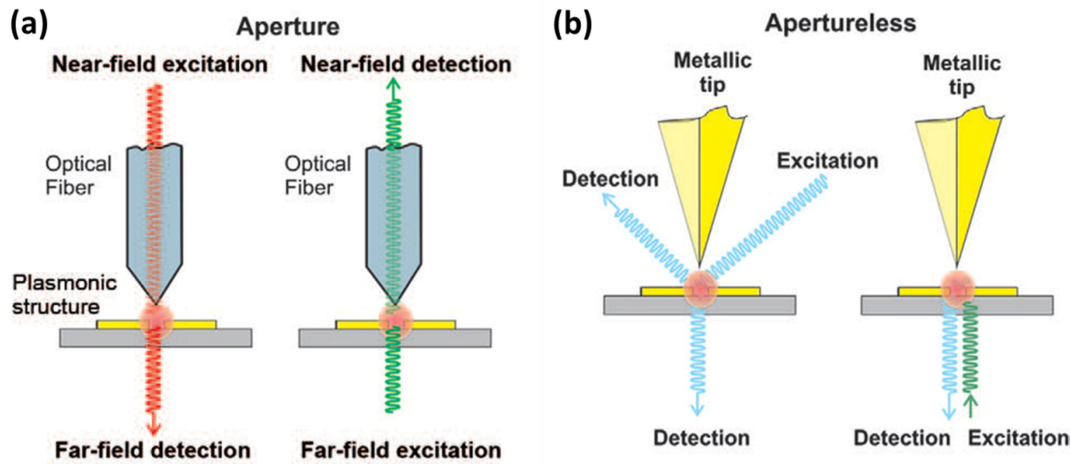


Figure 1.12 (a) SNOM using optical fiber detector. (b) aSNOM using metallic tips detector.¹⁶⁷

Figure 1.13 shows the investigations of the near field properties on simple nanostructures. The near-field amplitude (near field intensity) distributions under the light excitation can be clearly observed for nanorod, nanocircle, and nanotriangle. Furthermore, not only the amplitude distributions but also the phase information can be obtained by SNOM. The phase information can help us to clarify the charge distribution for each plasmon mode on different nanostructures. Under the horizontal polarized excitation, the dipole plasmon mode on the three kinds of nanostructures can be clearly identified and were confirmed by the phase information. The experimental results obtained by SNOM can be reproduced well with the numerical calculation results.¹⁶⁸

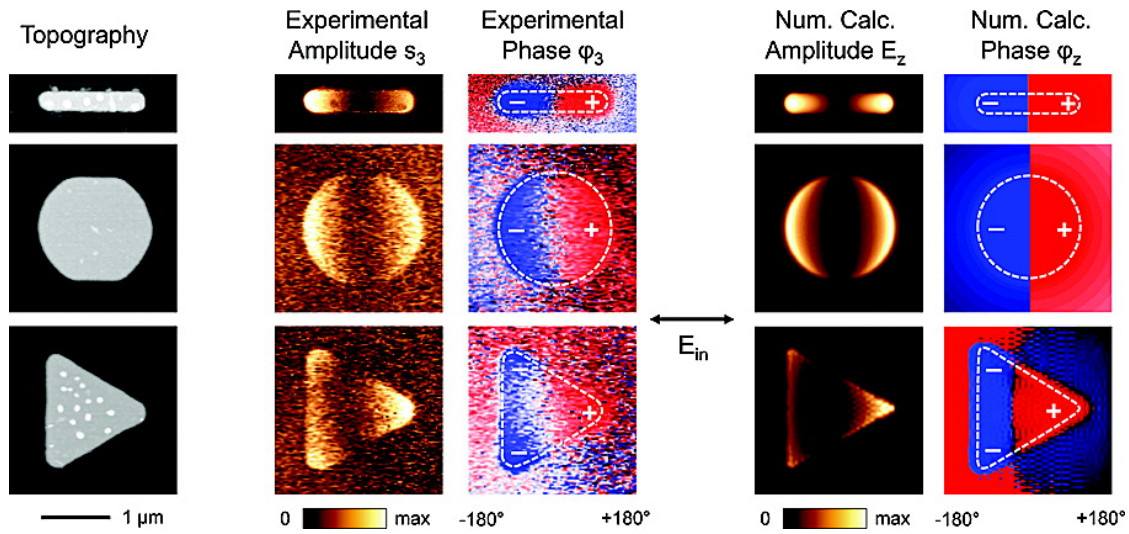


Figure 1.13 Near-field imaging for different kinds of nanostructures by SNOM. The topography (left), experimental results for amplitude and phase (middle), and numerical calculation for amplitude and phase (right) were compared.¹⁶⁸

Alonso-Gonzalez et al. investigated the Fano resonance in Au dolmen-like plasmonic nanostructures by SNOM with Si tip as shown in Figure 1.14 (a).³⁸ Figure 1.14 (b) shows the calculated reflection spectra of the dolmen-like structures under the horizontal polarization (red) and vertical polarization (blue). The results are similar with investigation described in the part of introduction of Fano resonance. Under vertical polarization excitation, the dipole plasmon mode for the entire structure has been excited. One main broad peak can be observed in the reflection spectra. The redistribution of the near-field shows the dipole plasmon mode for each nanorod as shown in Figure 1.14 (c). Under the horizontal polarization, the modes evolved as the excitation wavelength changing. Such redistribution in near field can also be resolved through the near-field mapping by SNOM as shown in Figure 1.14 (d). The results show dramatic redistributions of the electric field intensity and phase information for the structures at around the Fano wavelengths. A dark quadrupole mode was revealed at the dip wavelength excitation. With the help of SNOM, the information of near field distributions (electric field intensity and phase) can be directly revealed to us; in previous such information can be only obtained from the simulation and calculation.

The two investigations described here demonstrated that not only simple but also complex plasmonic nanostructures which exhibit dark plasmon and abundant near-field properties can be investigated by SNOM.

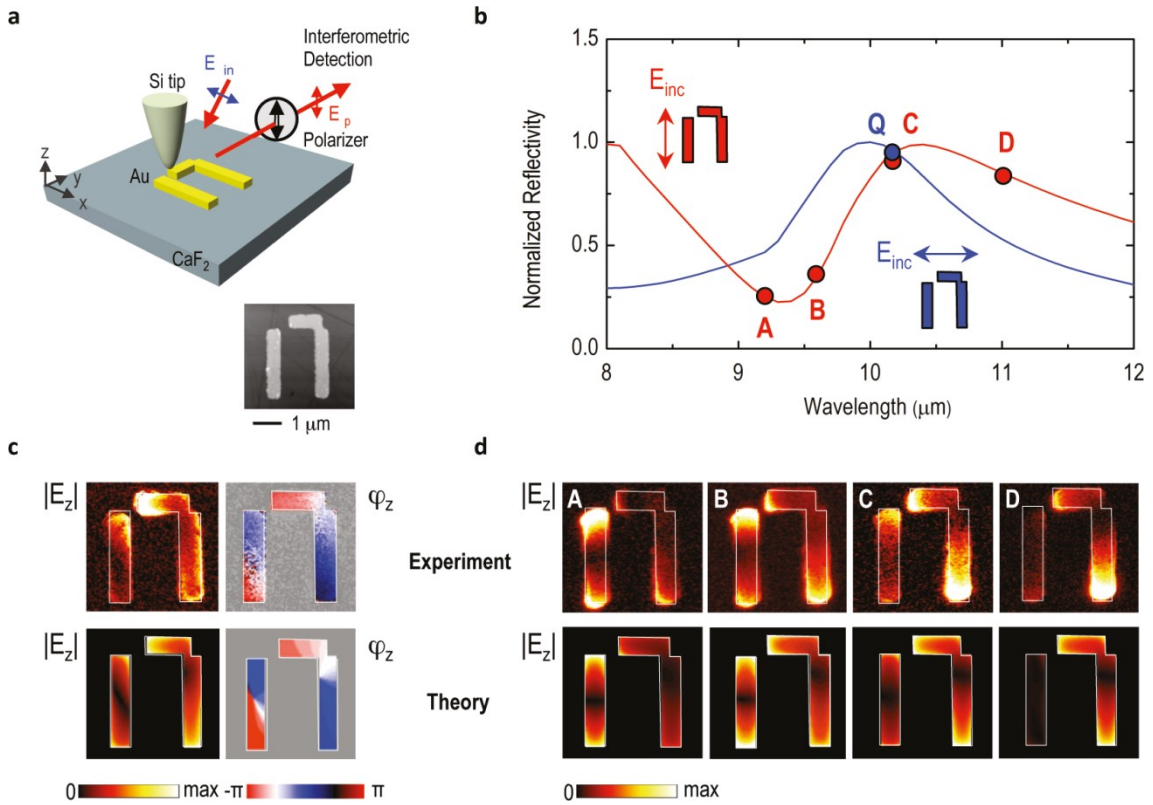


Figure 1.14 Real-space mapping of Fano interference in asymmetric dolmen-like structures. (a) Experimental setup of near-field imaging. (b) Calculated reflection spectrum for horizontal (blue) and vertical (red) polarization. (c) Experimental (up) and calculated (down) E_z under horizontal polarization. (d) Experimental (up) and calculated (down) E_z under vertical polarization.³⁸

SNOM is a very powerful tool to investigate the near-field properties of the LSPRs supported by metallic nanoparticles. It has high spatial resolution compared with the traditional optical microscope. However, it still has the spatial limitation since it is limited by the principle of the SNOM. The spatial resolution of SNOM is normally at the level of several tens of nanometer. Few reports introduced the spatial resolution of SNOM can reach less than 10 nm. For disadvantages, it is complex for analyzing of the optical near-field image due to the tip-sample interaction. Furthermore, the detectors of fiber or metallic tip are very close to the sample which guarantees the spatial resolution.

However, the very close detectors may influence the original optical properties of LSPRs.

1.5.2 Cathodoluminescence (CL) and electron energy-loss spectroscopy (EELS)

Cathodoluminescence (CL) is based on the inverse of the photoelectric effect. When a sample is illuminated by an electron beam, light can emit from the excitation of the electron beam. The photons normally emitted from the inter-band transitions between the bottom of conduction band and the valence-band maximum. It reflects the properties of the sample not the information of the element. In metallic nanostructures system, the electron beam may excite the LSPR giving rise to a detectable radiation. The information of plasmonic properties of the oscillation wavelength, near field intensity, polarization, and so on may all include in such photoemission signal and can be detected by CL. CL is normally combined with a scanning electron microscope (SEM) or a transmission electron microscope (TEM) . Firstly, it needs to use SEM or TEM to confirm the excitation position of the electron beam. Then the electron beam is scanned over the whole plasmonic nanostructure. At the same time, the photons excited by the electron beam will be collected. The sketch map of CL is shown in Figure 1.15. Two main kinds of information can be obtained in the detected signal. One is the spectral information which measured at a given point of the structure; another one is the spatial information which obtained from the radiation intensity by scanning over the sample at a given emission wavelength. After analyzing, the CL image will give the near-field spatial intensity distribution information on the metallic nanoparticles.

Electron energy-loss spectroscopy (EELS) is based on a pure electronic mechanism. One electron beam with a known and narrow range of kinetic energies illustrates on the sample, and then EELS records the signal after interaction with the sample. The EELS signal related to the energy loss during the interaction with the sample. For metallic nanostructures, the energy loss is related to the LSPR plasmon modes which excited by

the electron beam. The sketch map of EELS is shown in Figure 1.15. As shown in figure, EELS can be performed only with a TEM. EELS and CL are all using the electron beam as the excitation source, and the two methods are similar in some points. EELS can also provide the spectral information and the spatial information of LSPRs in near field. However, the ability of spectral analysis is weaker than CL. One reason is the spectral resolution of the EELS is lower than CL. Another reason is the high energy modes (typically higher than 1.5 eV) because of the very intense beam of the elastically transmitted electron beam limit the response wavelength. It means for shorter wavelength investigation (shorter than 830 nm), it is difficult to perform by EELS. Since the EELS signal is very intense, it is possible to use low electron current to avoid the damage to the sample. Furthermore, the intense EELS signal make it no need to enlarge the electron beam to measure a detectable signal, so this ensures higher spatial resolution in EELS.

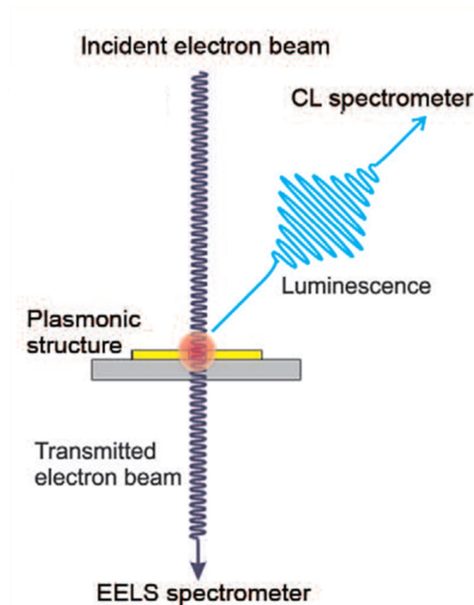


Figure 1.15 The sketch map of the CL and EELS.¹⁶⁷

Knight et al. investigated the near field properties of aluminum plasmonic nanoantennas by CL.¹⁶⁹ Figure 1.16 plots the CL mapping for aluminum nanorod with different lengths. For short aluminum nanorod, the CL mapping shows strong

photoemission located at the two sides of the structures which indicate the dipole plasmon mode has been excited. In the CL mapping of long aluminum nanorod, not only the two sides but also the inner place of the nanorod exhibit strong photoemission which indicates the higher-order plasmon mode (quadrupole) has been excited. The experiment results reproduce well with the FDTD simulations. Both the bright plasmon mode and dark plasmon mode can be revealed by CL methods. Figure 1.17 plots the CL images of aluminum nanorodantennas with different lengths and the Normalized CL emission intensity spectra for each wire length compared with the calculated scattering amplitudes spectra. The maximum near-field enhancements on nanorods with different lengths were revealed in the normalized CL intensity spectra. The results can also reproduce well with the simulations results. By using CL, the spectral information and spatial information of the LSPR in near field on metallic nanostructures can be investigated.

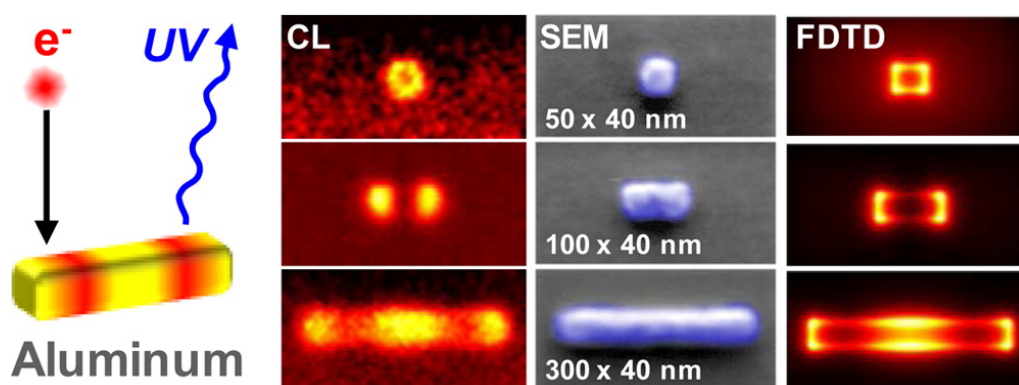


Figure 1.16 Near-field mapping of the aluminum nano antennas with different length by CL. The dipole mode in small size aluminum nanorod and the quadrupole mode in big size aluminum nanorod can be clearly observed. The CL results reproduce well with the FDTD simulation results.¹⁶⁹

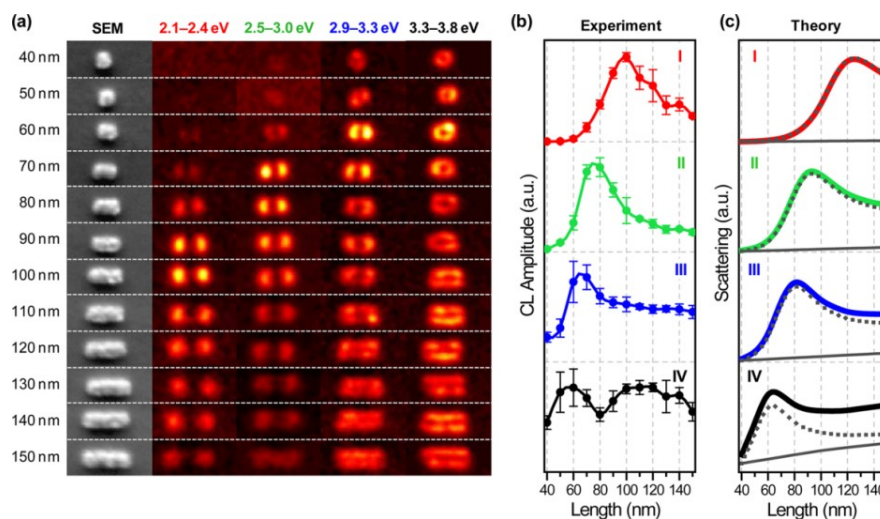


Figure 1.17 (a) SEM images with the associated CL images of aluminum nanorod antennas with different antenna lengths. (b) Normalized CL emission intensity for each wire length with different energy ranges. (c) Calculated scattering amplitudes for excitation as a function of antenna length with different energy ranges.¹⁶⁹

Figure 1.18 shows the investigated results of bow-tie antenna using EELS by Koh et al.¹⁷⁰ Figure 1.18 (a) shows the experimental EELS spectra of a bow-tie antenna from different positions of the structure. Since at different electron energy ranges, the near-field enhancement evolved at different positions because of the excitations of different plasmon modes as shown in Figure 1.18 (c)-(e). Such evolution can be observed in the EELS spectra. From the EELS spectra and near-field mapping of bow-tie antennas, different plasmon modes (the bright plasmon mode and dark plasmon mode) can be observed and distinguished at different energy ranges. And such different plasmon modes in experimental results correspond to the simulation results.

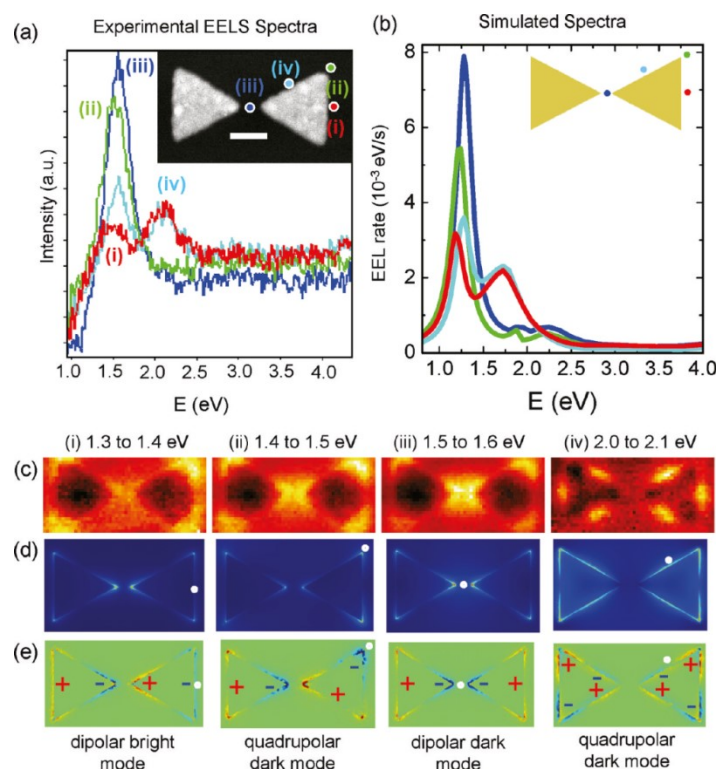


Figure 1.18 The investigation of bow-tie antenna by EELS. Experimental (a) and simulated (b) EELS spectra of a bow-tie antenna from different position of the structure. (c) Plasmon maps obtained from integrated EELS signal intensity for different energy range. (d) Simulated electric-field intensity. (e) Simulated charge distribution.¹⁷⁰

Since the CL supports a very high spectral resolution and the EELS supports a very high spatial resolution, scientists always investigate the near-field properties by combing of EELS and CL. Thus, complex metallic nanostructures can be investigated with detailed insight in the power dissipation of different plasmon modes. Coenen et al. investigated the plasmon anti-bonding plasmon mode and bonding plasmon mode supported by Au dolmen structures by EELS and CL.³⁹ The two plasmon mode can be understood from Figure 1.19 (a). From Figure 1.19 (c) and (d), the EELS and CL spectra which detected from the different structure position shown in Figure 1.19 (b) reveals the different plasmon modes (dipole plasmon mode, anti-bonding plasmon mode, bonding plasmon mode, and dark plasmon mode). Furthermore, with the help of the EELS mapping and CL mapping under specific wavelength excitation, the near-field intensity distribution for different plasmon mode can be obtained. Thus, it helps to

better understanding the different plasmon modes existing in the complex nanostructures.

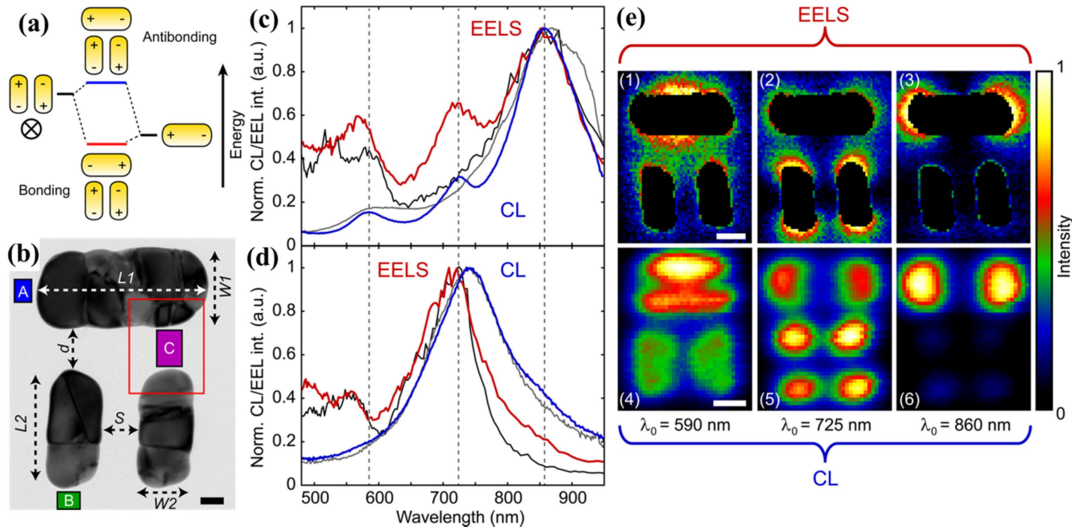


Figure 1.19 investigation of the near-field properties on dolmen structures by EELS and CL. (a) Hybridization scheme for the dolmen. (b) TEM image of a gold dolmen structure. (c) CL (blue) and EELS (red) spectra for excitation of the dolmen at position A as shown in (b). (d) CL and EELS spectra for excitation position B. (e) EELS image (1-3) and CL image (4-6) for different excitation wavelengths.³⁹

CL has very high spectral resolution (~ 1 meV) while EELS has very high spatial resolution (~ 10 nm). The two techniques are all allow for the investigation of both bright and dark plasmon mode. However, it is difficult to control the polarization which only can be tuned for the emitted light in CL. For CL, the strong electron beam can damage the sample which may take influence to the near field properties of the LSPR. For EELS, to ensure the electron transparent, in EELS system, it needs the sample must be very thin. However, CL and EELS especially the combination of the two techniques play very important role for the investigation of the near-field properties of LSPRs on metallic nanostructures.

1.5.3 Photoemission electron microscopy (PEEM)

Photoemission electron microscopy (PEEM) was firstly designed in 1933 by Brüche and his colleagues, and the PEEM made by them is shown in Figure 1.3.1.¹⁷¹ After

several tens of year development, during the 1970s and 1980s the PEEM-2 and PEEM-3 were generated, respectively. The two new type of PEEM make the performance greatly improved. Easily saying the difference between these two types of PEEM is that PEEM-3 has the aberration corrected function which employs a curved electron mirror to counter the lowest order aberrations of the electron lenses and the accelerating field. This improvement made PEEM has higher spatial resolution. PEEM is a surface sensitive technique so that it is very powerful to investigate the surface properties such as the surface physics/chemistry, material growth, and magnetic materials.^{172, 173}

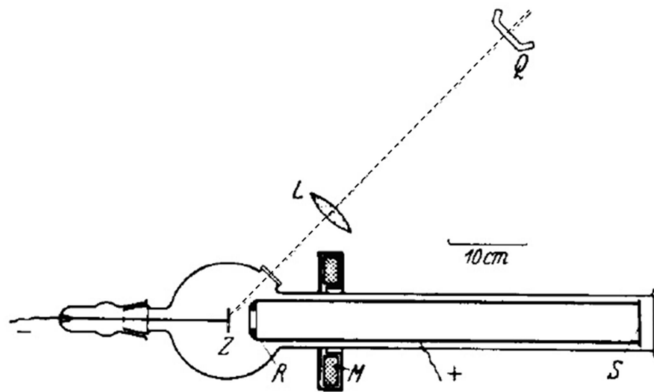


Figure 1.20 The sketch map of early PEEM.¹⁷¹

Unlike the EELS and CL, photoemission electron microscopy (PEEM) using light as the excitation sources. PEEM is based on the well-known photoelectric effect. It means that when the light irradiating on a metal material, if the energy of the photon is larger than the work function of the metal material, the photoelectrons can be induced from the metal surface due to the photoelectric effect which obey the following equation:

$$hf = \Phi + E_k$$

where E_k is the kinetic energy of an ejected electron, Φ is the work function of the metal material, h is the Planck constant and f is the frequency of the incident photon. The emitting electrons may be driven by high voltage and then pass through several electronic lens. The electrons will be focused by these lens and reach the fluorescent

screen and detected by a CCD camera. The sketch of the PEEM is shown in Figure 1.21. Due to the work principle, PEEM images reflect local differences in the overall photoemission intensity of the metal material.

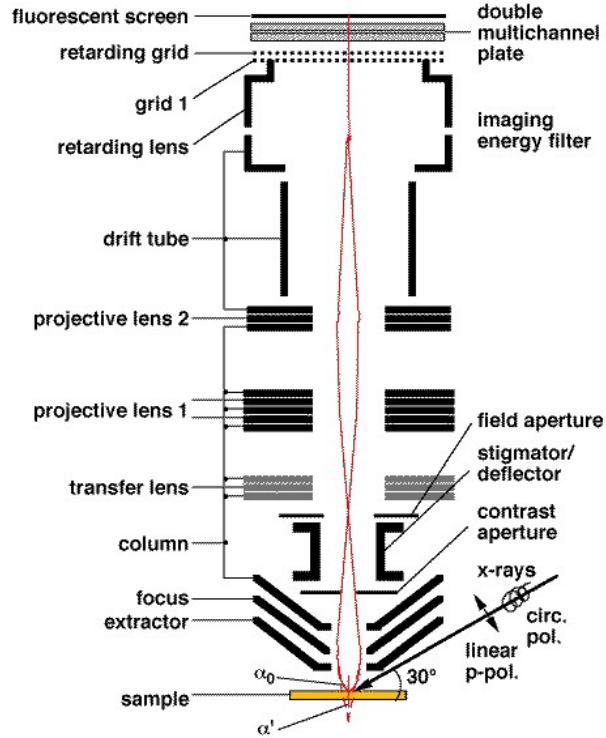


Figure 1.21 The sketch map of the PEEM.¹⁷⁴

In normal, UV light, synchrotron radiation or X-ray are selected as the excitation sources since the photon energy of such light sources is large and it is easier to overcome the work function of the materials and excite electron from the materials. In a plasmonic system which support surface plasmon resonance by metallic nanostructures, femtosecond laser pulses are usually used as the excitation source. Since in a plasmonic system, usually visible or near-infrared light has to be used as the excitation source to match the surface plasmon resonant wavelength. However at these wavelength ranges, the light energy is not enough to overcome the work function of the metal materials. Since fs laser has high peak intensity and the LSPRs can support strong near-field enhancement, the combination of these two effects make the multiphoton photoemission become possible. Because the multiphoton photoemission intensity is correspond to the near-field electric field intensity of the sample surface in a nonlinear manner, thus the fs

laser PEEM images can be treated as nonlinear near-field mapping of the LSPRs.

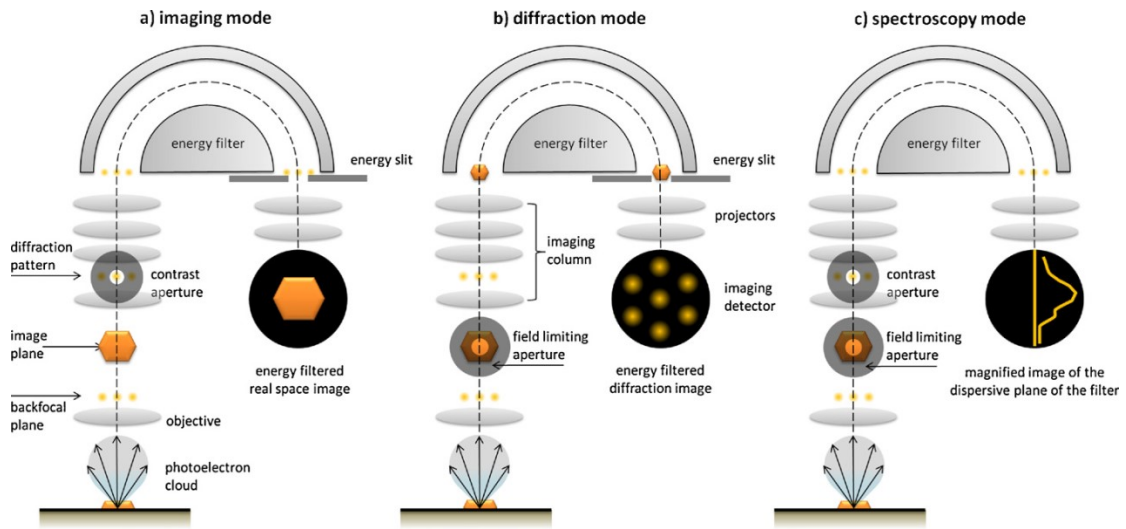


Figure 1.22 Sketch map of PEEM with energy filter in three different operation modes: (a) spectroscopic imaging, (b) spectroscopic diffraction imaging, (c) microspectroscopy operation.⁵³

Recent new type of the PEEM decorated with energy filter and field limiting aperture makes PEEM not only can image the real space of the metallic nanostructures as shown in Figure 1.22. Two new kinds of applications can be applied that are the diffraction mode which shows the energy filtered diffraction image and the spectroscopy mode which shows the magnified image of the dispersive plane of the filter. In diffraction mode, the energy filtered diffraction image can access to the local electronic structure of laterally inhomogeneous materials by the angle-resolved photoemission and photoelectron diffraction measurements.⁵³ The spectroscopy mode can be used to investigate the kinetic of the emitted electrons. Since new type of PEEM makes it possible to work in different ways, however, the investigations on plasmonic nanostructures mainly rely on the real space imaging mode of PEEM nowadays.

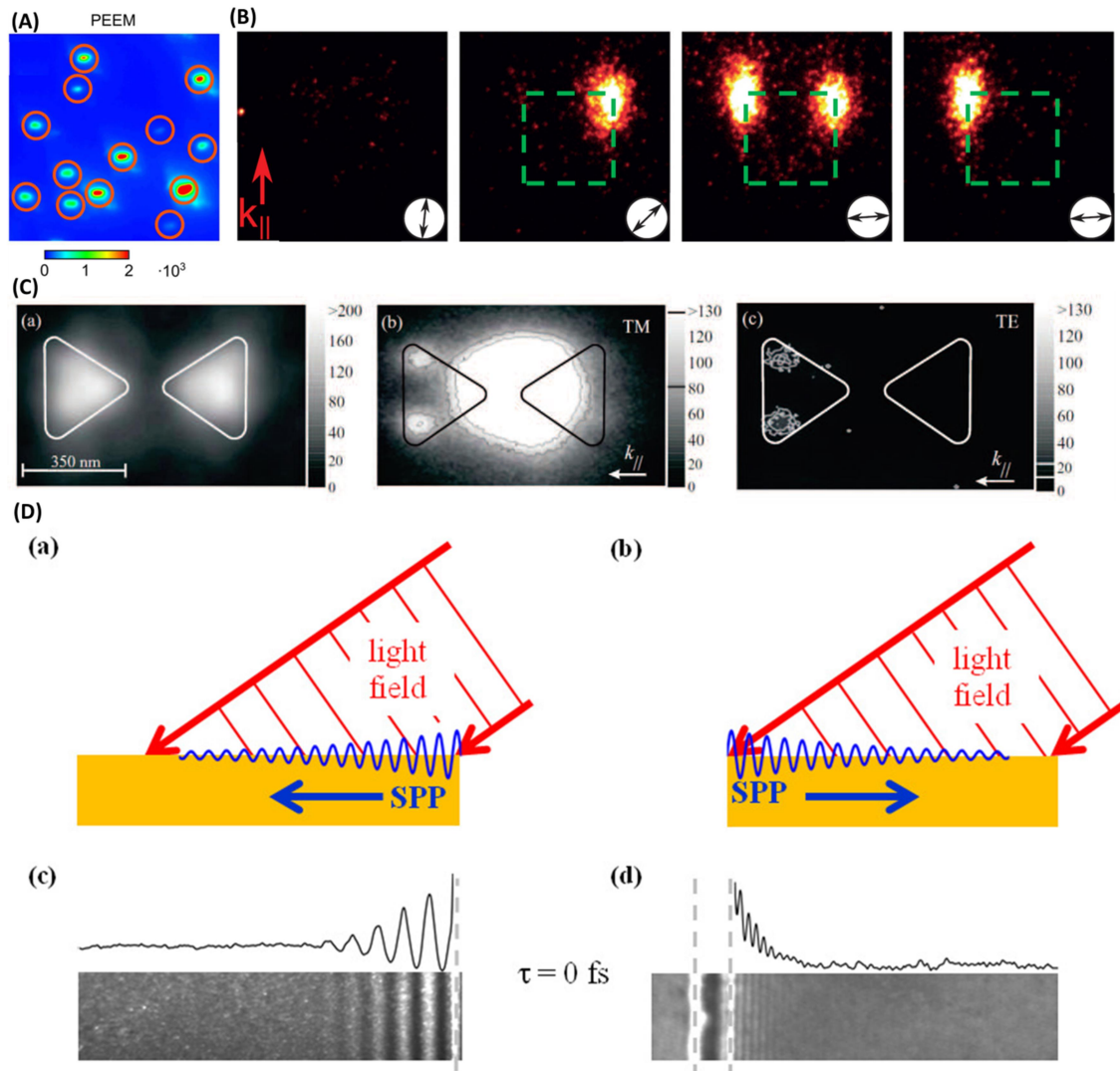


Figure 1.23 Several investigations by using PEEM. (A) PEEM image of Au nanosphere irradiated by femtosecond laser pulses.⁶⁰ (B) PEEM image of single nanoblock irradiated by femtosecond laser pulses with different polarization.¹⁷⁵ (C) PEEM image of the bow-tie antenna using different light sources.¹⁷⁶ (a) 1 photon photoemission pattern (off resonant) obtained under UV excitation. (b) 3 photon photoemission pattern under TM-polarized laser pulse excitation reveals strong photoemission from the gap and a weak photoemission at the two corners of the left nanoprism. (c) 3 photon photoemission pattern under TE-polarized laser pulse excitation shows a weak photoemission at the corners of the left nanoprism (D) Investigation of surface plasmon polaritons (SPPs) by PEEM.¹⁷⁷ (a) and (b) Schemes of the co-propagation (counter-propagation). (c) Co-propagation PEEM data of SPP propagation along a planar gold surface. (d) Corresponding data for the counter-propagating PEEM imaging mode.

Several research attempts have been investigated for the near-field properties on

different kinds of plasmonic nanostructures by PEEM using the femtosecond laser as the excitation source. Figure 1.23 (A) shows a PEEM image of Au nanosphere irradiated by the femtosecond laser pulses which investigated by Florian Schertz and co-workers.⁶⁰ The hot spots (near-field enhancement) for each nanosphere structure can be observed under the fs laser irradiation. However, in this investigation, the hot spots from an individual particle cannot be distinguished since the spatial resolution of this PEEM is not enough. Figure 1.23 (B) shows the PEEM images of Au nanoblock structures irradiated by femtosecond laser pulses with different polarizations by Erik Marsell and co-workers.¹⁷⁵ As the polarization of the excitation light changing, the hot spots distribution (near-field distribution) also changed. And PEEM images of bow-tie structures with different light sources are shown in Figure 1.23 (C) which investigated by P. Melchior and co-workers.¹⁷⁶ Using different kinds of light sources conditions, the PEEM image shows different photoemission distributions. Under the UV light excitation, 1 photon photoemission is excited (a). Under the TM-polarized laser light excitation, the hot spots localized at the gap and a weak photoemission from two corners of the left nanoprism can be observed due to the 3 photon photoemission (b). Only weak photoemission from the corners of the left nanoprism can be observed under TE-polarized excitation which also due to the 3 photon photoemission (c). PEEM can investigate not only the LSPR on metallic nanostructures but also the SPPs mode. The SPPs mode along the Au surface can be successfully observed by PEEM as an example shown in Figure 1.23 (D) which investigated by Christoph Lemke and co-workers.¹⁷⁷ In this investigation, co-propagation (a) and counter-propagation (b) can be observed from the PEEM images (c) and (d), respectively. The investigations introduced above demonstrated that PEEM is a strong powerful tool for pinpointing the near field of SPRs both in propagating mode and localized mode.

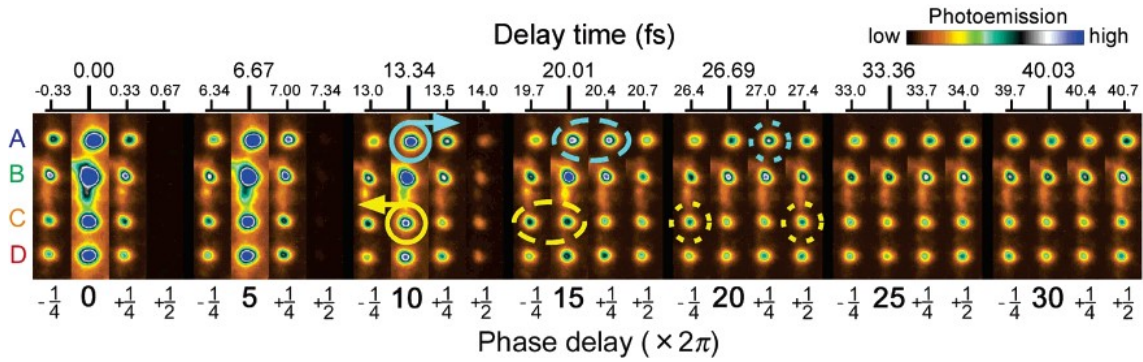


Figure 1.24 Time-resolved PEEM investigations on silver grating frame. The images show the near-field intensity evolution upon the delay time. (selected four localized hot spots on silver grating frame).⁵¹

The combination of PEEM with interferometric pump-probe techniques, time-resolved PEEM can be established. The system of time-resolved PEEM is a powerful tool to investigate the ultra-fast dynamics of LSPR and the SPPs. Atsushi Kubo and co-workers investigated the temporal properties of silver grating frame by time-resolved PEEM.⁵¹ As shown in Figure 1.24, the near-field intensity evolution of four selected hot spots on silver grating upon the delay time can be clearly observed. And after analyzed the dephasing time of the LSPRs support on metallic nanostructures can be obtained. Since the dephasing time is very short only at several to tens femtosecond level, it is very difficult to be obtained by other approaches. Therefore, time-resolved PEEM opens a new insight of the investigation of dynamics of SPRs.

In PEEM system, the requirement of the conductive substrate for the sample and the limitation of the incident angle of excitation light limit the possibility of some investigation. However, the super high spatial resolution (which can down to 4 nm) and the wide applications of PEEM for investigating the plasmonics make it attract more and more research attentions.

1.6 Aim and outline of this thesis

Complex coupled metallic nanostructures exhibit specific far- and near-field properties, such as the plasmon hybridization and Fano resonance. However, most investigations on these issues were in far field spectroscopic and numerical simulations. Since the near-field properties of complex metallic nanostructures play an important role to help for better understanding the mechanism of the LSPRs and optimizing the design of the plasmonic nanostructures for most applications, the near-field properties on complex metallic nanostructures is crucial to be determined. Therefore, this thesis aims at the near-field properties on several kinds of complex coupled metallic nanostructures which can exhibit different plasmon modes detected by powerful near-field imaging technique, PEEM. This thesis consists of five chapters including the present chapter 1. In chapter 1, it briefly describes the backgrounds of this study, the surface plasmon and plasmon coupling regime, the plasmon modes in complex plasmonic system, and introduces several near-field probing technique. Chapter 2 describes how PEEM can be applied to obtain the near-field mapping, near-field spectra, and time-resolved PEEM measurement using simple gold (Au) nanoblock structures as an example. Chapter 3 describes the investigation of the near-field properties on coupled Au dolmen structures by PEEM. Chapter 4 describes the investigation of far-field coupling and grating effects on complex metallic nanostructures by PEEM from the view point of near field. In this chapter, the spectral evolution of different plasmon modes support by Au dolmen structures, Au heptamer structures, and simple nanoblock structures have been investigated and compared depend on the pitch size of the 2D plasmonic nanostructure array. At the end of the thesis, chapter 5 summarizes the result described in chapter 2-4. This chapter also make a further perspectives beyond the research investigated in this thesis.

1.7 References

1. Jain, P. K.; Huang, X. H.; El-Sayed, I. H.; El-Sayed, M. A., Noble Metals on the Nanoscale: Optical and Photothermal Properties and Some Applications in Imaging, Sensing, Biology, and Medicine. *Accounts of Chemical Research* **2008**, 41, 1578-1586.
2. Anker, J. N.; Hall, W. P.; Lyandres, O.; Shah, N. C.; Zhao, J.; Van Duyne, R. P., Biosensing with plasmonic nanosensors. *Nature Materials* **2008**, 7, 442-453.
3. Lal, S.; Link, S.; Halas, N. J., Nano-optics from sensing to waveguiding. *Nature Photonics* **2007**, 1, 641-648.
4. Kawata, S.; Inouye, Y.; Verma, P., Plasmonics for near-field nano-imaging and superlensing. *Nature Photonics* **2009**, 3, 388-394.
5. Yang, A. K.; Hoang, T. B.; Dridi, M.; Deeb, C.; Mikkelsen, M. H.; Schatz, G. C.; Odom, T. W., Real-time tunable lasing from plasmonic nanocavity arrays. *Nature Communications* **2015**, 6, 6939.
6. Atwater, H. A.; Polman, A., Plasmonics for improved photovoltaic devices. *Nature Materials* **2010**, 9, 205-213.
7. Nishijima, Y.; Ueno, K.; Yokota, Y.; Murakoshi, K.; Misawa, H., Plasmon-Assisted Photocurrent Generation from Visible to Near-Infrared Wavelength Using a Au-Nanorods/TiO₂ Electrode. *Journal of Physical Chemistry Letters* **2010**, 1, 2031-2036.
8. Clavero, C., Plasmon-induced hot-electron generation at nanoparticle/metal-oxide interfaces for photovoltaic and photocatalytic devices. *Nature Photonics* **2014**, 8, 95-103.
9. Zhang, Y.; Zhen, Y. R.; Neumann, O.; Day, J. K.; Nordlander, P.; Halas, N. J., Coherent anti-Stokes Raman scattering with single-molecule sensitivity using a plasmonic Fano resonance. *Nature Communications* **2014**, 5, 4424.
10. Le, F.; Brandl, D. W.; Urzhumov, Y. A.; Wang, H.; Kundu, J.; Halas, N. J.; Aizpurua, J.; Nordlander, P., Metallic nanoparticle arrays: A common substrate for both surface-enhanced Raman scattering and surface-enhanced infrared absorption. *ACS Nano* **2008**, 2, 707-718.
11. Watanabe, K.; Menzel, D.; Nilius, N.; Freund, H. J., Photochemistry on metal

nanoparticles. *Chemical Reviews* **2006**, 106, 4301-4320.

12. Wu, B. T.; Ueno, K.; Yokota, Y.; Sun, K.; Zeng, H. P.; Misawa, H., Enhancement of a Two-Photon-Induced Reaction in Solution Using Light-Harvesting Gold Nanodimer Structures. *Journal of Physical Chemistry Letters* **2012**, 3, 1443-1447.

13. Tsuboi, Y.; Shimizu, R.; Shoji, T.; Kitamura, N., Near-Infrared Continuous-Wave Light Driving a Two-Photon Photochromic Reaction with the Assistance of Localized Surface Plasmon. *Journal of the American Chemical Society* **2009**, 131, 12623-12627.

14. Ueno, K.; Misawa, H., Plasmon-enhanced photocurrent generation and water oxidation from visible to near-infrared wavelengths. *Npg Asia Materials* **2013**, 5, e61.

15. Shi, X.; Ueno, K.; Takabayashi, N.; Misawa, H., Plasmon-Enhanced Photocurrent Generation and Water Oxidation with a Gold Nanoisland-Loaded Titanium Dioxide Photoelectrode. *Journal of Physical Chemistry C* **2013**, 117, 2494-2499.

16. Zhong, Y. Q.; Ueno, K.; Mori, Y.; Shi, X.; Oshikiri, T.; Murakoshi, K.; Inoue, H.; Misawa, H., Plasmon-Assisted Water Splitting Using Two Sides of the Same SrTiO₃ Single-Crystal Substrate: Conversion of Visible Light to Chemical Energy. *Angewandte Chemie-International Edition* **2014**, 53, 10350-10354.

17. Oshikiri, T.; Ueno, K.; Misawa, H., Plasmon-Induced Ammonia Synthesis through Nitrogen Photofixation with Visible Light Irradiation. *Angewandte Chemie-International Edition* **2014**, 53, 9802-9805.

18. Oshikiri, T.; Ueno, K.; Misawa, H., Selective dinitrogen conversion to ammonia using water and visible light via plasmon-induced charge separation. *Angewandte Chemie-International Edition* **2016**, 55, 3942-3946.

19. Prodan, E.; Radloff, C.; Halas, N. J.; Nordlander, P., A hybridization model for the plasmon response of complex nanostructures. *Science* **2003**, 302, 419-422.

20. Jin, R. C.; Cao, Y. C.; Hao, E. C.; Metraux, G. S.; Schatz, G. C.; Mirkin, C. A., Controlling anisotropic nanoparticle growth through plasmon excitation. *Nature* **2003**, 425, 487-490.

21. Kim, F.; Song, J. H.; Yang, P. D., Photochemical synthesis of gold nanorods. *Journal of the American Chemical Society* **2002**, 124, 14316-14317.

22. Bao, Y. J.; Hu, Z. J.; Li, Z. W.; Zhu, X.; Fang, Z. Y., Magnetic Plasmonic Fano Resonance at Optical Frequency. *Small* **2015**, 11, 2177-2181.

23. Giannini, V.; Fernandez-Dominguez, A. I.; Sonnefraud, Y.; Roschuk, T.; Fernandez-Garcia, R.; Maier, S. A., Controlling Light Localization and Light-Matter Interactions with Nanoplasmonics. *Small* **2010**, *6*, 2498-2507.
24. Ueno, K.; Mizeikis, V.; Juodkazis, S.; Sasaki, K.; Misawa, H., Optical properties of nanoengineered gold blocks. *Optics Letters* **2005**, *30*, 2158-2160.
25. Ebbesen, T. W.; Lezec, H. J.; Ghaemi, H. F.; Thio, T.; Wolff, P. A., Extraordinary optical transmission through sub-wavelength hole arrays. *Nature* **1998**, *391*, 667-669.
26. Sonnefraud, Y.; Koh, A. L.; McComb, D. W.; Maier, S. A., Nanoplasmonics: Engineering and observation of localized plasmon modes. *Laser & Photonics Reviews* **2012**, *6*, 277-295.
27. Lovera, A.; Gallinet, B.; Nordlander, P.; Martin, O. J. F., Mechanisms of Fano Resonances in Coupled Plasmonic Systems. *ACS Nano* **2013**, *7*, 4527-4536.
28. Fan, J. A.; Bao, K.; Wu, C. H.; Bao, J. M.; Bardhan, R.; Halas, N. J.; Manoharan, V. N.; Shvets, G.; Nordlander, P.; Capasso, F., Fano-like Interference in Self-Assembled Plasmonic Quadrumer Clusters. *Nano Letters* **2010**, *10*, 4680-4685.
29. Cetin, A. E.; Altug, H., Fano Resonant Ring/Disk Plasmonic Nanocavities on Conducting Substrates for Advanced Biosensing. *ACS Nano* **2012**, *6*, 9989-9995.
30. Mirin, N. A.; Bao, K.; Nordlander, P., Fano Resonances in Plasmonic Nanoparticle Aggregates. *Journal of Physical Chemistry A* **2009**, *113*, 4028-4034.
31. Lassiter, J. B.; Sobhani, H.; Fan, J. A.; Kundu, J.; Capasso, F.; Nordlander, P.; Halas, N. J., Fano Resonances in Plasmonic Nanoclusters: Geometrical and Chemical Tunability. *Nano Letters* **2010**, *10*, 3184-3189.
32. Verellen, N.; Sonnefraud, Y.; Sobhani, H.; Hao, F.; Moshchalkov, V. V.; Van Dorpe, P.; Nordlander, P.; Maier, S. A., Fano Resonances in Individual Coherent Plasmonic Nanocavities. *Nano Letters* **2009**, *9*, 1663-1667.
33. Luk'yanchuk, B.; Zheludev, N. I.; Maier, S. A.; Halas, N. J.; Nordlander, P.; Giessen, H.; Chong, C. T., The Fano Resonance in Plasmonic Nanostructures and Metamaterials. *Nature Materials* **2010**, *9*, 707-715.
34. Giannini, V.; Francescato, Y.; Amrania, H.; Phillips, C. C.; Maier, S. A., Fano Resonances in Nanoscale Plasmonic Systems: A Parameter-Free Modeling Approach. *Nano Letters* **2011**, *11*, 2835-2840.

35. Liu, N.; Langguth, L.; Weiss, T.; Kastel, J.; Fleischhauer, M.; Pfau, T.; Giessen, H., Plasmonic Analogue of Electromagnetically Induced Transparency at the Drude Damping Limit. *Nature Materials* **2009**, 8, 758-762.
36. Chen, H. Y.; He, C. L.; Wang, C. Y.; Lin, M. H.; Mitsui, D.; Eguchi, M.; Teranishi, T.; Gwo, S., Far-Field Optical Imaging of a Linear Array of Coupled Gold Nanocubes: Direct Visualization of Dark Plasmon Propagating Modes. *ACS Nano* **2011**, 5, 8223-8229.
37. Solis, D.; Willingham, B.; Nauert, S. L.; Slaughter, L. S.; Olson, J.; Swanglap, P.; Paul, A.; Chang, W. S.; Link, S., Electromagnetic Energy Transport in Nanoparticle Chains via Dark Plasmon Modes. *Nano Letters* **2012**, 12, 1349-1353.
38. Alonso-Gonzalez, P.; Schnell, M.; Sarriugarte, P.; Sobhani, H.; Wu, C. H.; Arju, N.; Khanikaev, A.; Golmar, F.; Albella, P.; Arzubiaga, L.; Casanova, F.; Hueso, L. E.; Nordlander, P.; Shvets, G.; Hillenbrand, R., Real-Space Mapping of Fano Interference in Plasmonic Metamolecules. *Nano Letters* **2011**, 11, 3922-3926.
39. Coenen, T.; Schoen, D. T.; Mann, S. A.; Rodriguez, S. R. K.; Brenny, B. J. M.; Polman, A.; Brongersma, M. L., Nanoscale Spatial Coherent Control over the Modal Excitation of a Coupled Plasmonic Resonator System. *Nano Letters* **2015**, 15, 7666-7670.
40. Frimmer, M.; Coenen, T.; Koenderink, A. F., Signature of a Fano Resonance in a Plasmonic Metamolecule's Local Density of Optical States. *Physical Review Letters* **2012**, 108.
41. Lassiter, J. B.; Sobhani, H.; Knight, M. W.; Mielczarek, W. S.; Nordlander, P.; Halas, N. J., Designing and Deconstructing the Fano Lineshape in Plasmonic Nanoclusters. *Nano Letters* **2012**, 12, 1058-1062.
42. Geldhauser, T.; Kolloch, A.; Murazawa, N.; Ueno, K.; Boneberg, J.; Leiderer, P.; Scheer, E.; Misawa, H., Quantitative Measurement of the Near-Field Enhancement of Nanostructures by Two-Photon Polymerization. *Langmuir* **2012**, 28, 9041-9046.
43. Ueno, K.; Juodkazis, S.; Shibuya, T.; Yokota, Y.; Mizeikis, V.; Sasaki, K.; Misawa, H., Nanoparticle plasmon-assisted two-photon polymerization induced by incoherent excitation source. *Journal of the American Chemical Society* **2008**, 130, 6928-6929.
44. Leiderer, P.; Bartels, C.; Konig-Birk, J.; Mosbacher, M.; Boneberg, J., Imaging Optical Near-Fields of Nanostructures. *Applied Physics Letters* **2004**, 85, 5370-5372.

45. Nedyalkov, N. N.; Takada, H.; Obara, M., Nanostructuring of Silicon Surface by Femtosecond Laser Pulse Mediated with Enhanced Near-Field of Gold Nanoparticles. *Applied Physics a-Materials Science & Processing* **2006**, 85, 163-168.
46. Eversole, D.; Luk'yanchuk, B.; Ben-Yakar, A., Plasmonic Laser Nanoablation of Silicon by the Scattering of Femtosecond Pulses Near Gold Nanospheres. *Applied Physics a-Materials Science & Processing* **2007**, 89, 283-291.
47. Kolloch, A.; Geldhauser, T.; Ueno, K.; Misawa, H.; Boneberg, J.; Plech, A.; Leiderer, P., Femtosecond and Picosecond Near-Field Ablation of Gold Nanotriangles: Nanostructuring and Nanomelting. *Applied Physics a-Materials Science & Processing* **2011**, 104, 793-799.
48. Ji, B. Y.; Qin, J.; Tao, H. Y.; Hao, Z. Q.; Lin, J. Q., Subwavelength Imaging and Control of Ultrafast Optical Near-Field under Resonant- and Off-Resonant Excitation of Bowtie Nanostructures. *New Journal of Physics* **2016**, 18, 093046.
49. Word, R. C.; Konenkamp, R., Mode Structure of Planar Optical Antennas on Dielectric Substrates. *Optics Express* **2016**, 24, 18727-18738.
50. Melchior, P.; Kilbane, D.; Vesseur, E. J.; Polman, A.; Aeschlimann, M., Photoelectron Imaging of Modal Interference in Plasmonic Whispering Gallery Cavities. *Optics Express* **2015**, 23, 31619-31626.
51. Kubo, A.; Onda, K.; Petek, H.; Sun, Z. J.; Jung, Y. S.; Kim, H. K., Femtosecond Imaging of Surface Plasmon Dynamics in a Nanostructured Silver Film. *Nano letters* **2005**, 5, 1123-1127.
52. H Yu, Q. S., J Yang, K Ueno, T Oshikiri, A Kubo, Y. Matsuo, Q. Gong, H. Misawa, Near-Field Spectral Properties of Coupled Plasmonic Nanoparticle Arrays. *Optics Express* **2017**, 25, 6883-6894.
53. Mentes, T. O.; Locatelli, A., Angle-Resolved X-Ray Photoemission Electron Microscopy. *Journal of Electron Spectroscopy and Related Phenomena* **2012**, 185, 323-329.
54. Sun, Q.; Ueno, K.; Yu, H.; Kubo, A.; Matsuo, Y.; Misawa, H., Direct imaging of the near field and dynamics of surface plasmon resonance on gold nanostructures using photoemission electron microscopy. *Light-Science & Applications* **2013**, 2, e118.
55. Sun, Q.; Yu, H.; Ueno, K.; Sun, Q.; Yu, H.; Ueno, K.; Kubo, A.; Matsuo, Y.; Misawa, H., Dissecting the Few-Femtosecond Dephasing Time of Dipole and

Quadrupole Modes in Gold Nanoparticles Using Polarized Photoemission Electron Microscopy. *ACS Nano* **2016**, 10, 3835-3842.

56. Han Yu, Q. S., Kosei Ueno, Tomoya Oshikiri, Atsushi Kubo, Yasutaka Matsuo, Hiroaki Misawa, Exploring Coupled Plasmonic Nanostructures in the Near Field by Photoemission Electron Microscopy. *ACS Nano* **2016**, 10, 10373-10381.

57. Cinchetti, M.; Gloskovskii, A.; Nepjiko, S. A.; Schonhense, G.; Rochholz, H.; Kreiter, M., Photoemission electron microscopy as a tool for the investigation of optical near fields. *Physical Review Letters* **2005**, 95, 047601.

58. Douillard, L.; Charra, F., Photoemission electron microscopy, a tool for plasmonics. *Journal of Electron Spectroscopy and Related Phenomena* **2013**, 189, 24-29.

59. Lecarme, O.; Sun, Q.; Ueno, K.; Misawa, H., Robust and Versatile Light Absorption at Near-Infrared Wavelengths by Plasmonic Aluminum Nanorods. *ACS Photonics* **2014**, 1, 538-546.

60. Schertz, F.; Schmelzeisen, M.; Mohammadi, R.; Kreiter, M.; Elmers, H. J.; Schonhense, G., Near Field of Strongly Coupled Plasmons: Uncovering Dark Modes. *Nano Letters* **2012**, 12, 1885-1890.

61. Ritchie, R. H., Plasma Losses by Fast Electrons In Thin Films. *Physical Review* **1957**, 106, 874-881.

62. Wood, R. W., On a Remarkable Case of Uneven Distribution of Light in a Diffraction Grating Spectrum. *Philosophical Magazine* **1902**, 4, 396-402.

63. Barnes, W. L.; Dereux, A.; Ebbesen, T. W., Surface Plasmon Subwavelength Optics. *Nature* **2003**, 424, 824-830.

64. Kelly, K. L.; Coronado, E.; Zhao, L. L.; Schatz, G. C., The Optical Properties of Metal Nanoparticles: The Influence of Size, Shape, and Dielectric Environment. *Journal of Physical Chemistry B* **2003**, 107, 668-677.

65. O'Hara, J. F.; Averitt, R. D.; Taylor, A. J., Prism Coupling to Terahertz Surface Plasmon Polaritons. *Optics Express* **2005**, 13, 6117-6126.

66. Lemke, C.; Schneider, C.; Leissner, T.; Bayer, D.; Radke, J. W.; Fischer, A.; Melchior, P.; Evlyukhin, A. B.; Chichkov, B. N.; Reinhardt, C.; Bauer, M.; Aeschlimann, M., Spatiotemporal Characterization of SPP Pulse Propagation in

Two-Dimensional Plasmonic Focusing Devices. *Nano Letters* **2013**, 13, 1053-1058.

67. Andrew, P.; Barnes, W. L., Energy Transfer across a Metal Film Mediated by Surface Plasmon Polaritons. *Science* **2004**, 306, 1002-1005.

68. Rivas, J. G.; Kuttge, M.; Bolivar, P. H.; Kurz, H.; Sanchez-Gil, J. A., Propagation of Surface Plasmon Polaritons on Semiconductor Gratings. *Physical Review Letters* **2004**, 93, 256804.

69. Hooper, I. R.; Sambles, J. R., Surface Plasmon Polaritons on Thin-Slab Metal Gratings. *Physical Review B* **2003**, 67, 235404.

70. Sondergaard, T.; Bozhevolnyi, S. I.; Boltasseva, A., Theoretical Analysis of Ridge Gratings for Long-Range Surface Plasmon Polaritons. *Physical Review B* **2006**, 73, 045320.

71. Garnett, J. C. M., Colours in Metal Glasses and in Metallic Films. *Philosophical Transactions of the Royal Society of London Series a-Containing Papers of a Mathematical or Physical Character* **1904**, 203, 385-420.

72. Schuller, J. A.; Barnard, E. S.; Cai, W. S.; Jun, Y. C.; White, J. S.; Brongersma, M. L., Plasmonics for Extreme Light Concentration and Manipulation. *Nature Materials* **2010**, 9, 193-204.

73. Kauranen, M.; Zayats, A. V., Nonlinear Plasmonics. *Nature Photonics* **2012**, 6, 737-748.

74. Schumacher, T.; Kratzer, K.; Molnar, D.; Hentschel, M.; Giessen, H.; Lippitz, M., Nanoantenna-Enhanced Ultrafast Nonlinear Spectroscopy of a Single Gold Nanoparticle. *Nature Communications* **2011**, 2, 333.

75. Celebrano, M.; Wu, X. F.; Baselli, M.; Grossmann, S.; Biagioni, P.; Locatelli, A.; De Angelis, C.; Cerullo, G.; Osellame, R.; Hecht, B.; Duo, L.; Ciccacci, F.; Finazzi, M., Mode Matching in Multiresonant Plasmonic Nanoantennas for Enhanced Second Harmonic Generation. *Nature Nanotechnology* **2015**, 10, 412-417.

76. Aouani, H.; Rahmani, M.; Navarro-Cia, M.; Maier, S. A., Third-harmonic-upconversion enhancement from a single semiconductor nanoparticle coupled to a plasmonic antenna. *Nature Nanotechnology* **2014**, 9, 290-294.

77. Sonnichsen, C.; Franzl, T.; Wilk, T.; von Plessen, G.; Feldmann, J.; Wilson, O.; Mulvaney, P., Drastic Reduction of Plasmon Damping in Gold Nanorods. *Physical*

Review Letters **2002**, 88, 077402.

78. Lamprecht, B.; Schider, G.; Lechner, R. T.; Ditlbacher, H.; Krenn, J. R.; Leitner, A.; Aussenegg, F. R., Metal Nanoparticle Gratings: Influence of Dipolar Particle Interaction on the Plasmon Resonance. *Physical Review Letters* **2000**, 84, 4721-4724.

79. Ueno, K.; Juodkazis, S.; Shibuya, T.; Yokota, Y.; Mizeikis, V.; Sasaki, K.; Misawa, H., Nanoparticle Plasmon-Assisted Two-Photon Polymerization Induced by Incoherent Excitation Source. *Journal of the American Chemical Society* **2008**, 130, 6928-6929.

80. Verellen, N.; Sonnefraud, Y.; Sobhani, H.; Hao, F.; Moshchalkov, V. V.; Van Dorpe, P.; Nordlander, P.; Maier, S. A., Fano Resonances in Individual Coherent Plasmonic Nanocavities. *Nano Letters* **2009**, 9, 1663-1667.

81. Meier, M.; Wokaun, A.; Liao, P. F., Enhanced Fields on Rough Surfaces - Dipolar Interactions among Particles Of Sizes Exceeding the Rayleigh Limit. *Journal of the Optical Society of America B-Optical Physics* **1985**, 2, 931-949.

82. Felidj, N.; Laurent, G.; Aubard, J.; Levi, G.; Hohenau, A.; Krenn, J. R.; Aussenegg, F. R., Grating-Induced Plasmon Mode in Gold Nanoparticle Arrays. *Journal of Chemical Physics* **2005**, 123, 221103.

83. Davis, T. J.; Gomez, D. E.; Vernon, K. C., Simple Model for the Hybridization of Surface Plasmon Resonances in Metallic Nanoparticles. *Nano Letters* **2010**, 10, 2618-2625.

84. Panaro, S.; De Angelis, F.; Toma, A., Dark and bright mode hybridization: from electric to magnetic fano resonances. *Optics and Lasers in Engineering* **2016**, 76, 64-69.

85. Arango, F. B.; Coenen, T.; Koenderink, A. F., Underpinning Hybridization Intuition for Complex Nanoantennas by Magnetolectric Quadrupolar Polarizability Retrieval. *ACS Photonics* **2014**, 1, 444-453.

86. Fano, U., *Nuovo Cimento* **1935**, 12.

87. Fano, U., Effects Of Configuration Interaction on Intensities And Phase Shifts. *Physical Review* **1961**, 124, 1866-1878.

88. Alhassid, Y.; Fyodorov, Y. V.; Gorin, T.; Ihra, W.; Mehlig, B., Fano Interference and Cross-Section Fluctuations in Molecular Photodissociation. *Physical Review A* **2006**, 73, 042711.

89. Hoffmann, T. H.; Allan, M.; Franz, K.; Ruf, M. W.; Hotop, H.; Sauter, G.; Meyer, W., Resonance Structure in Electron-N-2 Scattering Around 11.5 Ev: High-Resolution Measurements, Ab Initio Calculations and Line Shape Analyses. *Journal of Physics B-Atomic Molecular And Optical Physics* **2009**, 42, 215202.
90. Franco, R.; Figueira, M. S.; Anda, E. V., Fano Resonance in Electronic Transport Through a Quantum Wire with a Side-Coupled Quantum Dot: X-Boson Treatment. *Physical Review B* **2003**, 67, 155301.
91. Johnson, A. C.; Marcus, C. M.; Hanson, M. P.; Gossard, A. C., Charge sensing of excited states in an isolated double quantum dot. *Physical Review B* **2005**, 71, 115333.
92. Kobayashi, K.; Aikawa, H.; Sano, A.; Katsumoto, S.; Iye, Y., fano resonance in a quantum wire with a side-coupled quantum dot. *Physical Review B* **2004**, 70, 035319.
93. Luo, H. G.; Xiang, T.; Wang, X. Q.; Su, Z. B.; Yu, L., Fano resonance for Anderson impurity systems. *Physical Review Letters* **2004**, 92, 256602.
94. Mukhopadhyay, S.; Biswas, R.; Sinha, C., Signature of quantum interference and the Fano resonances in the transmission spectrum of bilayer graphene nanostructure. *Journal of Applied Physics* **2011**, 110, 014306.
95. Mukhopadhyay, S.; Biswas, R.; Sinha, C., Tunable Fano Resonances in The Ballistic Transmission and Tunneling Lifetime in a Biased Bilayer Graphene Nanostructure. *Physics Letters A* **2011**, 375, 2921-2927.
96. Rybin, M. V.; Khanikaev, A. B.; Inoue, M.; Samusev, K. B.; Steel, M. J.; Yushin, G.; Limonov, M. F., Fano Resonance between Mie and Bragg Scattering in Photonic Crystals. *Physical Review Letters* **2009**, 103, 023901.
97. Rybin, M. V.; Khanikaev, A. B.; Inoue, M.; Samusev, A. K.; Steel, M. J.; Yushin, G.; Limonov, M. F., Bragg Scattering Induces Fano Resonance in Photonic Crystals. *Photonics And Nanostructures-Fundamentals And Applications* **2010**, 8, 86-93.
98. Fan, S. H., Sharp asymmetric line shapes in side-coupled waveguide-cavity systems. *Applied Physics Letters* **2002**, 80, 908-910.
99. Fan, S. H.; Joannopoulos, J. D., Analysis Of Guided Resonances In Photonic Crystal Slabs. *Physical Review B* **2002**, 65, 235112.
100. Genet, C.; van Exter, M. P.; Woerdman, J. P., Fano-Type Interpretation of Red Shifts and Red Tails in Hole Array Transmission Spectra. *Optics Communications*

2003, 225, 331-336.

101. Fan, S. H.; Suh, W.; Joannopoulos, J. D., Temporal Coupled-Mode Theory for the Fano Resonance in Optical Resonators. *Journal of the Optical Society of America a-Optics Image Science And Vision* **2003**, 20, 569-572.

102. Christ, A.; Tikhodeev, S. G.; Gippius, N. A.; Kuhl, J.; Giessen, H., Waveguide-plasmon polaritons: Strong coupling of photonic and electronic resonances in a metallic photonic crystal slab. *Physical Review Letters* **2003**, 91, 183901.

103. Christ, A.; Zentgraf, T.; Kuhl, J.; Tikhodeev, S. G.; Gippius, N. A.; Giessen, H., Optical properties of planar metallic photonic crystal structures: Experiment and theory. *Physical Review B* **2004**, 70, 125113.

104. Catrysse, P. B.; Fan, S. H., Near-complete transmission through subwavelength hole arrays in phonon-polaritonic thin films. *Physical Review B* **2007**, 75, 075422.

105. Ruan, Z. C.; Fan, S. H., Temporal coupled-mode theory for fano resonance in light scattering by a single obstacle. *Journal of Physical Chemistry C* **2010**, 114, 7324-7329.

106. Jansen, C.; Al-Naib, I. A. I.; Born, N.; Koch, M., Terahertz metasurfaces with high Q-factors. *Applied Physics Letters* **2011**, 98, 051109.

107. Li, Z. Y.; Ma, Y. F.; Huang, R.; Singh, R. J.; Gu, J. Q.; Tian, Z.; Han, J. G.; Zhang, W. L., Manipulating the plasmon-induced transparency in terahertz metamaterials. *Optics Express* **2011**, 19, 8912-8919.

108. Pradarutti, B.; Torosyan, G.; Theuer, M.; Beigang, R., Fano profiles in transmission spectra of terahertz radiation through one-dimensional periodic metallic structures. *Applied Physics Letters* **2010**, 97, 244103.

109. Singh, R.; Al-Naib, I. A. I.; Koch, M.; Zhang, W. L., Sharp Fano resonances in THz metamaterials. *Optics Express* **2011**, 19, 6312-6319.

110. Singh, R.; Al-Naib, I. A. I.; Yang, Y. P.; Chowdhury, D. R.; Cao, W.; Rockstuhl, C.; Ozaki, T.; Morandotti, R.; Zhang, W. L., Observing metamaterial induced transparency in individual Fano resonators with broken symmetry. *Applied Physics Letters* **2011**, 99, 201107.

111. Tuniz, A.; Lwin, R.; Argyros, A.; Fleming, S. C.; Pogson, E. M.; Constable, E.; Lewis, R. A.; Kuhlmeier, B. T., Stacked-and-drawn metamaterials with magnetic

- resonances in the terahertz range. *Optics Express* **2011**, 19, 16480-16490.
112. Xiao, X. A.; Wu, J. B.; Miyamaru, F.; Zhang, M. Y.; Li, S. B.; Takeda, M. W.; Wen, W. J.; Sheng, P., Fano effect of metamaterial resonance in terahertz extraordinary transmission. *Applied Physics Letters* **2011**, 98, 011911.
113. Agio, M., Optical antennas as nanoscale resonators. *Nanoscale* **2012**, 4, 692-706.
114. Biagioni, P.; Huang, J. S.; Hecht, B., Nanoantennas for visible and infrared radiation. *Reports on Progress In Physics* **2012**, 75, 024402.
115. Fernandez-Dominguez, A. I.; Maier, S. A., New Design Principles for Nanoplasmonics. *Ieee Photonics Journal* **2011**, 3, 284-287.
116. Lei, D. Y.; Appavoo, K.; Sonnefraud, Y.; Haglund, R. F.; Maier, S. A., Single-particle plasmon resonance spectroscopy of phase transition in vanadium dioxide. *Optics Letters* **2010**, 35, 3988-3990.
117. Lei, D. Y.; Aubry, A.; Maier, S. A.; Pendry, J. B., Broadband nano-focusing of light using kissing nanowires. *New Journal of Physics* **2010**, 12, 093030.
118. Lei, D. Y.; Fernandez-Dominguez, A. I.; Sonnefraud, Y.; Appavoo, K.; Haglund, R. F.; Pendry, J. B.; Maier, S. A., Revealing Plasmonic Gap Modes in Particle-on-Film Systems Using Dark-Field Spectroscopy. *ACS Nano* **2012**, 6, 1380-1386.
119. Maier, S., Plasmonics: Fundamentals and Applications. *Springer* **2007**.
120. Stockman, M. I., Nanoplasmonics: past, present, and glimpse into future. *Optics Express* **2011**, 19, 22029-22106.
121. Utikal, T.; Zentgraf, T.; Paul, T.; Rockstuhl, C.; Lederer, F.; Lippitz, M.; Giessen, H., Towards the Origin of the Nonlinear Response in Hybrid Plasmonic Systems. *Physical Review Letters* **2011**, 106, 133901.
122. Zhang, W. H.; Gallinet, B.; Martin, O. J. F., Symmetry and selection rules for localized surface plasmon resonances in nanostructures. *Physical Review B* **2010**, 81, 233407.
123. Tribelsky, M. I.; Flach, S.; Miroshnichenko, A. E.; Gorbach, A. V.; Kivshar, Y. S., Light scattering by a finite obstacle and fano resonances. *Physical Review Letters* **2008**, 100, 043903.

124. Hao, F.; Sonnefraud, Y.; Van Dorpe, P.; Maier, S. A.; Halas, N. J.; Nordlander, P., Symmetry Breaking in Plasmonic Nanocavities: Subradiant LSPR Sensing and a Tunable Fano Resonance. *Nano Letters* **2008**, *8*, 3983-3988.
125. Hao, F.; Nordlander, P.; Sonnefraud, Y.; Van Dorpe, P.; Maier, S. A., Tunability of Subradiant Dipolar and Fano-Type Plasmon Resonances in Metallic Ring/Disk Cavities: Implications for Nanoscale Optical Sensing. *ACS Nano* **2009**, *3*, 643-652.
126. Maier, S. A., The benefits of darkness. *Nature Materials* **2009**, *8*, 699-700.
127. Sonnefraud, Y.; Verellen, N.; Sobhani, H.; Vandenbosch, G. A. E.; Moshchalkov, V. V.; Van Dorpe, P.; Nordlander, P.; Maier, S. A., Experimental Realization of Subradiant, Superradiant, and Fano Resonances in Ring/Disk Plasmonic Nanocavities. *ACS Nano* **2010**, *4*, 1664-1670.
128. Luk'yanchuk, B.; Zheludev, N. I.; Maier, S. A.; Halas, N. J.; Nordlander, P.; Giessen, H.; Chong, C. T., The Fano resonance in plasmonic nanostructures and metamaterials. *Nature Materials* **2010**, *9*, 707-715.
129. Rahmani, M.; Luk'yanchuk, B.; Hong, M. H., Fano resonance in novel plasmonic nanostructures. *Laser & Photonics Reviews* **2013**, *7*, 329-349.
130. Fedotov, V. A.; Rose, M.; Prosvirnin, S. L.; Papasimakis, N.; Zheludev, N. I., Sharp trapped-mode resonances in planar metamaterials with a broken structural symmetry. *Physical Review Letters* **2007**, *99*, 147401.
131. Christ, A.; Ekinici, Y.; Solak, H. H.; Gippius, N. A.; Tikhodeev, S. G.; Martin, O. J. F., Controlling the Fano interference in a plasmonic lattice. *Physical Review B* **2007**, *76*, 201405.
132. Bachelier, G.; Russier-Antoine, I.; Benichou, E.; Jonin, C.; Del Fatti, N.; Vallee, F.; Brevet, P. F., Fano Profiles Induced by Near-Field Coupling in Heterogeneous Dimers of Gold and Silver Nanoparticles. *Physical Review Letters* **2008**, *101*, 197401.
133. Ekinici, Y.; Christ, A.; Agio, M.; Martin, O. J. F.; Solak, H. H.; Löffler, J. F., Electric and magnetic resonances in arrays of coupled gold nanoparticle in-tandem pairs. *Optics Express* **2008**, *16*, 13287-13295.
134. Christ, A.; Martin, O. J. F.; Ekinici, Y.; Gippius, N. A.; Tikhodeev, S. G., Symmetry breaking in a plasmonic metamaterial at optical wavelength. *Nano Letters* **2008**, *8*, 2171-2175.

135. Naether, U.; Rivas, D. E.; Larenas, M. A.; Molina, M. I.; Vicencio, R. A., Fano resonances in waveguide arrays with saturable nonlinearity. *Optics Letters* **2009**, *34*, 2721-2723.
136. Cubukcu, E.; Zhang, S.; Park, Y. S.; Bartal, G.; Zhang, X., Split ring resonator sensors for infrared detection of single molecular monolayers. *Applied Physics Letters* **2009**, *95*, 043113.
137. Kante, B.; de Lustrac, A.; Lourtioz, J. M., In-plane coupling and field enhancement in infrared metamaterial surfaces. *Physical Review B* **2009**, *80*, 035108.
138. Liu, N.; Weiss, T.; Mesch, M.; Langguth, L.; Eigenthaler, U.; Hirscher, M.; Sonnichsen, C.; Giessen, H., Planar Metamaterial Analogue of Electromagnetically Induced Transparency for Plasmonic Sensing. *Nano Letters* **2010**, *10*, 1103-1107.
139. Urzhumov, Y. A.; Korobkin, D.; Neuner, B.; Zorman, C.; Shvets, G., Optical properties of sub-wavelength hole arrays in SiC membranes. *Journal of Optics a-Pure And Applied Optics* **2007**, *9*, S322-S333.
140. Parsons, J.; Hendry, E.; Burrows, C. P.; Auguie, B.; Sambles, J. R.; Barnes, W. L., Localized surface-plasmon resonances in periodic nondiffracting metallic nanoparticle and nanohole arrays. *Physical Review B* **2009**, *79*, 073412.
141. Li, Z. P.; Shegai, T.; Haran, G.; Xu, H. X., Multiple-Particle Nanoantennas for Enormous Enhancement and Polarization Control of Light Emission. *ACS Nano* **2009**, *3*, 637-642.
142. Yan, C.; Martin, O. J. F., Periodicity-Induced Symmetry Breaking in a Fano Lattice: Hybridization and Tight-Binding Regimes. *ACS Nano* **2014**, *8*, 11860-11868.
143. Gallinet, B.; Martin, O. J. F., Influence of Electromagnetic Interactions on the Line Shape of Plasmonic Fano Resonances. *ACS Nano* **2011**, *5*, 8999-9008.
144. Fang, Z. Y.; Cai, J. Y.; Yan, Z. B.; Nordlander, P.; Halas, N. J.; Zhu, X., Removing a Wedge from a Metallic Nanodisk Reveals a Fano Resonance. *Nano Letters* **2011**, *11*, 4475-4479.
145. Ye, J.; Wen, F. F.; Sobhani, H.; Lassiter, J. B.; Van Dorpe, P.; Nordlander, P.; Halas, N. J., Plasmonic Nanoclusters: Near Field Properties of the Fano Resonance Interrogated with SERS. *Nano Letters* **2012**, *12*, 1660-1667.
146. Hentschel, M.; Saliba, M.; Vogelgesang, R.; Giessen, H.; Alivisatos, A. P.; Liu, N.,

Transition from Isolated to Collective Modes in Plasmonic Oligomers. *Nano Letters* **2010**, 10, 2721-2726.

147. Murata, N.; Hata, R.; Ishihara, H., Crossover between Energy Transparency Resonance and Rabi Splitting in Antenna-Molecule Coupled Systems. *Journal of Physical Chemistry C* **2015**, 119, 25493-25498.

148. Vogelgesang, R.; Dmitriev, A., Real-space imaging of nanoplasmonic resonances. *Analyst* **2010**, 135, 1175-1181.

149. Bakker, R. M.; Drachev, V. P.; Yuan, H. K.; Shalaev, V. M., Near-field, broadband optical spectroscopy of metamaterials. *Physica B-Condensed Matter* **2007**, 394, 137-140.

150. Imura, K.; Nagahara, T.; Okamoto, H., Plasmon mode imaging of single gold nanorods. *Journal of the American Chemical Society* **2004**, 126, 12730-12731.

151. Imura, K.; Nagahara, T.; Okamoto, H., Near-field optical imaging of plasmon modes in gold nanorods. *Journal Of Chemical Physics* **2005**, 122, 154701.

152. Denkova, D.; Verellen, N.; Silhanek, A. V.; Valev, V. K.; Van Dorpe, P.; Moshchalkov, V. V., Mapping Magnetic Near-Field Distributions of Plasmonic Nanoantennas. *ACS Nano* **2013**, 7, 3168-3176.

153. Rang, M.; Jones, A. C.; Zhou, F.; Li, Z. Y.; Wiley, B. J.; Xia, Y. N.; Raschke, M. B., Optical Near-Field Mapping of Plasmonic Nanoprisms. *Nano Letters* **2008**, 8, 3357-3363.

154. Tanaka, Y.; Ishiguro, H.; Fujiwara, H.; Yokota, Y.; Ueno, K.; Misawa, H.; Sasaki, K., Direct imaging of nanogap-mode plasmon-resonant fields. *Optics Express* **2011**, 19, 7726-7733.

155. Achermann, M.; Shuford, K. L.; Schatz, G. C.; Dahanayaka, D. H.; Bumm, L. A.; Klimov, V. I., Near-field spectroscopy of surface plasmons in flat gold nanoparticles. *Optics Letters* **2007**, 32, 2254-2256.

156. Burrese, M.; van Oosten, D.; Kampfrath, T.; Schoenmaker, H.; Heideman, R.; Leinse, A.; Kuipers, L., Probing the Magnetic Field of Light at Optical Frequencies. *Science* **2009**, 326, 550-553.

157. Halliwell, D. E.; Morais, C. L. M.; Lima, K. M. G.; Trevisan, J.; Siggel-King, M. R. F.; Craig, T.; Ingham, J.; Martin, D. S.; Heys, K. A.; Kyrgiou, M.; Mitra, A.;

Paraskevaïdis, E.; Theophilou, G.; Martin-Hirsch, P. L.; Cricenti, A.; Luce, M.; Weightman, P.; Martin, F. L., Imaging cervical cytology with scanning near-field optical microscopy (SNOM) coupled with an IR-FEL. *Scientific Reports* **2016**, *6*, 29494.

158. Klein, A. E.; Janunts, N.; Steinert, M.; Tunnermann, A.; Pertsch, T., Polarization-Resolved Near-Field Mapping of Plasmonic Aperture Emission by a Dual-SNOM System. *Nano Letters* **2014**, *14*, 5010-5015.

159. Esteban, R.; Vogelgesang, R.; Kern, K., Full simulations of the apertureless scanning near field optical microscopy signal: achievable resolution and contrast. *Optics Express* **2009**, *17*, 2518-2529.

160. Esteban, R.; Vogelgesang, R.; Dorfmueller, J.; Dmitriev, A.; Rockstuhl, C.; Etrich, C.; Kern, K., Direct Near-Field Optical Imaging of Higher Order Plasmonic Resonances. *Nano Letters* **2008**, *8*, 3155-3159.

161. Vogelgesang, R.; Dorfmueller, J.; Esteban, R.; Weitz, R. T.; Dmitriev, A.; Kern, K., Plasmonic nanostructures in aperture-less scanning near-field optical microscopy (aSNOM). *Physica Status Solidi B-Basic Solid State Physics* **2008**, *245*, 2255-2260.

162. Schnell, M.; Garcia-Etxarri, A.; Huber, A. J.; Crozier, K.; Aizpurua, J.; Hillenbrand, R., Controlling the near-field oscillations of loaded plasmonic nanoantennas. *Nature Photonics* **2009**, *3*, 287-291.

163. Rindzevicius, T.; Alaverdyan, Y.; Sepulveda, B.; Pakizeh, T.; Kall, M.; Hillenbrand, R.; Aizpurua, J.; de Abajo, F. J. G., Nanohole plasmons in optically thin gold films. *Journal of Physical Chemistry C* **2007**, *111*, 1207-1212.

164. Olmon, R. L.; Krenz, P. M.; Jones, A. C.; Boreman, G. D.; Raschke, M. B., Near-field imaging of optical antenna modes in the mid-infrared. *Optics Express* **2008**, *16*, 20295-20305.

165. Dorfmueller, J.; Vogelgesang, R.; Weitz, R. T.; Rockstuhl, C.; Etrich, C.; Pertsch, T.; Lederer, F.; Kern, K., Fabry-Perot Resonances in One-Dimensional Plasmonic Nanostructures. *Nano Letters* **2009**, *9*, 2372-2377.

166. Jones, A. C.; Olmon, R. L.; Skrabalak, S. E.; Wiley, B. J.; Xia, Y. N.; Raschke, M. B., Mid-IR Plasmonics: Near-Field Imaging of Coherent Plasmon Modes of Silver Nanowires. *Nano Letters* **2009**, *9*, 2553-2558.

167. Merlen, A.; Lagugne-Labarthe, F., Imaging the Optical Near Field in Plasmonic

Nanostructures. *Applied Spectroscopy* **2014**, 68, 1307-1326.

168. Schnell, M.; Garcia-Etxarri, A.; Huber, A. J.; Crozier, K. B.; Borisov, A.; Aizpurua, J.; Hillenbrand, R., Amplitude- and Phase-Resolved Near-Field Mapping of Infrared Antenna Modes by Transmission-Mode Scattering-Type Near-Field Microscopy. *Journal of Physical Chemistry C* **2010**, 114, 7341-7345.

169. Knight, M. W.; Liu, L. F.; Wang, Y. M.; Brown, L.; Mukherjee, S.; King, N. S.; Everitt, H. O.; Nordlander, P.; Halas, N. J., Aluminum Plasmonic Nanoantennas. *Nano Letters* **2012**, 12, 6000-6004.

170. Koh, A. L.; Fernandez-Dominguez, A. I.; McComb, D. W.; Maier, S. A.; Yang, J. K. W., High-Resolution Mapping of Electron-Beam-Excited Plasmon Modes in Lithographically Defined Gold Nanostructures. *Nano Letters* **2011**, 11, 1323-1330.

171. Brüche, E., Elektronenmikroskopische Abbildung mit lichtelektrischen Elektronen, *Z. Phys.* **1933**, 86, 448.

172. Bauer, E.; Mundschau, M.; Swiech, W.; Teliëps, W., Surface Studies by Low-Energy Electron-Microscopy (Leem) And Conventional Uv Photoemission Electron-Microscopy (Peem). *Ultramicroscopy* **1989**, 31, 49-57.

173. Vogel, J.; Kuch, W.; Bonfim, M.; Camarero, J.; Pennec, Y.; Offi, F.; Fukumoto, K.; Kirschner, J.; Fontaine, A.; Pizzini, S., Time-resolved magnetic domain imaging by x-ray photoemission electron microscopy. *Applied Physics Letters* **2003**, 82, 2299-2301.

174. <http://www.physik.fu-berlin.de/einrichtungen/ag/ag-kuch/research/techniques/peem/index.html>.

175. Marsell, E.; Svard, R.; Miranda, M.; Guo, C.; Harth, A.; Lorek, E.; Mauritsson, J.; Arnold, C. L.; Xu, H. X.; L'Huillier, A.; Mikkelsen, A.; Losquin, A., Direct subwavelength imaging and control of near-field localization in individual silver nanocubes. *Applied Physics Letters* **2015**, 107, 201111.

176. Melchior, P.; Bayer, D.; Schneider, C.; Fischer, A.; Rohmer, M.; Pfeiffer, W.; Aeschlimann, M., Optical near-field interference in the excitation of a bowtie nanoantenna. *Physical Review B* **2011**, 83, 235407.

177. Lemke, C.; Leissner, T.; Jauernik, S.; Klick, A.; Fiutowski, J.; Kjelstrup-Hansen, J.; Rubahn, H. G.; Bauer, M., Mapping surface plasmon polariton propagation via counter-propagating light pulses. *Optics Express* **2012**, 20, 12877-12884.

Chapter 2

Localized surface plasmon resonance in simple nanostructures probed from near field and the fundamental applications of PEEM

2.1 Abstract

Near-field mapping, near-field spectrum, and time-resolved PEEM measurement are the three fundamental applications of PEEM to investigate the surface plasmon. To introduce how these three applications work, the localized surface plasmon resonances (LSPRs) supported on Au nanoblock structures has been investigated as an example in this chapter. Dipole plasmon mode and quadrupole plasmon mode are the two lowest orders of the LSPRs eigenmode. In classic Au nanoblock structures, the dipole plasmon mode can be easily excited by the light excitation under normal incidence. However, the quadrupole mode is forbidden when excited by linearly polarized light excitation under normal incidence. In this study, using PEEM with femtosecond laser as the excitation source, it demonstrated that the quadrupole mode in Au nanoblock structures can be excited by s-polarized light under oblique incidence. Furthermore, the results revealed that the dipole and quadrupole plasmon modes can be selectively excited by changing the polarizations of the oblique incidence light. Otherwise, by combining with pump and probe technique, the dynamics of the LSPRs have been investigated by time-resolved PEEM measurements. By using this technique, the quadrupole mode was demonstrated that it has longer dephasing time than the dipole mode. In this chapter, during the introduction of the experimental results, the fundamental applications of PEEM will be described at the same time.

2.2 Introduction

Metallic nanoparticles (NPs) can support localized surface plasmon resonances (LSPRs) which are the collective charge oscillations on the surface of the materials. When light irradiated onto a metallic NPs, LSPRs can be excited. If the size of the metallic NPs is much smaller than the irradiation wavelength, dipole plasmon mode can be excited due to the in-phase oscillation of the free electron on the surface of the NPs. However, if the size of the NPs is comparable to or even larger than the irradiation wavelength, quadrupole or multipolar plasmon modes can be excited since the free electrons at different locations can be driven by the irradiation light with different phases and oscillate in different phases.¹ Multipolar plasmon mode has been imaged on metal nanorods using scanning near-field optical microscopy (SNOM),²⁻⁴ and electron energy-loss spectroscopy (EELS).^{5, 6} Multipolar plasmon modes have specific optical properties. For example, the quadrupole plasmon mode has much less scattering loss in the far field. Thus, it has much stronger electric field enhancement in the near field.

In normal, the quadrupole plasmon mode and other even-order multipolar modes are forbidden for thin metallic NPs with symmetric geometry under the normal linearly polarized light excitation because of the symmetry selection rules. However, the quadrupole mode can be excited for some specific situations such as phase retardation or symmetry breaking.⁷⁻¹⁰ The investigation on the mapping of dipole and quadrupole LSPRs for Au nanodisks with different diameters under oblique incidence excitation using SNOM has been reported by Esteban et al.⁸ However, there is no research about the excitation of dipole and quadrupole modes on metallic NPs with same size. In particular, the quadrupole mode should produce a narrower line width which suggests that the quadrupole mode should have longer decay time than that in dipole mode. Nonetheless, there is no experimental research topic on such investigation.

Most investigations of the LSPRs are rely on the far field measurement and numerical simulation. To better understand the mechanism of the LSPRs and develop

the design of the plasmonic nanostructures, the near-field properties are crucial to be determined. Recent development of the photoemission electron microscopy (PEEM) using femtosecond laser pulses as the excitation light source has been demonstrated that PEEM is a powerful approach for pinpointing the near-field properties of localized plasmon of localized mode and propagation modes.¹¹⁻²⁰

In this study, the dipole and quadrupole plasmon modes on Au nanoblock structures have been investigated using PEEM. It demonstrated that the dipole mode and quadrupole mode can be selectively excited by changing the polarization of the oblique incident light. Furthermore, the time-resolved PEEM which is the combination of the PEEM with pump and probe technique was used to investigate the dynamic of the dipole and quadrupole modes. The results demonstrated that the quadrupole mode has longer dephasing time than the dipole mode.

Otherwise, in this chapter the fundamental applications of PEEM were also introduced in detail through the introductions of the investigations. The results further demonstrated that PEEM is a very powerful approach to investigate the near field properties of LSPRs both in the spatial domain and the temporal domain.

2.3 Experimental details

2.3.1 Sample fabrication and characterization

The Au nanoblock structures investigated in this study were fabricated by electron beam lithography (EBL) followed by metal sputtering and lift-off technique. The sample fabrication process is shown in Figure 2.1. The indium tin oxide (ITO)-coated glass substrates with an approximately 150 nm ITO layer substrate was firstly sequentially cleaned for 5 mins by acetone, methanol, and ultrapure water in ultrasonic bath. Then the substrate was spin-coated by a conventional copolymer resist (ZEP520, Zeon Chemicals) diluted with a ZEP thinner (1:1) by 1000 rpm for 10s and 4000 rpm for 90s. The spin-coated copolymer resist has an average thickness of 180 nm. After

spin-coating, the substrate was prebaked on a hot plate at 150° to remove the water element in the resist for 2 mins. An EBL system (ELS-7000HM, Elionix) operating at 100 kV was used for the EBL writing process. The EBL operated at an electrical current of 50 pA. After exposing, the development was done by ZED-N50. Then 2 nm thick Titanium layer was first deposited by sputtering (MPS-4000, ULVAC) as the adhesive layer, and then a 30 nm thickness Au film was deposited. Lift-off was performed by immersing the sample in anisole, acetone, methanol and ultra-pure water successively in an ultrasonic bath with each step for 5mins.

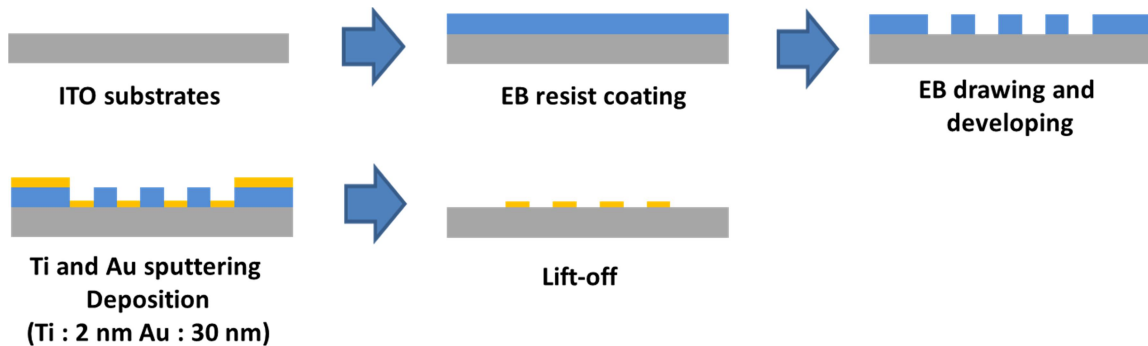


Figure 2.1 The sketch map of the sample fabrication process of Au nanostructures.

After sample fabrication, characterization of topography and far-field extinction spectra were measured by a field-emission scanning electron microscopy (SEM) (JSM-6700FT, JEOL) and a Fourier transform infrared spectrometer (FTIR) spectroscopy equipped with an infrared microscope (FT/IR-6000TM-M, JASCO), respectively. In FTIR measurement system, light was focused on the sample by a Cassegrainian objective lens, which provided angles of incidence between 16° and 32°.

2.3.2 Near-field measurements

The near-field measurements in this study were performed by PEEM. The photoemission electron microscope used here was a PEEM-III equipped with an energy analyzer (Elmitec GmbH). The sketch map of PEEM is shown in Figure 2.2. The PEEM approach has an aberration corrector, so that the spatial resolution can down to 4 nm.

The sample was settled in the main chamber with super high vacuum which can reach $\sim 10^{-11}$ Torr. And a 20 kV voltage was applied to the system to ensure most of the emitting electrons can be driven and collected by the system. Additionally, as shown in Figure 2.2 the laser pulses can irradiate onto the sample at either a fixed oblique incidence angle of 74° or normal incidence.

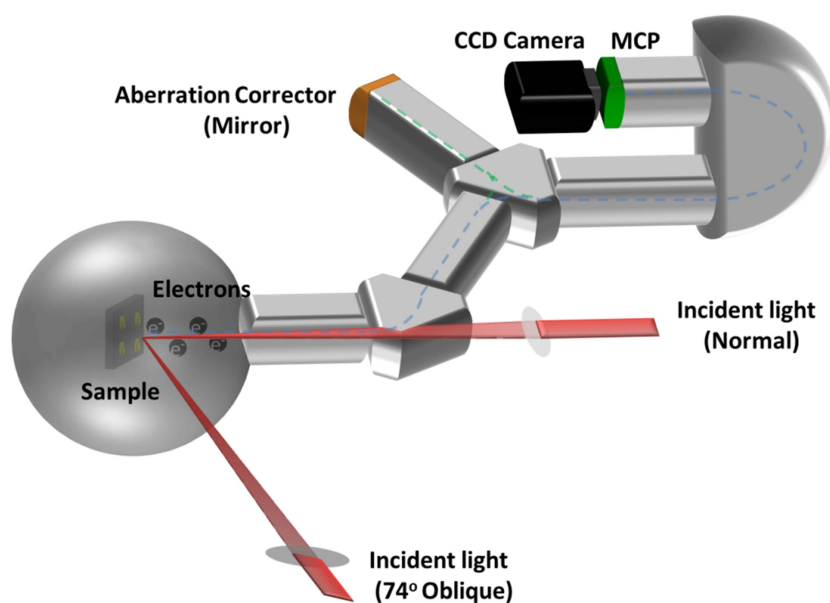


Figure 2.2 The sketch map of our PEEM system.

In this study, three kinds of light sources were employed. One beam was the UV light from a mercury lamp (unpolarized continuous wave (CW) light with a cutoff energy of 4.9 eV), which was used to characterize the morphologies of metallic nanoparticles. Since the energy of UV light is slight larger than the work function of the Au, it may light up almost entire Au nanostructures. Due to the work function contrast between the Au and substrate, the morphology of the structures can be obtained.

Second beam was a Ti:sapphire femtosecond laser that delivers approximately 100 fs laser pulses with a tunable central wavelength (720–920 nm) at a repetition rate of 77 MHz. The laser beam was focused onto the sample using a lens with a focal length of 600 mm. This laser was used for wavelength-dependent PEEM measurements to obtain the near-field photoemission spectra, as well as for near-field mapping at various

wavelengths. Since in a metallic nanostructures system, assisted by LSPR, femtosecond laser pulses provide substantial photoemission (PE) through nonlinear photoemission process mainly in multiphoton photoemission, especially when the wavelength of the laser pulses are at or close to the LSPR wavelength. In general, the probability of multiphoton photoemission is very low. For metal materials it is very difficult to catch several photons simultaneously and excite electron. However, in a plasmonic nanostructure system, when the ultra-fast femtosecond laser pluses with high peak intensity irradiating onto the structures with the wavelength of LSPRs, the near-field enhancement effect can promote the multiphoton photoemission process significantly. Because the PE intensity on the sample surface in a nonlinear manner, the PEEM image under the femtosecond laser irradiation at resonance condition of a metallic nanostructure system can be regarded as the nonlinear near-field intensity mapping of the structures. Otherwise, the near-field photoemission intensity spectrum can be treated as the nonlinear near-field LSPR response spectrum of the metallic nanostructures. PEEM can record the photoemission intensity signal from the entire field of view (FOV). By changing the irradiation wavelengths from 720 nm to 920 nm step-by-step with increments of 10 nm, a series of PEEM images can be obtained. The photoemission intensity signal from the entire FOV can be integrated and plotted against the incidence wavelength; thus, the so-called near-field PE intensity spectra can be obtained.

The third beam is a Ti:sapphire femtosecond laser (Rainbow, Femtolasers) with 7-fs laser pulse at the central wavelength of 800 nm with >200 nm bandwidth from 650 nm to 1000 nm at the repetition rate of 77 MHz. The ultra-fast laser pulse provides the application of time-resolved PEEM measurement.

The multiphoton photoemission is considered as the nonlinear photoemission process in this PEEM measurement because of the wavelength range and the laser intensity (50-100 MW/cm²). An average value of 4 is considered as the nonlinearity through this thesis. Although the nonlinearity of the photoemission can be a little different from the

wavelength between 720 nm and 920 nm and different positions of the samples, the measured near-field spectra and near-field intensity distribution can be reproduced well by finite-difference time-domain simulation results with an average nonlinearity value of 4 which will be demonstrated later in this thesis.

2.3.3 Numerical simulations

Numerical simulations of the far- and near-field properties of Au nanoblock structures were performed using the finite-difference time-domain (FDTD) simulation method by FDTD Solutions software package (Lumerical, Inc.). The optical properties of Au were obtained using the data from Johnson and Christy.²¹ The ITO-covered glass substrate was assumed to have a dielectric material with an average refractive index of 1.55. The plane wave light source was used as the light source and it located at the structure side with the light injecting down on the Au nanoblock structures. In the light propagation direction, the boundary condition was chosen to be the perfectly matched layer boundary conditions. Under normal incidence, in the plane perpendicular to the light propagation direction, the periodic boundary conditions were used for each boundary. And under the oblique incidence, the Bloch boundary condition was used. The far-field extinction spectra were obtained by a transmission power monitor located at 230 nm below the ITO layer. The near-field spectra were obtained from the maximum near-field enhancement intensity under the corresponding excitation wavelengths, as $\max. (E/E_0)^2$. The FDTD simulations were performed in a discrete, uniformly spaced mesh with 3 nm mesh size.

2.3.4 Time-resolved PEEM setup

The dynamics of the LSPRs was investigated by the time-resolved PEEM equipment. The time-resolved PEEM measurements were performed by an interferometric pump and probe technique. As shown in Figure 2.3, the laser beam passed through a

Mach-Zehnder interferometer to generate the phase-correlated pump and probe pulses. The laser beam can be divided into two beams with the absolute same phases by the interferometer. The most important point in the time-resolved study is that the delay time between the two laser pulses can be controlled. The delayed two laser pulses generated a pump and probe system and was then focused onto the sample. As adjusting the delay time between the pump and probe pulses, a series of PEEM images was recorded at a frame interval of 0.67 fs ($\pi/2$ rad with respect to the 800 nm carrier wave of the laser pulse).

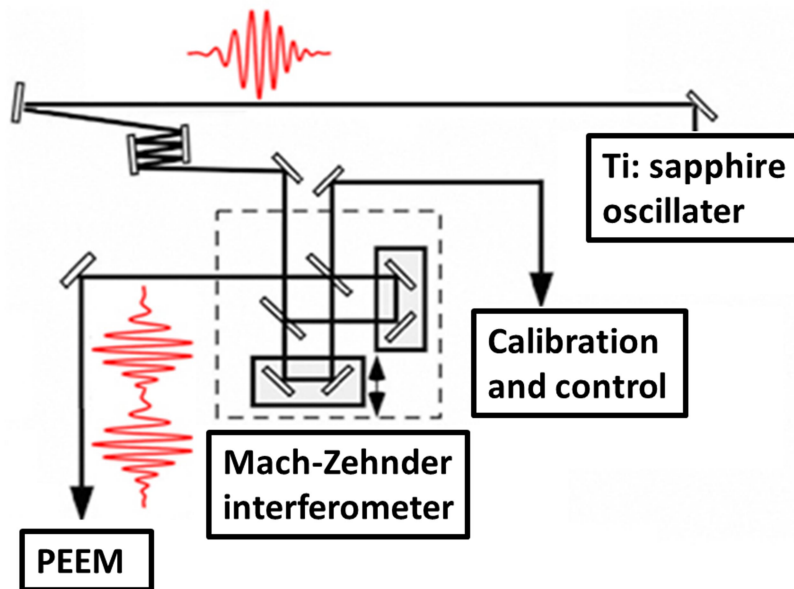


Figure 2.3 The sketch map of time-resolved PEEM.

Figure 2.4 is shown for easily understanding the principle of the time-resolved experiments. LSPRs of the metallic NPs can be excited under the irradiation of the pump pulse. Then the plasmon is oscillating following its oscillation frequency. When the probe pulse starts to irradiate the sample with the delay time, the probe pulse may also excite the oscillation of the LSPRs, and the two LSPRs fields which are excited by pump and probe pulses may interfere with each other mainly in two situations. If the two oscillating plasmons are in the same phase, constructive interference occurs. In this case, electrons can be excited and collected by PEEM. On the contrary, if the two waves are out of phase, destructive interference occurs. There will be no electron emission. As

varying the delay time between the pump and probe pulses, the oscillation of the hot spots can be observed.

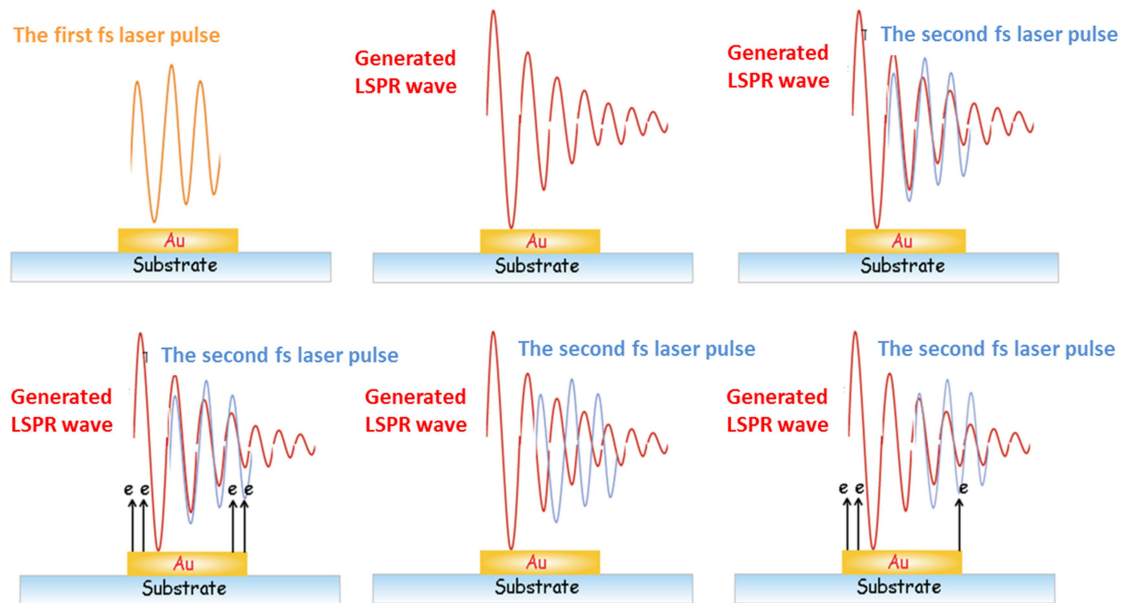


Figure 2.4 Principle sketch map of time-resolved PEEM experiments.

During the first short delay time, the pump and probe beams are overlap, the oscillation of the LSPR hot spots is almost decided by the interference of the pump and probe pulses, and it oscillates under the carrier frequency. After that, the pump and probe pulses are separated. The coherent LSPR fields which excited by the pump pulses can keep the oscillation properties of the LSPRs. And two LSPRs filed may interfere with each other, in which the two LSPRs filed were excited by the pump and probe laser pulses, respectively. Such interference may dominate the oscillation of the hot spots. Furthermore, by comprising with the numerical calculated time-resolved nonlinear photoemission signal, the decay time of the measured nanostructures can be obtained.

2.4 Results and discussion

2.4.1 Characterization of topography and far-field spectra

The Au nanoblock structures were fabricated by EBL followed by metal sputter and lift-off process. The nanoblock structures have the dimensions of $200 \times 200 \times 30 \text{ nm}^3$. The structures were arranged in a two-dimensional (2D) array with a $150 \times 150 \mu\text{m}^2$ area. The pitch size of the structures is 500 nm. Figure 2.5 (a) shows the SEM image of the nanoblock structures array. Figure 2.5 (b) shows the far-field extinction spectrum of the Au nanoblock structures measured by FTIR. In the figure, a strong and wide extinction band can be observed which located at approximately 875 nm. This peak is corresponding to the dipole LSPR of the Au nanoblock structures. Additionally, a very weak peak can be still observed at the wavelength of 765 nm. This peak is attributed to the quadrupole plasmon mode of the Au nanoblock structures. The quadrupole plasmon mode in such symmetry nanoblock structure is normally forbidden under the normal excitation. However, the light incidence was not exactly normal during the far-field extinction spectrum measurement by FTIR. As mentioned in the experimental details, the Cassegrainian objective lens provided a range of incidence angles between 16° and 32° . The oblique incidence of the excitation light makes such quadrupole mode become possible to be excited and detected by FTIR.

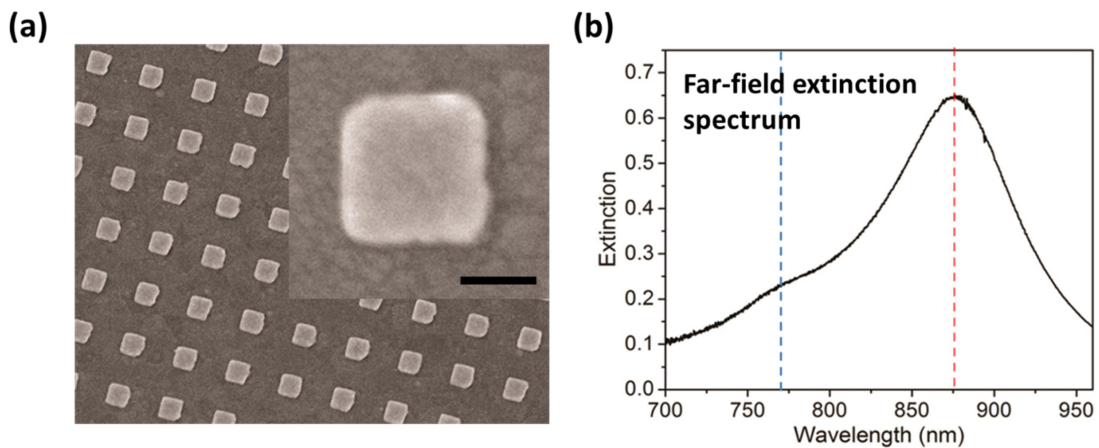


Figure 2.5 (a) SEM image of Au nanoblock structure array with the pitch size of 500 nm. The scale bar in inset is 100 nm. (b) Far-field extinction spectrum of Au nanoblock

structure measured by FTIR. The red and blue dashed lines plot the wavelength of the strong dipole and weak quadrupole peaks, respectively.

2.4.2 Near-field mapping

The near-field mapping of Au nanoblock structures was performed by PEEM with the wavelength-tunable femtosecond laser source (720 nm to 920 nm). Figure 2.6 (a) shows the PEEM image of Au nanoblock structure under the femtosecond laser pulses with a central wavelength of 860 nm at normal incidence. Here the field of view is 0.75 μm which ensures only single particle is imaged. The figure shows that four hot spots from the nanoblock structure can be clearly observed. This result was similar to the previous observation on Au nanorod structures.¹⁷ However, it is very difficult to distinguish the exact location of the hot spots only from this PEEM image. To further confirm where the hot spots emitted from, a UV light from mercury lamp was used also. Figure 2.6 (b) shows the PEEM image of Au nanoblock structure irradiated by the femtosecond laser pulses and UV light, simultaneously. From this image, the hot spots were excited from the four corners of the Au nanoblock structure can be clearly observed. Since irradiated by the UV light, the morphology of the structures can be obtained as shown in Figure 2.6 (c). As mentioned in the experimental details, the UV light lead to a one-photon photoemission process of the Au nanostructures, since the photon energy of the UV light is slight larger than the work function of the Au. Also due to the work function contrast between the Au and the substrate, the PEEM image under the UV light irradiation can perform the geometry of the nanostructures. This method provides a new way for PEEM experiments to determine the exact location of the hot spots (near-field enhancement). In a metallic nanostructures system under the femtosecond laser irradiation, assisted by LSPR, it provide substantial photoemission through nonlinear photoemission process mainly in multiphoton photoemission, especially when the wavelength of the laser pulses are at or close to the LSPR wavelength. The PEEM image under the femtosecond laser irradiation at resonance condition of a metallic

nanostructure system can be regarded as the nonlinear near-field intensity mapping of the structures. Thus, through the near-field mapping, the near-field properties of near-field enhancement for metallic nanostructures with different wavelength excitation can be obtained.

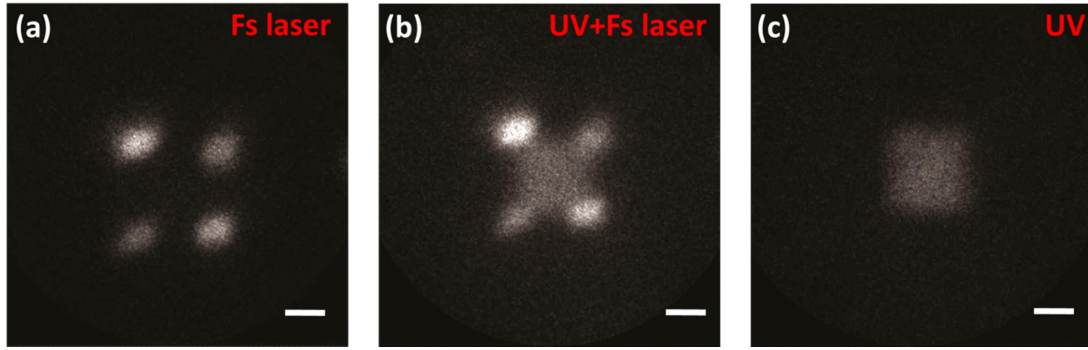


Figure 2.6 PEEM images (FOV of $0.75\ \mu\text{m}$) of Au nanoblock structures with different light sources. (a) Femtosecond laser at 860 nm wavelength under normal incidence. (b) Femtosecond pulses and UV light from a mercury lamp. (c) UV light from a mercury lamp. The scale bars are 100 nm.

Based on above discussions, the wavelength-dependent near-field properties of the Au nanoblock structures under normal incidence and oblique incidence with 74° incidence angle have also been investigated. Firstly, by changing the excitation wavelengths and the excitation conditions, a series of PEEM images can be obtained. In Figure 2.7, selected PEEM images under different wavelength excitations and light conditions (normal incidence, p-polarization at oblique incidence, and s-polarization at oblique incidence) were shown. Under oblique incidence, p-polarization means the electric field of the light is parallel to the plane of incidence, while the p-polarized light has the light component along the horizontal direction. Contrary, the s-polarization means the electric field of the light is perpendicular to the plane of incidence, while the s-polarization is almost totally along the vertical direction as shown in the above part of Figure 2.7. In Figure 2.7, all the PEEM images are in same contrast. It is easily found that, the PEEM images have stronger photoemission intensity under the 860 nm wavelength excitation both at normal incidence and oblique incidence with p-polarization. In contrast, it is very weak for s-polarization excitation under the 860 nm

wavelength irradiating. However, the PEEM image shows strong photoemission at the wavelength of 760 nm under oblique incidence with s-polarization. It seemed that a new mode other than the dipole mode was excited at this situation. To further understanding, near-field spectra are necessary.

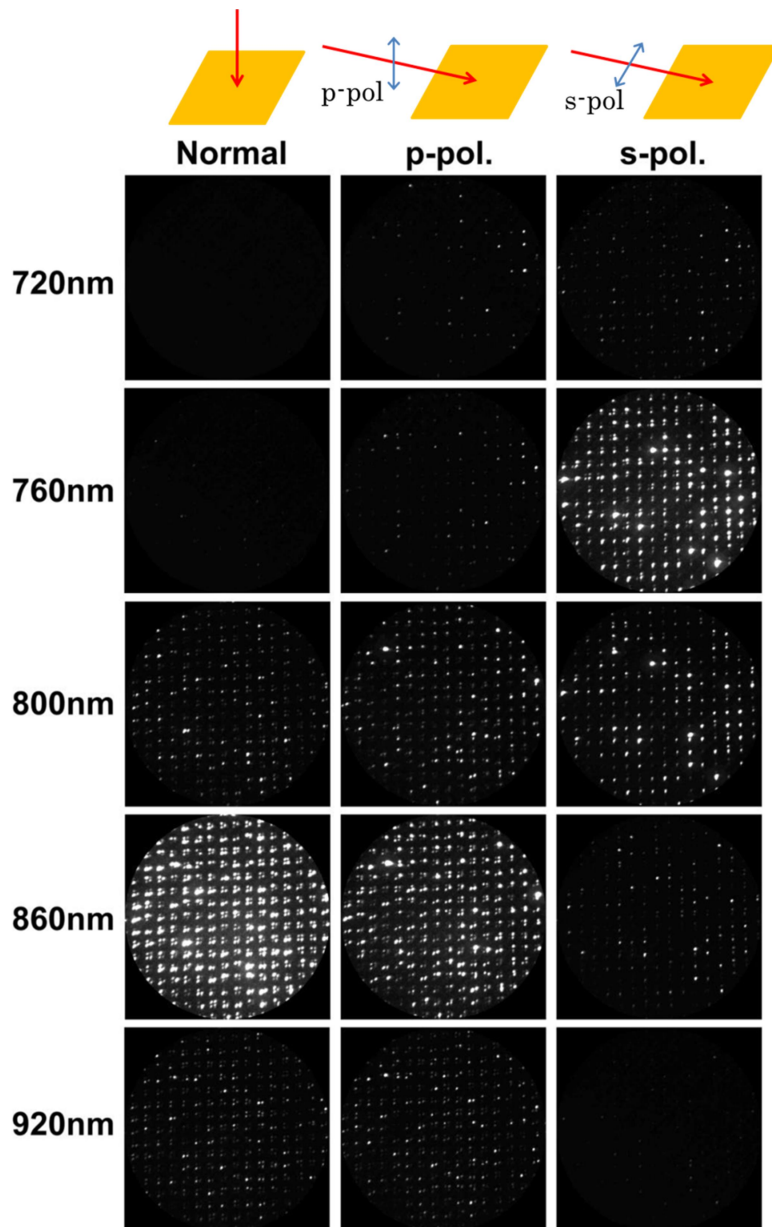


Figure 2.7 PEEM images of Au nanoblock structure irradiated by different light conditions with different wavelengths. The figure at top plots the sketch maps of the light conditions: normal incidence, p-polarized oblique incidence, and s-polarized oblique incidence. The p-polarization incidence light means the electric field of the light is parallel to the plane of incidence, while the s-polarization incidence light means the electric field of the light is perpendicular to the plane of incidence.

2.4.3 Near-field spectra

As mentioned and the figure showed above, a series of PEEM images can be obtained by changing the excitation wavelength from 720 nm to 920 nm with the incensement of 10 nm under the three excitation conditions. By integrating the photoemission signal and plotting it against the incidence wavelength, the so-called near-field spectrum can be obtained. Since the photoemission intensity is correlated with the near-field electric field intensity, the near-field photoemission intensity spectrum can be treated as the nonlinear near-field LSPR response spectrum of the metallic nanostructures.

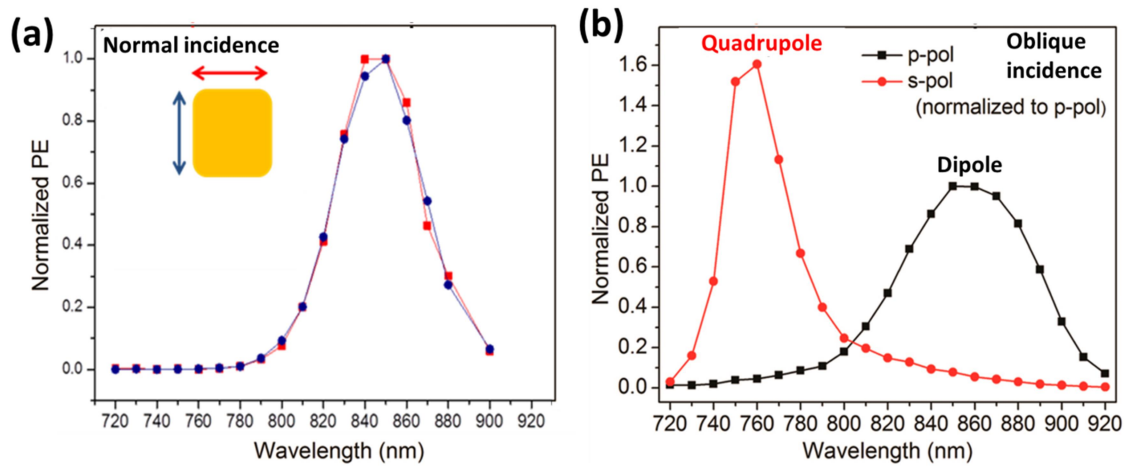


Figure 2.8 Near-field spectra of Au nanoblock structures under normal incidence with horizontal polarization (red) and vertical polarization (blue) (a) and under oblique incidence with p-polarization (black) and s-polarization (red) (b). In (b) the two curves were normalized to the maximum photoemission intensity under p-polarized laser excitation.

Figure 2.8 (a) shows the near-field spectra of Au nanoblock structures under normal incidence with horizontal polarization excitation (red) and vertical polarization excitation (blue). The two curves all show one peak located at around 860 nm which is almost the same wavelength in the far-field extinction spectrum shown in Figure 2.5 (b). It demonstrated that under the normal incident light, only dipole plasmon mode can be excited at both horizontal and vertical polarization excitation conditions. Figure 2.8 (b) shows the near-field spectra of Au nanoblock structures at oblique incidence with p-polarized (black) and s-polarized (red) excitations. The different polarization states of

the oblique incident light resulted in different near-field spectra. Under the p-polarized irradiation, only the dipole mode which located at the wavelength of 860 nm was excited. However, under the s-polarized irradiation, dipole plasmon peak cannot be observed. On the contrary, a quadrupole plasmon peak located at the wavelength of 760 nm can be observed. Since the two curves were normalized to the maximum photoemission intensity under p-polarized laser excitation, the near-field enhancement of the quadrupole mode was much stronger than the dipole mode can be clearly observed.

2.4.4 Numerical simulation results

To explain the experimental observation, numerical simulation results have been done by FDTD simulation. Figure 2.9 shows the numerical simulated near-field intensity spectra (the maximum near-field enhancement factor against the excitation wavelength) under the oblique incidence with p-polarized light (black) and s-polarized light (red). Under p-polarized light excitation, only a dipole plasmon mode located at approximately 900 nm can be observed. Under s-polarized light excitation, a quadrupole plasmon mode at 750 nm was excited. The experimental results reproduce well with the FDTD simulation results. It is also noted that the calculated near-field enhancement of the quadrupole mode is larger than that of the dipole mode. This result qualitatively agreed with the experimental result.

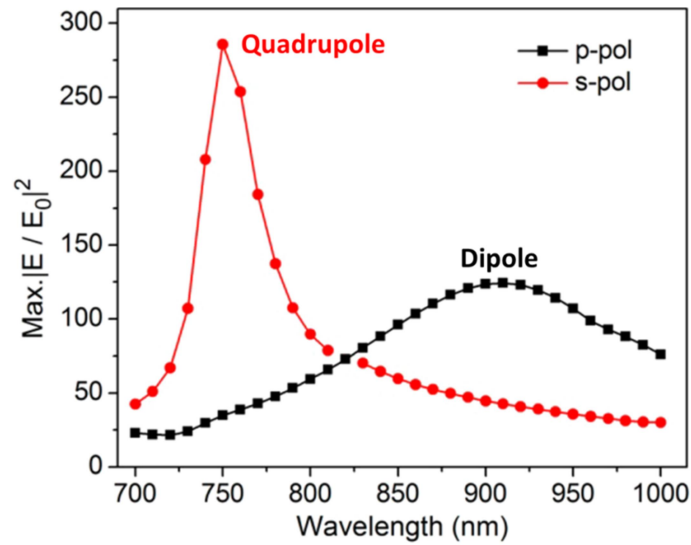


Figure 2.9 FDTD numerical simulated near-field spectra of Au nanoblock structures under the oblique incidence with p-polarized light excitation (black) and s-polarized light excitation.

Figure 2.10 shows the calculated electric field intensity distributions (left) and charge distributions (right) for both p-polarized and s-polarized light excitations at the corresponding peak wavelengths. The near-field electric field intensity distributions reproduce well with the PEEM images under the corresponding wavelength excitations. Furthermore, the charge distribution under p-polarized excitation performs an in-phase distribution along the in-plane direction of the light polarization; it indicates the mode belongs to a dipole plasmon mode. However, under the s-polarized excitation, the charge distribution shows an out-of-phase distribution, it indicates that this mode belongs to the quadrupole mode.

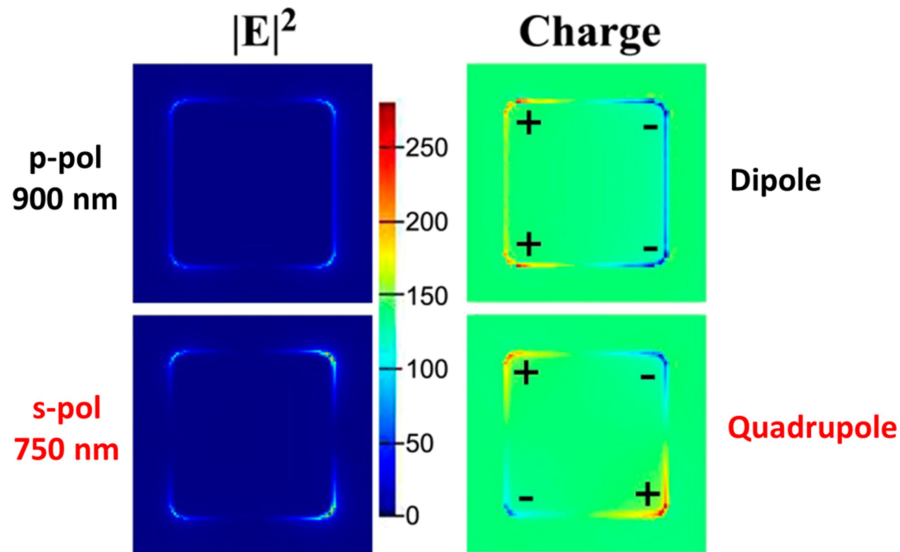


Figure 2.10 Left column shows the calculated electric field intensity distributions corresponding to the dipole and quadrupole peak wavelength excitations. Right column shows the calculated charge distributions for both p-polarized and s-polarized light excitation at the peak wavelengths.

It is noted that no clear dipole peak was observed in the near-field spectra under s-polarized light excitation either the experimental results or the simulated results. It is because of the significant damping which resulted from the large phase retardation effect at grazing incidence. From the results, it can be concluded that the dipole plasmon mode and quadrupole plasmon mode can be selectively excited by changing the polarization of the oblique incident light.

2.4.5 Dynamics of localized surface plasmon resonance investigated by time-resolved PEEM

Form the experimental and simulation near-field spectra, it can be found that the bandwidth of the quadrupole mode is narrower than that of the dipole mode. It is noted that the near-field spectra were obtained by scanning the laser wavelength at the step of 10 nm and during tuning the wavelength, the pulse duration, the focal spot, and the nonlinear order can be slightly changes. It is difficult to estimate the spectral line width and to infer the dephasing time of the LSPRs, since it is difficult to obtain the real linear

near-field intensity spectra. However, it can be qualitatively found that the bandwidth of the quadrupole mode is narrower than the dipole mode. It can be deduced that the quadrupole mode should have longer dephasing time than the dipole mode. To confirm this, time-resolved PEEM has been established.

As mentioned in the experimental details, the time-resolved PEEM is the combination of PEEM with an interferometric pump and probe technique. Here, a Mach-Zehnder interferometer is employed to support the pump and probe pulses. A series of PEEM images were recorded by adjusting the delay between the pump and probe pulses. Like the near-field spectra, by integrating the photoemission intensity of each PEEM image and plotting against the delay time, the time evolution of photoemission intensity curves can be obtained.

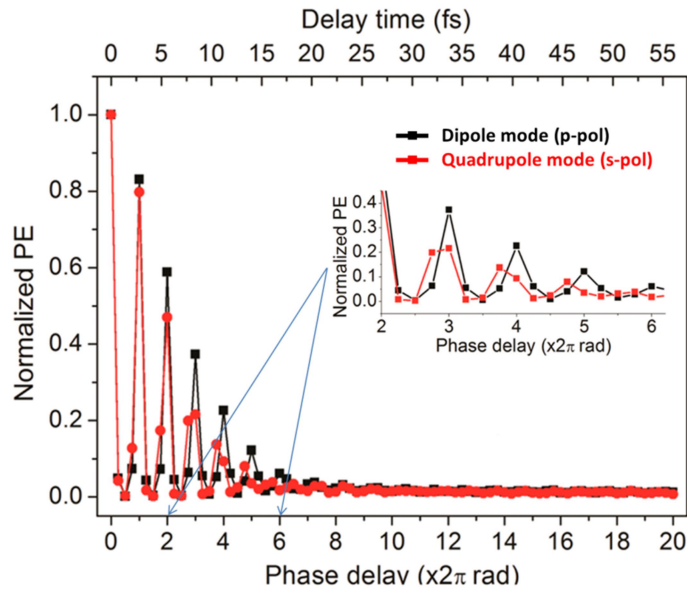


Figure 2.11 Time evolution of the photoemission intensity for both p-polarized and s-polarized light excitation within the phase delay of $(0-20) \times 2\pi$ rad (corresponding to the delay time of 0-56 fs)

Figure 2.11 shows the time evolution of the photoemission intensity of Au nanoblock structures for both p-polarized and s-polarized light excitation within the phase delay time of 0-56 fs. As can be seen in the figure, the two curves firstly oscillate at the same frequency which corresponds to the laser carrier frequency. After that, the oscillation of

the two curves are separated (as shown in the inset), since in this situation the oscillation of each curve is charged by the interference of the two LSPR fields excited by the pump and probe pulses, respectively. In this region, the oscillation is corresponding to the decay of the plasmon modes excited separately by p-polarized and s-polarized light excitation. However, the information showed in the figure cannot reflect the dephasing time of the dipole mode and quadrupole mode. Since if it is assumed that the two plasmon modes have the same plasmon resonance frequency but different dephasing time, the two LSPR fields induced by the pump and probe can interfere with each other at relatively longer time of the plasmon mode has longer dephasing time. Buy here, the dipole mode and quadrupole mode have different plasmon resonance frequencies, it is not possible to compare the dephasing time of this two modes by simply comparing the width of the time-resolved photoemission curves. To confirm the dephasing time, numerical simulations are necessary.

Here, the numerical calculation of the time-resolved nonlinear photoemission signal is calculated by employing a plasmon oscillator model with an exponential damping term including the nonlinearity of the photoemission.^{22, 23} In the calculation, two important parameters were necessary. One is the driving electric field $E(t) + E(t + t_d)$, where t_d is the time delay between the pump and probe pulses. In this experiment, $E(t)$ was determined by the sech^2 -shaped pulse with the pulse duration of 7 fs of the fs laser. Another parameter is the nonlinear photoemission order. Here the average nonlinear order for dipole mode and quadrupole mode are 3.7 and 3.6, respectively. The values were obtained from the peak to background ratio in the two time-resolved photoemission curves. The values are in accordance with recently reported value of 3.5.²⁴ After determined the two important parameters, the time-resolved nonlinear photoemission signal can be calculated with changing the fitting parameter of dephasing time. The details of the calculation are as following:

A simple damped harmonic oscillator mode was employed to model the time dependent surface plasmon field.²² The plasmon field $E_{pl}(t)$ can be described as

following:

$$E_{pl}(t) \propto \int_{-\infty}^t \frac{1}{\omega_0} K(t') e^{-\gamma(t-t')} \sin[\omega_0(t-t')] dt' \quad (2-1)$$

In the equation, $K(t)$ is the driving field which can be expressed as $K(t) = E(t) + E(t + t_d)$ in the case of interferometric pump-probe measurements in this investigation. t_d represents the delay between the pump and probe pulses. ω_0 denotes the plasmon resonance frequency. $\gamma = 1/2T$, where T means the dephasing time of the plasmon field. Since the nonlinearity of the photoemission should be considered in this study, the delay time t_d dependent photoemission intensity can be given by:

$$I(t_d) \propto \int_{-\infty}^{+\infty} |E_{pl}(t)|^{2N} dt \quad (2-2)$$

Where N means the nonlinear order of the photoemission and it was assumed as 3.7 for dipole mode and 3.6 for quadrupole mode.

By using these two equations with the parameters, the photoemission intensity as a function of the t_d can be calculated. By changing the dephasing time and excitation wavelengths, several calculated time-resolved photoemission signal curves have been obtained. As an example, Figure 2.12 (a-d) shows the results for fixed LSPR wavelength of 860 nm with different dephasing time. The calculated time-resolved photoemission signal for fixed dephasing time of 9 fs but different wavelengths are shown in the panels (e-f) of Figure 2.12. By comparing the calculated results with the experimental results, the best fitted T value can be obtained.

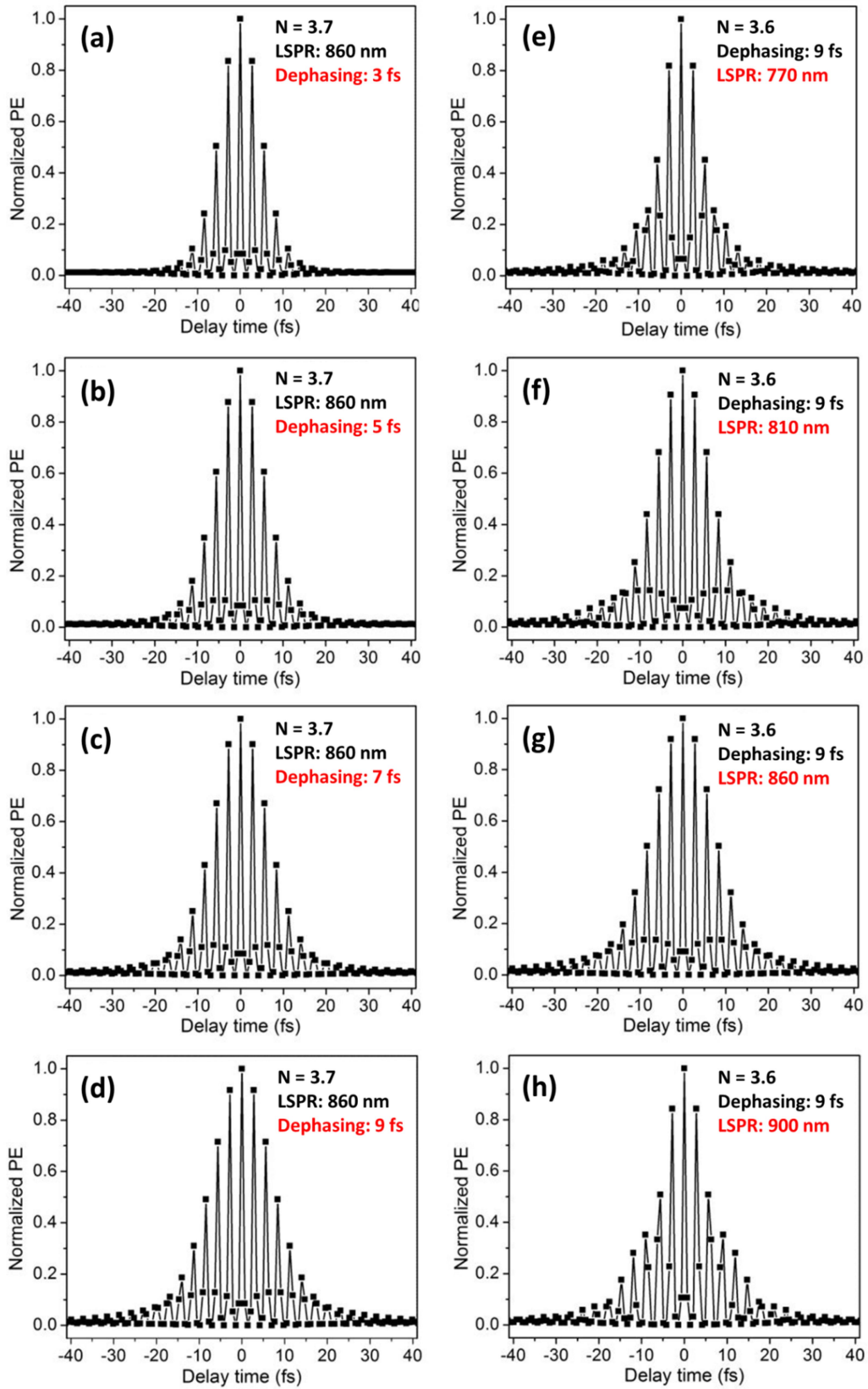


Figure 2.12 Several calculated time-resolved photoemission signal for fixed LSPR wavelength of 860 nm with different dephasing time are shown in panels (a-d). The

calculated time-resolved photoemission signal for fixed dephasing time of 9 fs but different wavelengths are shown in the panels (e-f).

Among the simulated time-resolved photoemission intensity curves for both the p-polarized and s-polarized light excitation, it is found that the resulting simulated curves yielded the best fitted dephasing time of 5 fs (shown in Figure 2.13 (a)) for dipole plasmon mode and 9 fs (shown in Figure 2.13 (b)) for quadrupole plasmon mode. It has been demonstrated that the dipole and quadrupole plasmon modes could be selectively excited by changing the light polarization between p-polarization and s-polarization. Otherwise, it was also demonstrated that the photoemission was dominated by the dipole and quadrupole LSPR fields under p-polarized and s-polarized light incidence, respectively. It can be concluded that the quadrupole plasmon mode has a longer dephasing time than the dipole mode.

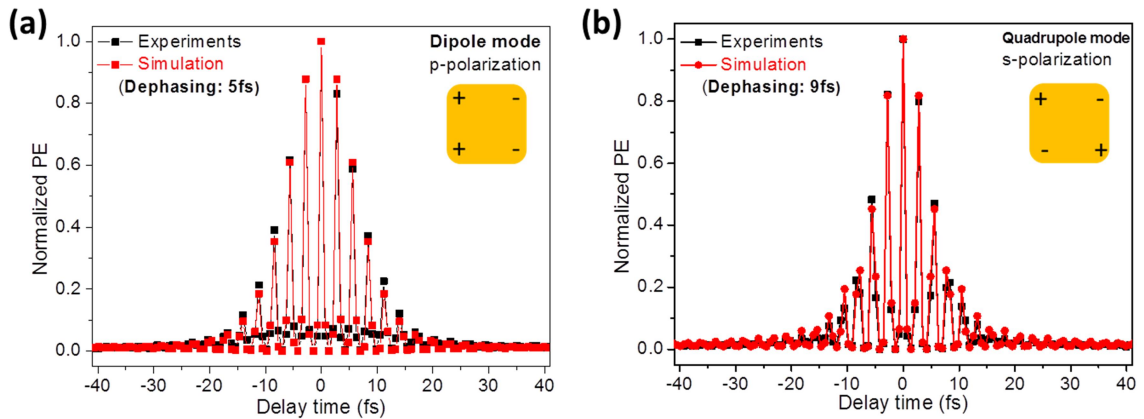


Figure 2.13 Experimental (black) and numerical simulated (red) photoemission intensity for dipole mode (a) and quadrupole mode (b) as a function of the delay time between pump and probe pulses.

In this study, the quadrupole mode and dipole mode are far from the interband transition region leading to negligible contribution to the damping. Thus, the damping from the intraband excitation can be thought to be similar. However, the radiative damping of the quadrupole mode is suppressed due to the less net dipole moment. This leads to a longer dephasing time of quadrupole mode than the dipole mode.

2.5 Conclusions

In this chapter, the near-field properties of dipole plasmon mode and quadrupole plasmon mode on Au nanoblock structures have been investigated using PEEM through the near-field mapping, near-field spectrum and time-resolved PEEM measurement which are the three fundamental applications of PEEM for investigating the surface plasmon resonance. From the near-field mapping and near-field spectrum results, it demonstrated that the quadrupole plasmon mode and dipole plasmon mode can be selectively excited by changing the polarization of the oblique incident light. Under p-polarization, the dipole plasmon was excited and dominated the near field enhancement. Under s-polarization, the quadrupole mode dominated the near-field enhancement with much higher values than the dipole mode. Furthermore, time-resolved PEEM allows to investigate the ultra-fast dynamics of the LSPRs. By using the technique, the quadrupole plasmon mode was demonstrated that has longer dephasing time than the dipole plasmon mode. The results deepen our understanding of the plasmon modes especially the quadrupole mode. Using PEEM to investigate the near field properties of LSPRs paves a new way to investigate the plasmonic systems both in spatial domain and temporal domain.

2.6 References

1. You, E. A.; Zhou, W.; Suh, J. Y.; Huntington, M. D.; Odom, T. W., Polarization-Dependent Multipolar Plasmon Resonances in Anisotropic Multiscale Au Particles. *ACS Nano* **2012**, 6, 1786-1794.
2. Imura, K.; Nagahara, T.; Okamoto, H., Plasmon Mode Imaging of Single Gold Nanorods. *Journal of the American Chemical Society* **2004**, 126, 12730-12731.
3. Imura, K.; Nagahara, T.; Okamoto, H., Near-Field Optical Imaging of Plasmon Modes in Gold Nanorods. *Journal of Chemical Physics* **2005**, 122, 154701.
4. Denkova, D.; Verellen, N.; Silhanek, A. V.; Valev, V. K.; Van Dorpe, P.; Moshchalkov, V. V., Mapping Magnetic Near-Field Distributions of Plasmonic Nanoantennas. *ACS Nano* **2013**, 7, 3168-3176.
5. Rossouw, D.; Couillard, M.; Vickery, J.; Kumacheva, E.; Botton, G. A., Multipolar Plasmonic Resonances in Silver Nanowire Antennas Imaged with a Subnanometer Electron Probe. *Nano Letters* **2011**, 11, 1499-1504.
6. Martin, J.; Kociak, M.; Mahfoud, Z.; Proust, J.; Gerard, D.; Plain, J., High-Resolution Imaging and Spectroscopy of Multipolar Plasmonic Resonances in Aluminum Nanoantennas. *Nano Letters* **2014**, 14, 5517-5523.
7. Hao, F.; Larsson, E. M.; Ali, T. A.; Sutherland, D. S.; Nordlander, P., Shedding Light on Dark Plasmons in Gold Nanorings. *Chemical Physics Letters* **2008**, 458, 262-266.
8. Esteban, R.; Vogelgesang, R.; Dorfmueller, J.; Dmitriev, A.; Rockstuhl, C.; Etrich, C.; Kern, K., Direct Near-Field Optical Imaging of Higher Order Plasmonic Resonances. *Nano Letters* **2008**, 8, 3155-3159.
9. Zhang, Y.; Jia, T. Q.; Zhang, S. A.; Feng, D. H.; Xu, Z. Z., Dipole, Quadrupole and Octupole Plasmon Resonance Modes in Non-Concentric Nanocrescent/Nanodisk Structure: Local Field Enhancement in the Visible and Near Infrared Regions. *Optics Express* **2012**, 20, 2924-2931.
10. Fang, Z. Y.; Cai, J. Y.; Yan, Z. B.; Nordlander, P.; Halas, N. J.; Zhu, X., Removing a Wedge from a Metallic Nanodisk Reveals a Fano Resonance. *Nano Letters* **2011**, 11, 4475-4479.
11. Aeschlimann, M.; Brixner, T.; Fischer, A.; Kramer, C.; Melchior, P.; Pfeiffer, W.;

Schneider, C.; Struber, C.; Tuchscherer, P.; Voronine, D. V., Coherent Two-Dimensional Nanoscopy. *Science* **2011**, 333, 1723-1726.

12. Kubo, A.; Onda, K.; Petek, H.; Sun, Z. J.; Jung, Y. S.; Kim, H. K., Femtosecond Imaging of Surface Plasmon Dynamics in a Nanostructured Silver Film. *Nano Letters* **2005**, 5, 1123-1127.

13. Kubo, A.; Pontius, N.; Petek, H., Femtosecond Microscopy of Surface Plasmon Polariton Wave Packet Evolution at the Silver/Vacuum Interface. *Nano Letters* **2007**, 7, 470-475.

14. Lemke, C.; Schneider, C.; Leissner, T.; Bayer, D.; Radke, J. W.; Fischer, A.; Melchior, P.; Evlyukhin, A. B.; Chichkov, B. N.; Reinhardt, C.; Bauer, M.; Aeschlimann, M., Spatiotemporal Characterization of SPP Pulse Propagation in Two-Dimensional Plasmonic Focusing Devices. *Nano Letters* **2013**, 13, 1053-1058.

15. Schertz, F.; Schmelzeisen, M.; Mohammadi, R.; Kreiter, M.; Elmers, H. J.; Schonhense, G., Near Field of Strongly Coupled Plasmons: Uncovering Dark Modes. *Nano Letters* **2012**, 12, 1885-1890.

16. Cinchetti, M.; Gloskovskii, A.; Nepjiko, S. A.; Schonhense, G.; Rochholz, H.; Kreiter, M., Photoemission Electron Microscopy as a Tool for the Investigation of Optical Near Fields. *Physical Review Letters* **2005**, 95, 047601.

17. Sun, Q.; Ueno, K.; Yu, H.; Kubo, A.; Matsuo, Y.; Misawa, H., Direct Imaging of the Near Field and Dynamics of Surface Plasmon Resonance on Gold Nanostructures Using Photoemission Electron Microscopy. *Light-Science & Applications* **2013**, 2, e118.

18. Sun, Q.; Yu, H.; Ueno, K.; Sun, Q.; Yu, H.; Ueno, K.; Kubo, A.; Matsuo, Y.; Misawa, H., Dissecting the Few-Femtosecond Dephasing Time of Dipole and Quadrupole Modes in Gold Nanoparticles Using Polarized Photoemission Electron Microscopy. *ACS Nano* **2016**, 10, 3835-3842.

19. Han Yu, Q. S., Kosei Ueno, Tomoya Oshikiri, Atsushi Kubo, Yasutaka Matsuo, Hiroaki Misawa, Exploring Coupled Plasmonic Nanostructures in the Near Field by Photoemission Electron Microscopy. *ACS Nano* **2016**, 10, 10373-10381

20. Lecarme, O.; Sun, Q.; Ueno, K.; Misawa, H., Robust and Versatile Light Absorption at Near-Infrared Wavelengths by Plasmonic Aluminum Nanorods. *ACS Photonics* **2014**, 1, 538-546.

21. Johnson, P. B.; Christy, R. W., Optical Constants Of Noble Metals. *Phy. Rev. B*

1972, 6, 4370-4379.

22. Lamprecht, B.; Krenn, J. R.; Leitner, A.; Aussenegg, F. R., Resonant and Off-Resonant Light-Driven Plasmons in Metal Nanoparticles Studied by Femtosecond-Resolution Third-Harmonic Generation. *Physical Review Letters* **1999**, 83, 4421-4424.

23. Hanke, T.; Krauss, G.; Trautlein, D.; Wild, B.; Bratschitsch, R.; Leitenstorfer, A., Efficient Nonlinear Light Emission of Single Gold Optical Antennas Driven by Few-Cycle Near-Infrared Pulses. *Physical Review Letters* **2009**, 103, 257404.

24. Marsell, E.; Losquin, A.; Svard, R.; Miranda, M.; Guo, C.; Harth, A.; Lorek, E.; Mauritsson, J.; Arnold, C. L.; Xu, H. X.; L'Huillier, A.; Mikkelsen, A., Nanoscale Imaging of Local Few-Femtosecond Near-Field Dynamics within a Single Plasmonic Nanoantenna. *Nano Letters* **2015**, 15, 6601-6608.

Chapter 3

Plasmon hybridization in coupled dolmen structures

3.1 Abstract

In a coupled plasmon nanostructure system, the extraordinary optical properties make these materials potentially useful in many applications; these materials have received a growing level of attention in basic and applied research. Optical properties of the coupled plasmon modes have been characterized mainly by far-field spectroscopy and numerical simulation. The spectral response of the local field enhancement in coupled plasmonic nanostructures remains largely unexplored in near-field spectroscopy. In this chapter, the near-field properties of complex coupled gold dolmen nanostructures have been investigated by photoemission electron microscopy (PEEM) using a wavelength tunable femtosecond laser pulses as an excitation source. The dolmen structures are classic nanostructures which were thought to support Fano resonance in former works. In this study, the spatial evolution of near-field mapping of an individual dolmen structure with the excitation wavelength was obtained. An anti-bonding plasmon mode and a bonding mode as the result of plasmon hybridization were spatially resolved in the near field. Furthermore, from the spatially resolved near-field spectra, the quadrupole-like plasmon mode that could be involved in the formation of a Fano resonance was also revealed. However, this quadrupole-like plasmon mode only weakly contributed to the total near-field enhancement. The findings demonstrated that the hybridization plasmon modes in dolmen structures dominate the near field enhancement rather than Fano resonance. The results deepen our understanding of the near-field properties of complex plasmonic nanostructures.

3.2 Introduction

In recent years, the advances in synthesis and nanofabrication technique allow for the preparation of metallic NPs with nanometer accuracy and complex shapes by several methods. The complex plasmonic NPs that resemble NPs with small gap distance also can be fabricated. Such kinds of complex nanostructures can induce plasmon coupling and result in larger field enhancement. Some striking properties can also be generated, such as plasmon hybridization,^{1,2} Fano resonance,³⁻¹⁵ plasmonic waveguiding,^{16,17} and electromagnetically induced transparency (EIT).¹⁸ These specific properties may extremely improve the performances of the plasmonic applications and even new application can be created.

Among the wide applications of LSPRs, many of them rely on the near-field properties of the plasmonic nanostructures. The large field enhancements of plasmonic modes make particular benefits for plasmon-enhanced photochemical reactions¹⁹⁻²¹ and plasmon-enhanced nonlinear optical effects.²²⁻²⁵ The complex coupled nanostructures have much more complicated plasmon resonance line-shape in far field and much richer near-field properties compared with the simple individual nanostructures. The near field mapping which reveal the near field enhancement distribution and the near field spectrum are the two topics of the near field properties. In particular, the spatially resolved spectral response of coupled plasmonic nanostructures with different plasmon modes is in high demand. Till now, there are few attempts have been reported by using scanning near-field optical microscopy (SNOM),⁷ electron energy loss spectroscopy (EELS) and Cathodoluminescence (CL)^{10,26,27} to investigate the near field of complex plasmonic nanostructures. Photoemission electron microscopy (PEEM) using femtosecond laser pulses as the excitation light source supports another choice to investigate the near-field properties on complex coupled plasmonic nanostructures. PEEM has been found promising for pinpointing the near-field properties of plasmonic modes on different metallic nanostructures.²⁸⁻³⁶

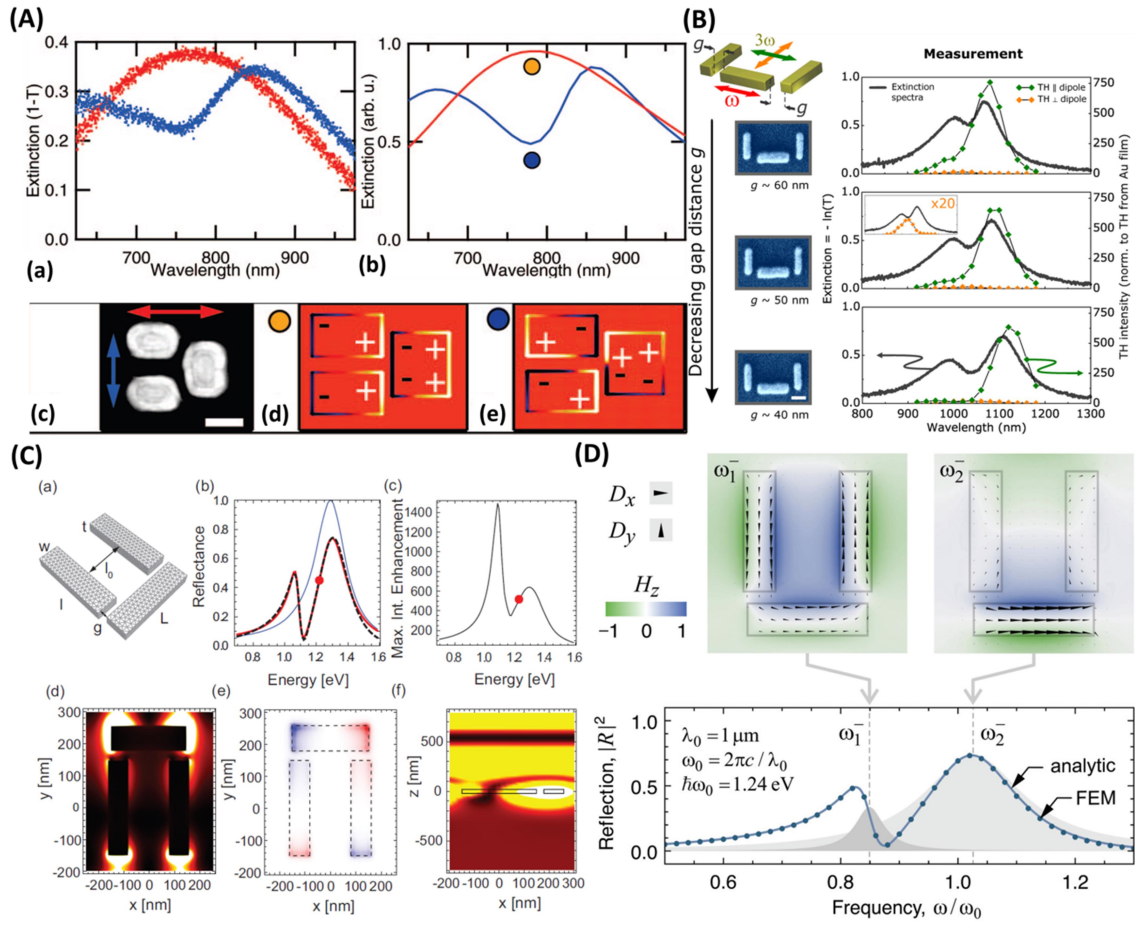


Figure 3.1 The investigations of spectral properties in dolmen structures on the basis of far-field spectroscopic measurements and numerical simulations. (A) Investigation on dolmen structures in experimental and numerical simulation in far field.¹⁴ Under horizontal polarized light excitation, one broad extinction peak can be observed due to the dipole mode for entire structure. Under vertical polarization excitation, two peaks and a dip can be observed in both the experimental and simulated results shown in (a) and (b), respectively. The near-field charge distribution demonstrated that a quadrupole mode in dimer part can be obtained under the dip wavelength excitation (e). (B) Investigation of Fano resonance on dolmen structures by third harmonic mechanism.¹⁵ (C) Investigation of Fano resonance on dolmen structures in experimental, calculations and numerical simulations.³⁷ (D) Theoretical investigation of Fano resonance on dolmen structures. The researches above all obtained two peaks and a dip in far field spectra.³⁸ The near-field properties were only performed through the calculation and simulation.

Au nano dolmen structure consists of a planar monomer nanorod and a two parallel planar nanorods (dimer) is a popular complex plasmonic nanostructures, since it exhibit striking spectral properties in far field and have been primarily explained by the Fano

resonance as the result of interference between a spectral wide dipole plasmon mode and a narrow dark quadrupole plasmon mode.^{8, 10, 14} In normal, the quadrupole plasmon mode in dimer part cannot be excited since it is a forbidden mode and it hard couples to the far field. However when the monomer part close to the dimer part, the dipole mode in monomer part may induce the quadrupole mode in dimer part due to the near-field interaction (near-field coupling). The Fano resonance can be generated from the interference between these two modes. The spectral properties of dolmen structures have been intensively investigated on the basis of far-field spectroscopic measurements and numerical simulations. Figure 3.1 shows several investigations of Fano resonance on dolmen structures by several methods in experiments, numerical simulations, and theoretical calculations.^{14, 15, 37, 38} The results all indicated that in far-field spectra two peaks and a dip can be observed under the polarized excitation perpendicular to the symmetry axis of dolmen structures. Only few attempts of investigations on near-field properties, but they were all in calculations or simulations. Since the plasmon hybridization and Fano resonance mix with each other and it is difficult to distinguish only in far field spectra. Therefore, in near field, the spectral response of the local field enhancement in plasmonic Fano nanostructures is extremely desired to be explored.

In this chapter, the near-field spectral response and spatial evolution of the near-field intensity distribution on complex coupled dolmen structures have been investigated by PEEM. According to the near-field properties of dolmen structures, the spectral response of dolmen structures is primarily attributable to the anti-bonding plasmon mode and bonding plasmon mode that are thought to result from plasmon hybridization. Upon the high spatial resolution of the PEEM, spatially resolved near-field spectral response of dolmen structures has been obtained. In particular, the near-field spectra demonstrated that the maximum near-field enhancement is dominated by the anti-bonding and bonding hybridized modes, although the quadrupole-like mode can be revealed from the spatially resolved near-field photoemission spectra, it only weakly contribute to the near-field enhancement. The experimental results can be reproduced

well with the finite-difference time-domain (FDTD) method. On the basis of the results, the discussion of the crossover between plasmon hybridization and Fano resonance was also described. And a new method for distinguishing the plasmon hybridization and Fano resonance is concluded. It is the near-field properties especially the near-field spectra can be used to clarify the crossover between the plasmon hybridization and Fano resonance.

3.3 Experimental details

The LSPRs is highly dependent on the shape of the metallic nanoparticles, in dolmen structure system the constitution elements of three nanorods provide twelve corners. Since the plasmon coupling between the constitution elements decide the spectral properties in dolmen structure, the shapes of the nanorods and the corners play a very important role. To increase and ensure the quality of the structures, in this study I employed another EBL approach (ELS-F130MH, Elionix) to fabricate the sample. The fabrication process is almost the same as described in chapter 2. Here, EBL writing was performed at 130 kV acceleration voltages and a current of 50 pA. The ELS-F130MH used in this study working at 130kV acceleration voltage can dramatically increase the accuracy of nanostructures compared with the EBL using in chapter 2. This insures the dolmen structures with higher quality, especially the corners of each nanorod.

Near field properties were also performed by PEEM. The details of the PEEM measurements were described in chapter 2. In this study, two light beams were used as excitation sources for PEEM. One beam was UV light from a mercury lamp (unpolarized cw light with a cutoff energy of 4.9 eV), which was used to characterize the morphologies of metallic nanoparticles. The other one was a Ti:sapphire femtosecond laser that delivers approximately 100 fs laser pulses with a tunable central wavelength (720–920 nm) at a repetition rate of 77 MHz. I used this laser for wavelength-dependent PEEM measurements to obtain the near-field photoemission

spectra, as well as for near-field mapping at various wavelengths. In this study, all the PEEM images were recorded under the field of view of $1.25 \mu\text{m}$ to ensure only single dolmen structure has been imaged. The laser power was kept as 120 mW before the PEEM window and the focal lens for the wavelength dependent measurements. The laser intensity on the sample was estimated to be $\sim 120 \text{ MW/cm}^2$, and considering a near-field intensity enhancement factor of $10^2 - 10^3$, the maximum local electric intensity could reach 12 - 120 GW/cm^2 , which is sufficient to generate multiphoton photoemission.

In this study, not only the near-field intensity spectra but also the spatially resolved photoemission intensity spectra were investigated which were obtained from integrating the photoemission intensity from selected area of one PEEM image and plotting against the excitation wavelengths. The spatially resolved photoemission intensity spectra of different selected areas can be used to separate the contribution to near-field enhancement for different plasmon modes existing in different areas of the structure.

Numerical simulation of the near-field properties of Au dolmen structures was performed using the FDTD Solutions software package (Lumerical, Inc.). The simulation details were almost same with that in chapter 2. The boundary conditions were different. In the light propagation direction, the same perfectly-matched layer boundary conditions were imposed. However only in plane perpendicular to the light propagation direction, the periodic boundary conditions were applied on each boundary. The simulation region in this plane is $1000 \text{ nm} \times 1000 \text{ nm}$, corresponding to one unit of the dolmen structure in the array.

Here, the near-field intensity spectrum was obtained from plotting the integral of the $(I/I_0)^4$ for a $320 \text{ nm} \times 320 \text{ nm}$ area on the interface between the dolmen structure and the substrate considering the nonlinearity of the PEEM measurement is 4. I and I_0 represent the local electromagnetic field intensity on the plane and the incident electromagnetic field intensity, respectively. This is for better comparison with the PEEM measurement results.

3.4 Results and discussion

3.4.1 Characterization of topography and far-field spectra

The complex coupled metallic nanostructures investigated in this study were Au dolmen structures as schematically shown in Figure 3.2 (a). As shown in the figure, the dolmen structure consists of a planar nanorod monomer and a planar nanorod dimer with small gap distance. The planar nanorod monomer had a dimension of $100 \times 150 \text{ nm}^2$. And the dimension of each nanorod in the planar nanorod dimer was $80 \times 140 \text{ nm}^2$. The edge-to-edge distance between two nanorods in the dimer part was 70 nm. The gap distance between the monomer part and dimer part was chosen to be 25 nm, and the small gap distance guaranteed a strong interaction between the monomer and dimer parts. The dolmen structures were arranged in 2D square in a $100 \times 100 \mu\text{m}^2$ area with the pitch size of $1 \mu\text{m}$. The large pitch size was fabricated to avoid the near-field interaction between the nearby dolmen structures.⁸ A SEM image was shown in Figure 3.2 (b), in which the Au dolmen structures are uniform and have good quality.

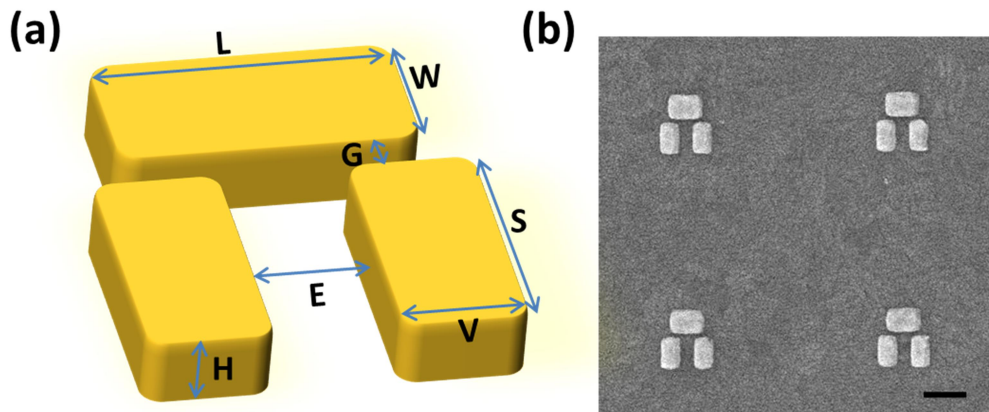


Figure 3.2 (a) Sketch map of Au dolmen structures. Design parameters of the structure are as follows: $L = 150 \text{ nm}$, $W = 100 \text{ nm}$, $G = 25 \text{ nm}$, $S = 140 \text{ nm}$, $V = 80 \text{ nm}$, $E = 70 \text{ nm}$, $H = 30 \text{ nm}$. (b) SEM image of the Au dolmen structures with the pitch size of $1 \mu\text{m}$. The scale bar is 200 nm.

Figure 3.3 shows the far-field extinction spectra of Au dolmen structures with horizontal polarized light irradiation (where the electric field vector is perpendicular to

the symmetry axis) and vertical polarized light irradiation (where the electric field vector is parallel to the symmetry axis of the dolmen structures) measured by FTIR. In the case of vertical polarization (red curve), a broad extinction band centered at approximately 810 nm can be observed. This is because under the vertical polarized light excitation, a broad dipole LSPR mode of the entire dolmen structure was excited. On the contrary, two distinct extinction peaks centered at approximately 760 nm and 850 nm can be observed under the horizontal polarization (black curve). These observations are consistent with previous reports on the far-field optical properties of Au dolmen structures.

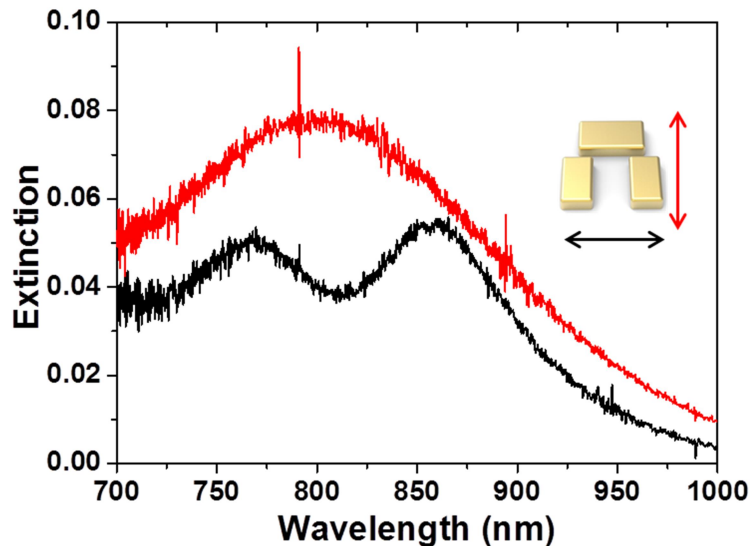


Figure 3.3 Far-field extinction spectra of Au dolmen structures measured by FTIR using different linearly polarized light. Red curve is under the vertical polarization (where the electric field vector is parallel to the symmetry axis), and black curve under the horizontal polarization (where the electric field vector is perpendicular to the symmetry axis). The polarization of incident light was also followed the arrow inset the figure.

In normal, only dipole plasmon mode in the two nanorods in dimer part can be excited, since the quadrupole-like mode (the quadrupole-like mode is for entire dimer part with anti-phase dipole distributions of the two nanorods) of the dimer is forbidden. However, the small gap between the monomer part and the dimer part ensure a strong near-field coupling between the two parts, result in the quadrupole mode in dimer part become possible. The sketch map of such discussion is shown in Figure 3.4.

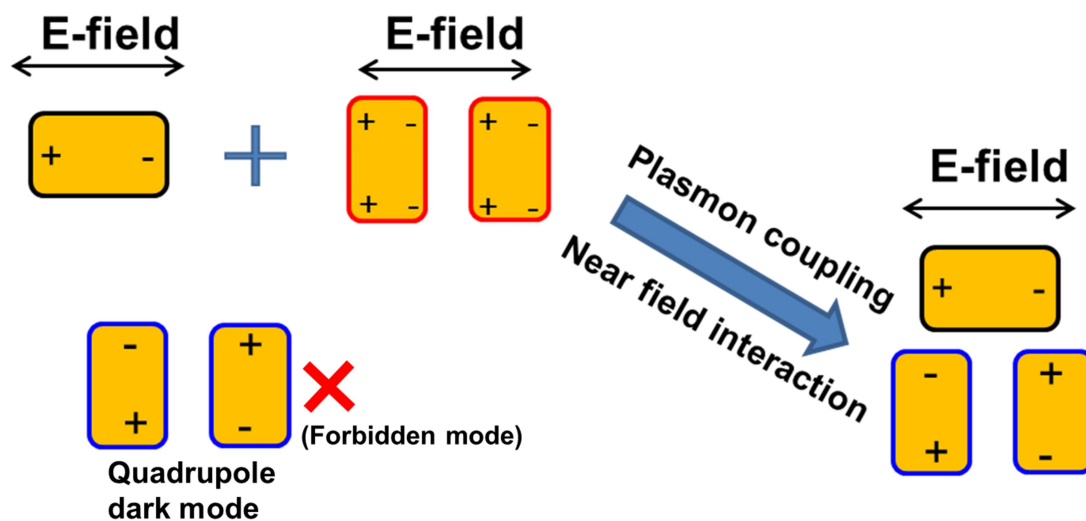


Figure 3.4 Sketch map of the formation of the quadrupole mode in dimer part. Under the horizontal polarization, only the dipole mode in monomer and dimer can be excited. The dark quadrupole mode is forbidden. However when the two part close to each other with small gap distance, the dipole mode in monomer may induce the quadrupole mode in dimer due to the near-field interaction.

In the frame of plasmonic Fano resonance theory, the dipole mode in monomer and quadrupole mode in dimer can interfere with each other, which leads to the so-called plasmonic Fano dip in the extinction spectrum.^{8, 10, 14} In Figure 3.3 a dip at 810 nm can be observed. The quadrupole mode is usually thought to be located close to this dip position. Such deduction has been demonstrated by calculations of the charge distribution.⁶ The quadrupole mode is subradiant dark plasmon mode, thus the radiant loss is smaller. It may exhibit a stronger local field enhancement in the near field and a longer dephasing time. Here, in Au dolmen structures, if the Fano resonances decide the far-field spectral profile, in near field, the maximum near-field enhancement should occur at the so-called Fano resonance wavelength (close to the dip wavelength). To confirm this, near field measurement is necessary.

3.4.2 Near-field spectra of Au dolmen structure

The near-field properties of Au dolmen structures were investigated using PEEM with a wavelength tunable femtosecond laser as the excitation source. As mentioned in chapter 2, in a metallic nanostructures system, assisted by LSPR femtosecond laser pulses provide substantial photoemission through nonlinear photoemission process mainly in multiphoton photoemission, especially when the wavelength of the laser pulses are at or close to the LSPR wavelength. The PEEM image under the femtosecond laser irradiation at resonance condition of a metallic nanostructure system can be regarded as the nonlinear near-field intensity mapping of the structures. Otherwise, the near-field photoemission intensity spectrum can be treated as the nonlinear near-field LSPR response spectrum of the plasmonic nanostructures.

Here, a wavelength-tunable femtosecond laser with the wavelength range from 720 nm to 920 nm was employed as the excitation source. The laser delivered a pulse with pulse duration of ~ 100 fs and a repetition rate of 77MHz. In this experiment, the laser pluses irradiated onto the sample under normal incidence. A nominal FOV of $1.25 \mu\text{m}$ for the PEEM measurements was used to ensure that only a single dolmen structure was imaged, since the pitch size of the structures was $1 \mu\text{m}$. To obtain the near-field spectra, I imaged the near-field photoemission intensity over the entire FOV for the illumination wavelengths range from 720 nm to 920 nm in 10 nm increments. The integrated the near-field photoemission intensity was integrated and plotted against the excitation wavelengths, thus the near-field spectra can be obtained.

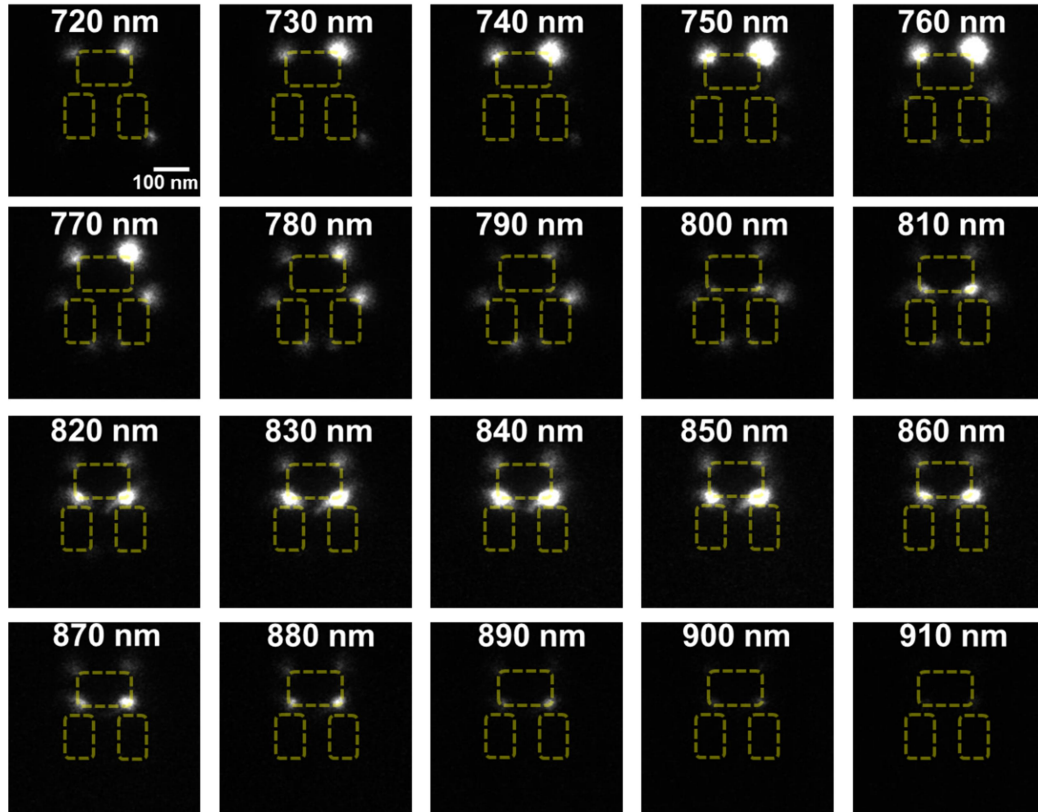


Figure 3.5 PEEM images of the dolmen structure under the horizontally polarized femtosecond laser irradiation with the central wavelength changing from 720 nm to 910 nm in the increments of 10 nm. Here, the FOV of $1.25\ \mu\text{m}$ is used which guaranteed only single structures can be detected. The yellow dashed line plots the geometry of dolmen structure.

Figure 3.5 shows the PEEM images of a single dolmen structure under the horizontally polarized excitation with the central wavelength changing from 720 nm to 910 nm (920 nm not shown here) in the increment of 10 nm. These images were the original framework of the near-field spectra. From these images, the hot spot intensities under different wavelength excitations are different can be clearly observed. By integrating the photoemission intensity of each image and plotted it against the wavelengths, near-field spectra of dolmen structure were obtained. Figure 3.6 shows the near-field spectra of Au dolmen structures under horizontal polarized laser light (red curve) and vertical polarized excitation laser light (black curve). The near-field spectra of dolmen structure under vertical polarization gives one broad band centered at approximately 820 nm; this is similar to the far-field extinction spectra. For horizontal

polarization excitation, it is found that two extinct peaks can be observed that located at approximately 760 nm and 850 nm, respectively. The near-field spectra and far-field extinction spectra were plotted together with the same wavelength range for easily compare with the far-field extinction spectra.

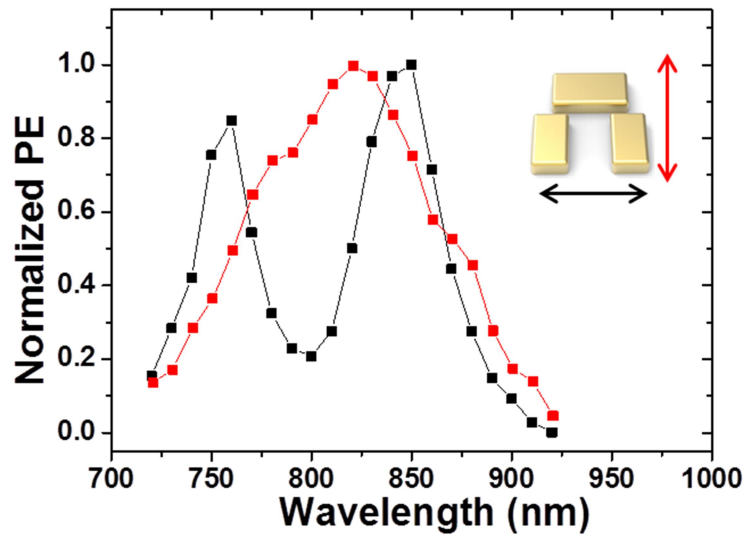


Figure 3.6 Near-field spectra of Au dolmen structure under horizontal polarization (black curve) and vertical polarization (red curve) using wavelength-tunable laser as the excitation source. The inset plots the polarization conditions.

Figure 3.7 shows the near-field spectra compared with far-field spectra under horizontal polarization (a) and vertical polarization (b). For vertical polarization, the broad plasmon peaks located at almost the same wavelength both in far- and near-field spectra. Furthermore, under horizontal polarization, the two near-field peaks also located at the same wavelengths with the two peaks in far-field extinction spectra. The results indicate that the maximum near-field enhancement was not located at the dip wavelength. It is unlike the results in a previous report Fano resonant plasmonic heptamer structures. Thus, it can be deduced that the far-field spectral profile maybe not caused by the Fano resonance since the quadrupole mode cannot be clearly observed at the dip wavelength in the near-field spectra.⁶ The interesting phenomena only occur under the horizontal polarization excitation, next I will just discuss about the investigation under this polarization.

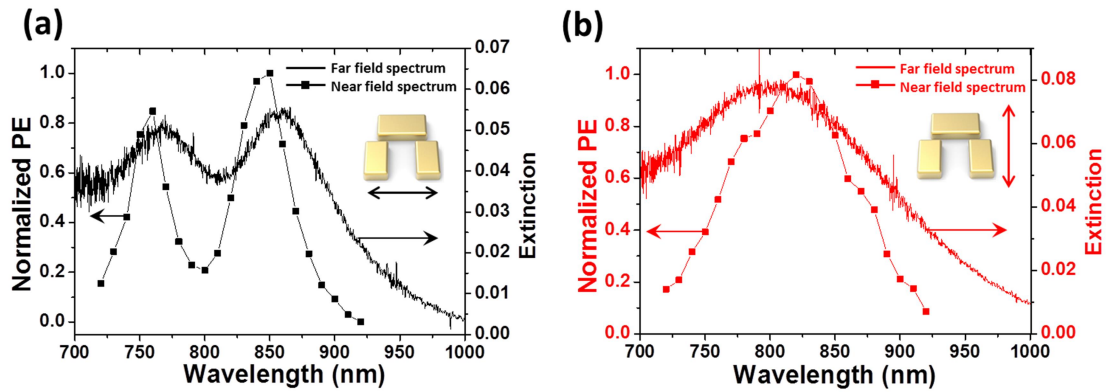


Figure 3.7 Near-field spectra compared with far-field spectra under horizontal polarization (a) and vertical polarization (b).

3.4.3 Near-field mapping of Au dolmen structure

In far- and near-field spectra of Au dolmen structure under horizontal polarization, the curves have approximately the same shape. To further understanding the mechanism in Au dolmen structures, the near-field intensity distributions at various wavelengths are a matter of particular interest. As mentioned above, since the photoemission intensity is correlated with the local electric field intensity in a nonlinear manner, the wavelength-dependent PEEM images can give the spatially resolved near-field intensity distribution. Firstly, by changing the excitation wavelength, it was found that, under different excitation conditions, the PEEM images gave different spatial distribution as can be seen in Figure 3.5. The near-field intensity distributions evolve dramatically, especially when the wavelength changes between the two peaks. However, it is difficult to distinguish where the hot spots excited from only in the PEEM image irradiated by fs laser. Therefore, an additional UV light source from a mercury lamp was employed. Figure 3.8 (a) shows the PEEM image of Au dolmen structure irradiated by UV light. Because the work function between Au and the substrate is different and the UV light is uniform with high photon energy (bigger than Au, smaller than substrate), the PEEM image irradiated by the UV light can provide details of the morphology of the Au nanostructures. Such kind of usage is an important reference for determining the

locations of plasmonic hot spots irradiated by fs laser. Figure 3.8 (b) shows the PEEM image of Au dolmen structure simultaneously irradiated with UV light and femtosecond laser pulses with central wavelength of 800nm. This simultaneous irradiation helps to outline Au dolmen structures, which are shown as red dashed lines in Figure 3.9.

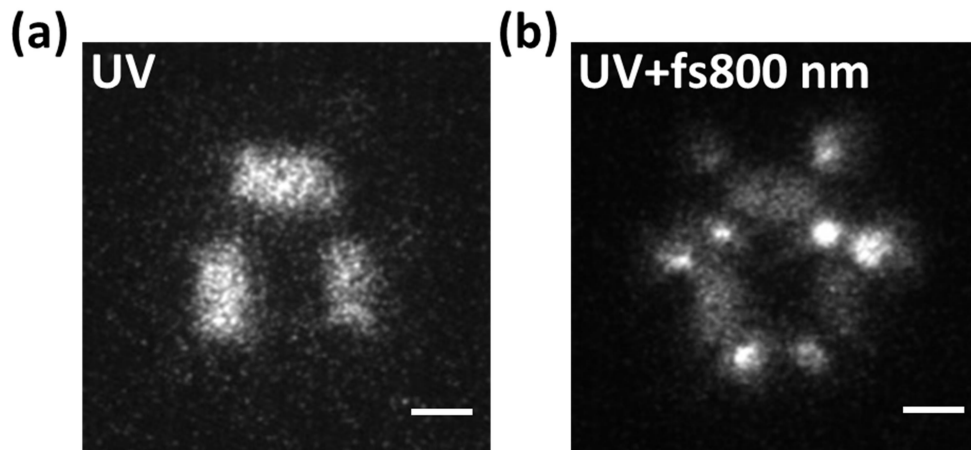


Figure 3.8 PEEM image of Au dolmen structure under UV light irradiation (a) and simultaneously irradiated with UV light and femtosecond laser pulses, with a central wavelength of 800 nm. The scale bar is 100 nm.

To present the evolution of the near-field intensity distribution more clearly, the PEEM images for four characterized wavelengths were shown in Figure 3.9. The four characterized wavelengths are also remarked in the inset number in Figure 3.9 (a). At the two peak wavelengths (760 nm (1) and 850 nm (4)), the photoemission is mainly from the top monomer part and dominate the near-field enhancement. At the shorter-wavelength peak of 760 nm, the photoemission stronger located at the two upper corners. However, at the longer-wavelength peak of 850 nm, two lower corners are stronger. And at the dip wavelength of 800 nm (3), four hot spots from the dimer part also can be seen. They located at the two nearest lower corners and two outside upper corners. However, due to the near-field spectrum, the near-field enhancement here is much weaker than the two peaks. The strongest photoemission in dimer part was found to be at the wavelength of 780 nm (2), however, it is still very weak.

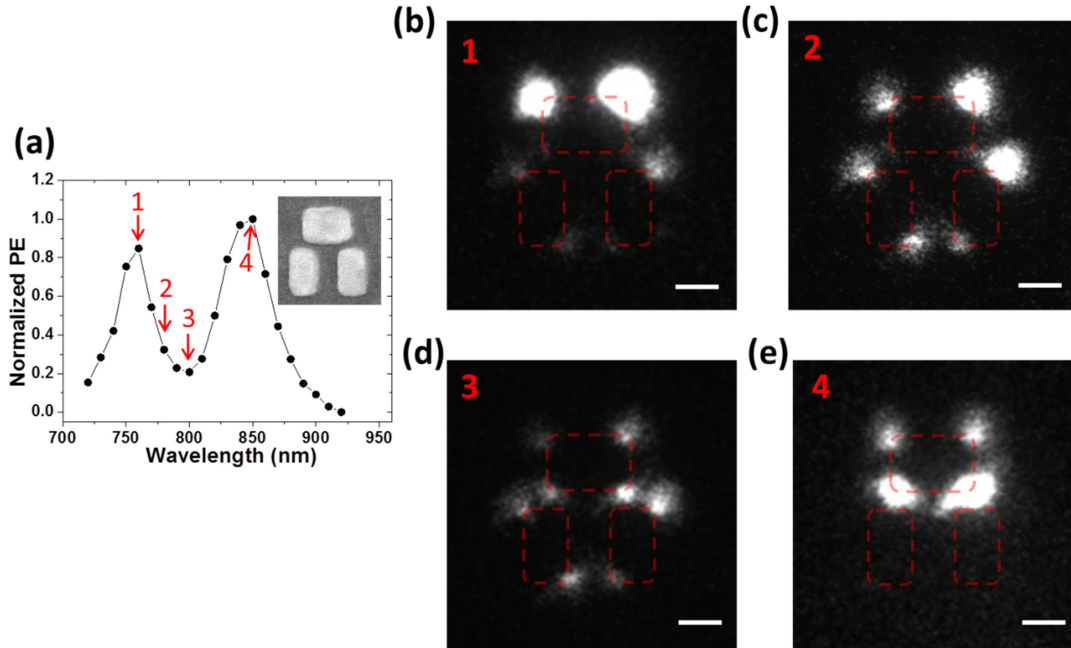


Figure 3.9 (a) Near-field spectra of Au solemn structure. The inset shows an SEM image of Au dolmen structure investigated here. (b-e) PEEM images under fs laser excitation with four different wavelengths. The four wavelengths include the two peak wavelengths (shorter-peak wavelength of 760nm and longer-peak wavelength of 850 nm), dip wavelength of 800 nm and 780 nm with the maximum enhancement from the dimer part. The four wavelengths are also remarked in inset of (a). The red dashed line plots the geometry of the dolmen structure. The scale bar in all images is 100 nm.

The PEEM images for four characterized wavelengths excitation indicate that there are different plasmon modes excited by the different wavelengths. To further explain the experimental observation and confirm the plasmon modes, numerical calculations were performed.

3.4.4 Finite-difference time-domain simulation results

The far-field extinction spectra, the near-field intensity enhancement spectra, the near-field intensity distributions, and charge distributions are performed by FDTD simulations. The simulated far-field extinction spectrum (red) and near-field intensity spectrum (black) under horizontal polarization excitation are shown in Figure 3.10. In the figure, the normalized integrated value $(I/I_0)^4$ over an area of $320 \text{ nm} \times 320 \text{ nm}$ at

the interface between the dolmen structure and the substrate in the near-field spectrum is shown for better comparison with the PEEM measurement results. Since it has mentioned above, it was assumed an average four-photon photoemission process for the PEEM measurement. Here, I and I_0 represent the local electromagnetic field intensity on the plane and the incident electromagnetic field intensity, respectively. In the near field, the maximum near-field intensity was not induced at the extinction dip wavelength, instead, two peaks also can be observed and they almost coincided with the far-field extinction spectrum. The simulation results reproduce well with the experimental results.

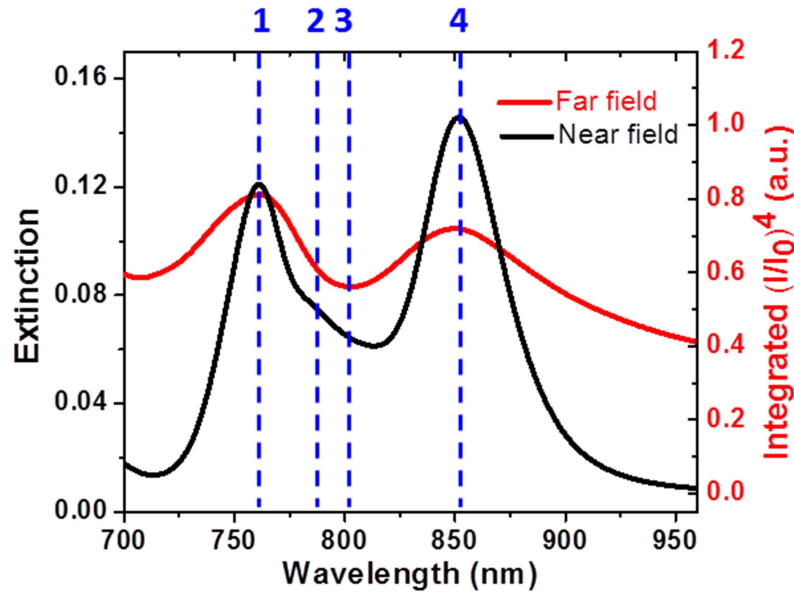


Figure 3.10 FDTD simulated far-field extinction spectrum (red) and near-field intensity spectrum (black) under horizontal polarization excitation, plotting the integral of the $(I/I_0)^4$ for a $320 \text{ nm} \times 320 \text{ nm}$ area on the interface between the dolmen structure and the substrate.

The near-field electric field intensity distributions of Au dolmen structure under the corresponding four characteristic wavelengths were shown in Figure 3.11. The redistribution of the near-field enhancement in monomer part under the two peak wavelengths excitation is clearly observed with the same distribution compared with the experimental results. The near-field intensity distribution on the dimer part at

wavelength positions of 2 and 3 is also reproduced well with the experimental observations.

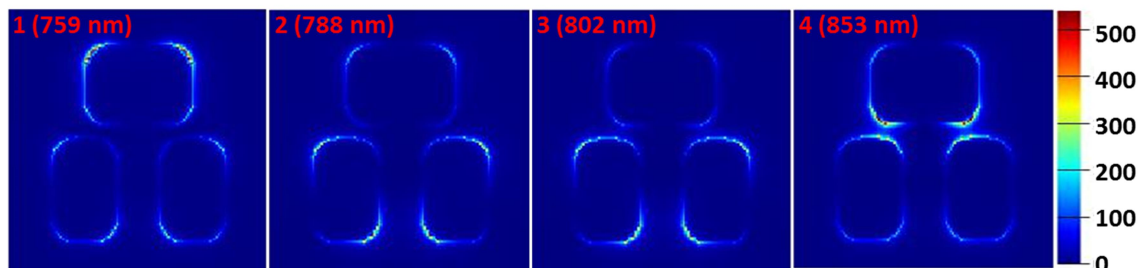


Figure 3.11 Calculated near-field electric field intensity distributions under the corresponding four characteristic wavelengths. The wavelengths of 1, 2, 3, 4 are also remarked in Figure 3.10.

Figure 3.12 performs the calculated charge distribution at the two peak wavelengths by FDTD simulation. The results indicate that two kinds of plasmon modes were generated correspond to the shorter-wavelength peak and longer-wavelength peak. In shorter-wavelength peak, the charge distribution shows an anti-bonding mode between the monomer and dimer parts. While in longer-wavelength peak, the charge distribution shows a bonding mode between the monomer and dimer parts. The anti-bonding mode and bonding mode are thought to result from the plasmon hybridization.

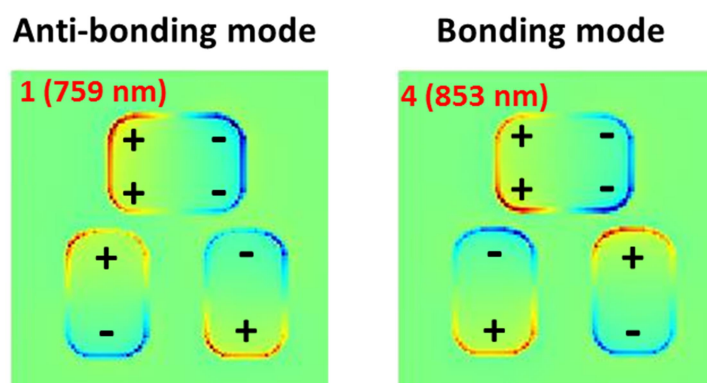


Figure 3.12 Calculated charge distribution at the two peak wavelengths. The wavelength correspond to the number marks in Figure 3.10.

It is reasonable to interpret the wavelength-dependent near-field patterns results in the frame of the plasmon hybridization model. The two plasmon hybridization states were generated from the strong near-field coupling between the dipole mode in the monomer

and the quadrupole-like mode in the dimer.^{1, 8} The shorter-wavelength peak (higher-energy) is according to the anti-bonding state. On the other hand, the longer-wavelength peak (lower-energy) is according to the bonding state. The calculated charge distribution results shown in Figure 3.12 support such assumption. In the case of anti-bonding hybridized mode, the charge distribution in the monomer and dimer parts leads to a repulsive Coulomb force at the gap area. It makes the charges in the monomer easier concentrate at the two upper corners. Otherwise, in the case of bonding hybridized mode, the charge distribution in the monomer and dimer parts leads to an attractive Coulomb force at the gap area. Thus, the charges in the monomer easier concentrated at the lower corners of the monomer. This explains the experimental and simulated near-field intensity distribution results under anti-bonding and bonding excitations, respectively.

3.4.5 Spatially resolved photoemission intensity spectra

The spatially resolved photoemission intensity spectra from different regions of the structure can be obtained due to the high spatial resolution of PEEM measurements. The spatially resolved photoemission intensity spectrum is done by integrating the photoemission signal of a selected region and plotting it against the excitation wavelengths. Figure 3.13 (a) shows the experimental spatially resolved photoemission intensity spectra for four regions, and the regions were described in Figure 3.13 (b). The total photoemission intensity curve can be divided into three bands. The three bands dominate the photoemission signal in three different regions. Area 1 corresponds to the anti-bonding plasmon peaks and area 2 corresponds to the bonding plasmon peak. In area 3, a small peak located at 780 nm can be observed. This peak related to the quadrupole-like plasmon mode in dimer part. This quadrupole-like mode was thought to lead the formation of the Fano resonance through the interference with the dipole mode in monomer. However, this quadrupole-like mode is much weaker than the two plasmon

hybridized plasmon modes.

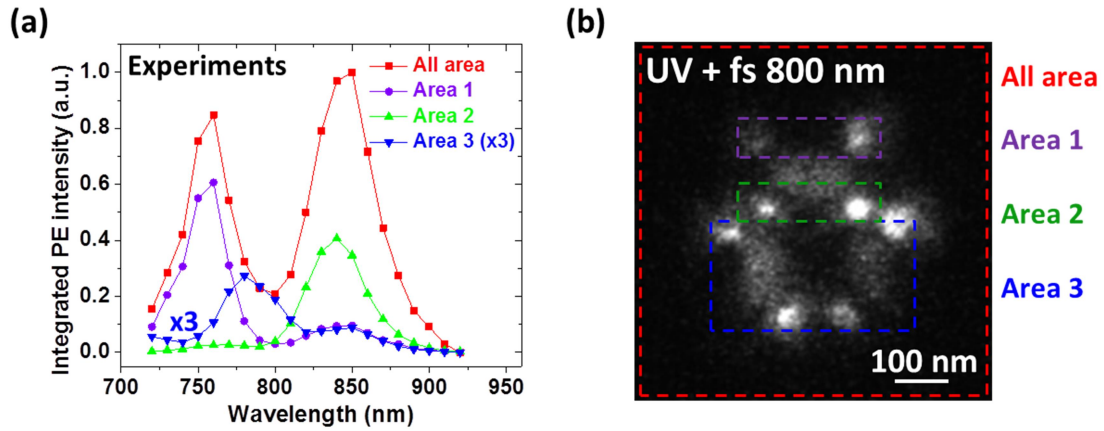


Figure 3.13 (a) The experimental spatially resolved photoemission spectrum of the dolmen, obtained for four different regions by integrating the photoemission signal from the selected areas. (b) The sketch map of the four selected areas.

Figure 3.14 shows the simulated spatially resolved photoemission spectrum of the dolmen structures for four selected regions. The results reproduce well with the experimental observation. A weak peak can also be identified in area 3 corresponding to the quadrupole-like mode in dimer part.

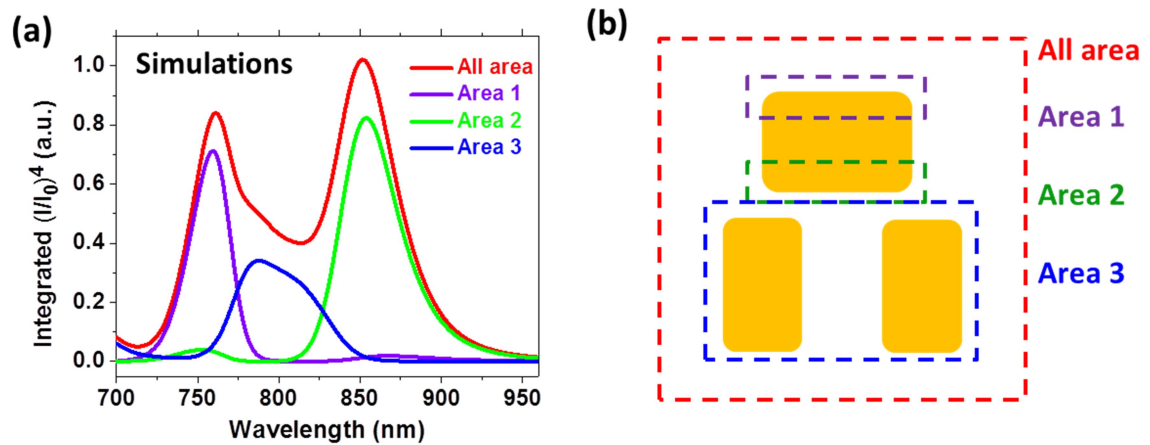


Figure 3.14 (a) The simulated spatially resolved photoemission spectrum of the dolmen, obtained for four different regions by integrating the photoemission signal from the selected areas. (b) The sketch map of the four selected areas.

From both the experimental and simulation results of spatially resolved photoemission intensity spectra, it is reasonable to conclude that in complex coupled dolmen structures, the near-field enhancement is dominated by plasmon hybridization

rather than Fano resonance.

3.4.6 Discussions

Upon the results above, some new topics can be summarized which may help to better understand the mechanism of plasmon hybridization and Fano resonance. As mentioned in the introductions, the plasmon hybridization and Fano resonance are mixed in most coupled plasmonic nanostructures. It is very hard to distinguish only from the far-field extinction or scattering spectra. The crossover between the EIT phenomena and Rabi splitting in a plasmon-molecular-coupled system exist the similar problem.³⁹ However, such crossover can be distinguished through the excitation spectra that reflect molecular absorption spectra. As deduced from the above part, the near-field spectral properties can be applied to distinguish the difference of the near-field enhancement contribution between plasmon hybridization and Fano resonance.

Halas et al. investigated the near-field properties of plasmonic heptamer structures which support the Fano resonance using surface-enhanced Raman scattering (SERS) and numerical calculations.⁶ In a plasmonic heptamer, plasmon hybridization and Fano resonance both exist. The dipole LSPRs of the central nanodisks and the outer nanodisks are hybridized to a bonding bright mode with same phase in all nanodisks and an anti-bonding dark mode with the center nanodisks and outer nanodisks out of phase. The bonding mode and anti-bonding mode interference and induce the Fano resonance.^{40, 41} In experiments, they observed strongest SERS signals when the wavelength of the pump laser and the Raman Stokes mode of interest overlap the Fano dip wavelength. Additionally, their calculations performed that the wavelength of the Fano dip in the far-field scattering spectrum is very close to the wavelength of the maximum in the near-field enhancement spectrum. In a real Fano resonance system, the sharp dark mode around the extinction or scattering dip position should dominate the near-field enhancement. Such kind of finding was also demonstrated by Frimmer et al.

using the CL technique.²⁶

From PEEM measurements, it did not observed strong near-field enhancement at the dip position or the Fano resonance position in dolmen system. A strong anti-bonding mode and a strong bonding mode can be observed, and they dominate the near-field enhancement. In previous investigation, the Fano resonance was thought to result the far-field spectral profile in dolmen structures. However, due to the study above, it is reasonable to conclude that plasmon hybridization dominate the near-field enhancement and result in the far-field line-shape in dolmen structures.

3.5 Conclusions

In this chapter, the near-field properties of a complex coupled Au dolmen structures have been experimentally investigated using PEEM. The spatial evolution of the near-field patterns revealed the near-field plasmon coupling occurring in the coupled dolmen system. The evolution of near-field mapping with high spatial resolution under different wavelength excitation presented the coupling anti-bonding and bonding plasmon modes which hybridized from the interaction between a dipole plasmon mode in the monomer part and a quadrupole-like mode in the dimer part. It is found that the two hybridized plasmon mode dominated the near-field enhancement. Although the quadrupole-like mode in the dimer part can be identified by the spatially resolved near-field spectra, it only contributed weakly to the near-field enhancement. Furthermore, a new method which can be used to distinguish the plasmon hybridization and Fano resonance was proposed. That is the near-field spectral properties allows for distinguishing the difference of the contribution to the near-field enhancement on plasmon hybridization and Fano resonance. The results deepen our understanding of plasmon hybridization and Fano resonance and are expected to promote further development of potential applications.

3.6 References

1. Prodan, E.; Radloff, C.; Halas, N. J.; Nordlander, P., A Hybridization Model for the Plasmon Response of Complex Nanostructures. *Science* **2003**, 302, 419-422.
2. Sonnefraud, Y.; Koh, A. L.; McComb, D. W.; Maier, S. A., Nanoplasmonics: Engineering and Observation of Localized Plasmon Modes. *Laser & Photonics Reviews* **2012**, 6, 277-295.
3. Luk'yanchuk, B.; Zheludev, N. I.; Maier, S. A.; Halas, N. J.; Nordlander, P.; Giessen, H.; Chong, C. T., The Fano resonance in plasmonic nanostructures and metamaterials. *Nature Materials* **2010**, 9, 707-715.
4. Fan, J. A.; Wu, C. H.; Bao, K.; Bao, J. M.; Bardhan, R.; Halas, N. J.; Manoharan, V. N.; Nordlander, P.; Shvets, G.; Capasso, F., Self-Assembled Plasmonic Nanoparticle Clusters. *Science* **2010**, 328, 1135-1138.
5. Bao, Y. J.; Hu, Z. J.; Li, Z. W.; Zhu, X.; Fang, Z. Y., Magnetic Plasmonic Fano Resonance at Optical Frequency. *Small* **2015**, 11, 2177-2181.
6. Ye, J.; Wen, F. F.; Sobhani, H.; Lassiter, J. B.; Van Dorpe, P.; Nordlander, P.; Halas, N. J., Plasmonic Nanoclusters: Near Field Properties of the Fano Resonance Interrogated with SERS. *Nano Letters* **2012**, 12, 1660-1667.
7. Alonso-Gonzalez, P.; Schnell, M.; Sarriugarte, P.; Sobhani, H.; Wu, C. H.; Arju, N.; Khanikaev, A.; Golmar, F.; Albella, P.; Arzubiaga, L.; Casanova, F.; Hueso, L. E.; Nordlander, P.; Shvets, G.; Hillenbrand, R., Real-Space Mapping of Fano Interference in Plasmonic Metamolecules. *Nano Letters* **2011**, 11, 3922-3926.
8. Yan, C.; Martin, O. J. F., Periodicity-Induced Symmetry Breaking in a Fano Lattice: Hybridization and Tight-Binding Regimes. *ACS Nano* **2014**, 8, 11860-11868.
9. Fang, Z. Y.; Cai, J. Y.; Yan, Z. B.; Nordlander, P.; Halas, N. J.; Zhu, X., Removing a Wedge from a Metallic Nanodisk Reveals a Fano Resonance. *Nano Letters* **2011**, 11, 4475-4479.
10. Coenen, T.; Schoen, D. T.; Mann, S. A.; Rodriguez, S. R. K.; Brenny, B. J. M.; Polman, A.; Brongersma, M. L., Nanoscale Spatial Coherent Control over the Modal Excitation of a Coupled Plasmonic Resonator System. *Nano Letters* **2015**, 15, 7666-7670.

11. Rahmani, M.; Luk'yanchuk, B.; Hong, M. H., Fano Resonance in Novel Plasmonic Nanostructures. *Laser & Photonics Reviews* **2013**, *7*, 329-349.
12. Mirin, N. A.; Bao, K.; Nordlander, P., Fano Resonances in Plasmonic Nanoparticle Aggregates. *Journal of Physical Chemistry A* **2009**, *113*, 4028-4034.
13. Gallinet, B.; Martin, O. J. F., Influence of Electromagnetic Interactions on the Line Shape of Plasmonic Fano Resonances. *ACS Nano* **2011**, *5*, 8999-9008.
14. Verellen, N.; Sonnefraud, Y.; Sobhani, H.; Hao, F.; Moshchalkov, V. V.; Van Dorpe, P.; Nordlander, P.; Maier, S. A., Fano Resonances in Individual Coherent Plasmonic Nanocavities. *Nano Letters* **2009**, *9*, 1663-1667.
15. Metzger, B.; Schumacher, T.; Hentschel, M.; Lippitz, M.; Giessen, H., Third Harmonic Mechanism in Complex Plasmonic Fano Structures. *ACS Photonics* **2014**, *1*, 471-476.
16. Chen, H. Y.; He, C. L.; Wang, C. Y.; Lin, M. H.; Mitsui, D.; Eguchi, M.; Teranishi, T.; Gwo, S., Far-Field Optical Imaging of a Linear Array of Coupled Gold Nanocubes: Direct Visualization of Dark Plasmon Propagating Modes. *ACS Nano* **2011**, *5*, 8223-8229.
17. Solis, D.; Willingham, B.; Nauert, S. L.; Slaughter, L. S.; Olson, J.; Swanglap, P.; Paul, A.; Chang, W. S.; Link, S., Electromagnetic Energy Transport in Nanoparticle Chains via Dark Plasmon Modes. *Nano Letters* **2012**, *12*, 1349-1353.
18. Liu, N.; Langguth, L.; Weiss, T.; Kastel, J.; Fleischhauer, M.; Pfau, T.; Giessen, H., Plasmonic Analogue of Electromagnetically Induced Transparency at the Drude Damping Limit. *Nature Materials* **2009**, *8*, 758-762.
19. Ueno, K.; Juodkazis, S.; Shibuya, T.; Yokota, Y.; Mizeikis, V.; Sasaki, K.; Misawa, H., Nanoparticle Plasmon-Assisted Two-Photon Polymerization Induced by Incoherent Excitation Source. *Journal of the American Chemical Society* **2008**, *130*, 6928-6929.
20. Gao, S. Y.; Ueno, K.; Misawa, H., Plasmonic Antenna Effects on Photochemical Reactions. *Accounts of Chemical Research* **2011**, *44*, 251-260.
21. Brongersma, M. L.; Halas, N. J.; Nordlander, P., Plasmon-Induced Hot Carrier Science and Technology. *Nature Nanotechnology* **2015**, *10*, 25-34.
22. Kauranen, M.; Zayats, A. V., Nonlinear Plasmonics. *Nature Photonics* **2012**, *6*, 737-748.

23. Schumacher, T.; Kratzer, K.; Molnar, D.; Hentschel, M.; Giessen, H.; Lippitz, M., Nanoantenna-Enhanced Ultrafast Nonlinear Spectroscopy of a Single Gold Nanoparticle. *Nature Communications* **2011**, 2, 333.
24. Aouani, H.; Rahmani, M.; Navarro-Cia, M.; Maier, S. A., Third-Harmonic-Upconversion Enhancement From a Single Semiconductor Nanoparticle Coupled to a Plasmonic Antenna. *Nature Nanotechnology* **2014**, 9, 290-294.
25. Celebrano, M.; Wu, X. F.; Baselli, M.; Grossmann, S.; Biagioni, P.; Locatelli, A.; De Angelis, C.; Cerullo, G.; Osellame, R.; Hecht, B.; Duo, L.; Ciccacci, F.; Finazzi, M., Mode Matching in Multiresonant Plasmonic Nanoantennas for Enhanced Second Harmonic Generation. *Nature Nanotechnology* **2015**, 10, 412-417.
26. Frimmer, M.; Coenen, T.; Koenderink, A. F., Signature of a Fano Resonance in a Plasmonic Metamolecule's Local Density of Optical States. *Physical Review Letters* **2012**, 108, 077404.
27. Lassiter, J. B.; Sobhani, H.; Knight, M. W.; Mielczarek, W. S.; Nordlander, P.; Halas, N. J., Designing and Deconstructing the Fano Lineshape in Plasmonic Nanoclusters. *Nano Letters* **2012**, 12, 1058-1062.
28. Kubo, A.; Onda, K.; Petek, H.; Sun, Z. J.; Jung, Y. S.; Kim, H. K., Femtosecond Imaging of Surface Plasmon Dynamics in a Nanostructured Silver Film. *Nano Letters* **2005**, 5, 1123-1127.
29. Schertz, F.; Schmelzeisen, M.; Mohammadi, R.; Kreiter, M.; Elmers, H. J.; Schonhense, G., Near Field of Strongly Coupled Plasmons: Uncovering Dark Modes. *Nano Letters* **2012**, 12, 1885-1890.
30. Douillard, L.; Charra, F., Photoemission Electron Microscopy, a Tool for Plasmonics. *Journal of Electron Spectroscopy and Related Phenomena* **2013**, 189, 24-29.
31. Melchior, P.; Kilbane, D.; Vesseur, E. J.; Polman, A.; Aeschlimann, M., Photoelectron Imaging of Modal Interference in Plasmonic Whispering Gallery Cavities. *Optics Express* **2015**, 23, 31619-31626.
32. Word, R. C.; Konenkamp, R., Mode Structure of Planar Optical Antennas on Dielectric Substrates. *Optics Express* **2016**, 24, 18727-18738.
33. Ji, B. Y.; Qin, J.; Tao, H. Y.; Hao, Z. Q.; Lin, J. Q., Subwavelength Imaging and

Control of Ultrafast Optical Near-Field under Resonant- and Off-Resonant Excitation of Bowtie Nanostructures. *New Journal of Physics* **2016**, 18, 093045.

34. Sun, Q.; Ueno, K.; Yu, H.; Kubo, A.; Matsuo, Y.; Misawa, H., Direct Imaging of the Near Field and Dynamics of Surface Plasmon Resonance on Gold Nanostructures Using Photoemission Electron Microscopy. *Light-Science & Applications* **2013**, 2, e118.

35. Sun, Q.; Yu, H.; Ueno, K.; Sun, Q.; Yu, H.; Ueno, K.; Kubo, A.; Matsuo, Y.; Misawa, H., Dissecting the Few-Femtosecond Dephasing Time of Dipole and Quadrupole Modes in Gold Nanoparticles Using Polarized Photoemission Electron Microscopy. *ACS Nano* 2016, 10, 3835-3842.

36. Han Yu, Q. S., Kosei Ueno, Tomoya Oshikiri, Atsushi Kubo, Yasutaka Matsuo, Hiroaki Misawa, Exploring Coupled Plasmonic Nanostructures in the Near Field by Photoemission Electron Microscopy. *ACS Nano* 2016, 10, 10373-10381.

37. Gallinet, B.; Martin, O. J. F., Relation Between Near-Field and Far-Field Properties of Plasmonic Fano Resonances. *Optics Express* **2011**, 19, 22167-22175.

38. Grigoriev, V.; Varault, S.; Boudarham, G.; Stout, B.; Wenger, J.; Bonod, N., Singular Analysis of Fano Resonances in Plasmonic Nanostructures. *Physical Review A* **2013**, 88, 063805.

39. Murata, N.; Hata, R.; Ishihara, H., Crossover between Energy Transparency Resonance and Rabi Splitting in Antenna-Molecule Coupled Systems. *Journal Of Physical Chemistry C* **2015**, 119, 25493-25498.

40. Lassiter, J. B.; Sobhani, H.; Fan, J. A.; Kundu, J.; Capasso, F.; Nordlander, P.; Halas, N. J., Fano Resonances in Plasmonic Nanoclusters: Geometrical and Chemical Tunability. *Nano Letters* **2010**, 10, 3184-3189.

41. Hentschel, M.; Saliba, M.; Vogelgesang, R.; Giessen, H.; Alivisatos, A. P.; Liu, N., Transition from Isolated to Collective Modes in Plasmonic Oligomers. *Nano Letters* **2010**, 10, 2721-2726.

Chapter 4

Far-field coupling and the grating effect in coupled plasmonic nanostructures

4.1 Abstract

The pitch size of a regular two-dimensional array of metallic nanoparticles plays an important role in the plasmonic properties of the array due to the plasmon coupling between nanoparticles. In particular, when the pitch size is comparable to the plasmon resonant wavelength, the grating effect can alter the resonant wavelength and the dephasing of the plasmon resonance. In this study, far-field coupling and grating effect on complex Au dolmen structures which exhibit multiple plasmon modes due to plasmon hybridization have been experimentally investigated from both the far field and the near field. The near-field properties were investigated by photoemission electron microscopy using wavelength-tunable femtosecond laser as the excitation source. The results demonstrated that the two hybridized plasmon modes on Au dolmen structures could be modified by the grating effect. For comparison, the grating effects in arrays of simple Au nanoblock structures and complex heptamer structures which support a strong bright plasmon mode and a dark plasmon mode, respectively, have also been investigated. The spectral response of the two hybridized plasmon modes on the dolmen structures as the pitch size changed evolved in a manner similar to that of the bright dipole mode on the nanoblock structures can be observed, whereas the dark mode on the heptamer structures is less sensitive to the pitch size. These results deepen our understanding of the grating effect for complex coupled plasmonic nanostructures.

4.2 Introduction

For metallic NPs in regular 2D array, the optical properties can be different from those of individual NPs. The optical properties can be influenced by the pitch size. In a metallic NP array, two types of the interaction between nearby NPs can be distinguished. They are the near-field interaction due to the short range interaction and the far-field interaction due to the long range interaction. The two kinds of interactions can be switched by the pitch size in the metallic NP array or the inter-particles distance for a single NP array, d . When d is much smaller than the NP size, the interaction between adjacent NPs based on the short range of the electromagnetic field within several tens of nanometers leads to the near-field coupling with d^{-3} dependence dominates. When d is larger enough comparable to the NP size and the LSPR wavelengths, the interaction of long range dipole-dipole interaction in the scattered light field leads to the far-field coupling with d^{-1} dominates. Thus, the near-field interaction and far-field interaction can be separated by changing the pitch size of the 2D NP array. The far- and near-field coupling have been investigated intensively on metallic NPs array which formed by simple nanostructures, such as nanoblocks, nanodisks, and nanorods.¹⁻¹⁶

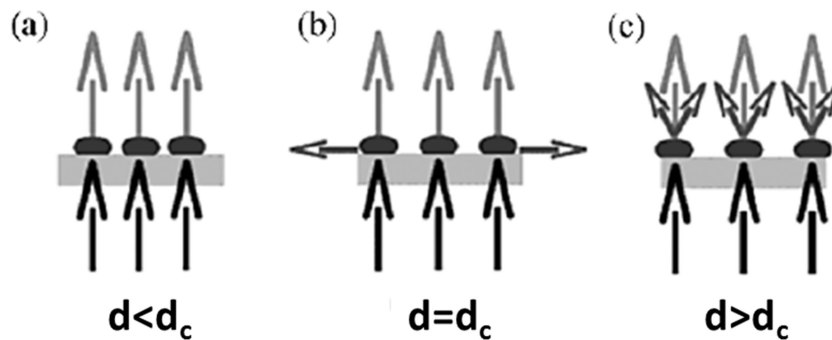


Figure 4.1 The diffraction of grating order change from evanescent (a) to radiative (c) upon the changing of d from $d < d_c$ to $d > d_c$.

The grating effect in the far-field coupling regime plays an important role in determining the plasmonic properties. It indicates that the diffraction order can be changed from the evanescent to radiation by changing the pitch size.^{12, 13} For 2D square

grating of metallic NPs, there is a critical pitch size, d_c , it decided a new diffractive radiation order emerges for a given wavelength, λ . For normal incidence onto NP array on a substrate, there are two values of d_c for first-order diffraction. One is $d_c = \lambda/n$ which correspond to radiation onto the substrate. Another one is $d_c = \lambda$ which correspond to radiation on to the free space. When $d < d_c$, the diffraction of grating order is evanescent. The plasmon resonance of an individual particle decided the optical response of the grating at this situation with reduced radiation damping compared to a single particle as shown in Figure 4.1 (a). When d is approach to d_c (and $d = d_c$), the light fields related to a grating order is still evanescent, however, the first grating order begins to radiate in the array plane and an almost in-phase addition of the scattered light fields of neighboring particles enhanced the local optical fields in the plane of the array as shown in Figure 4.1 (b). This lead to a modification of the plasmon resonance properties resulted in the red shift of the plasmon resonant wavelength. When $d > d_c$, the diffraction of grating order becomes radiative at a grazing angle as shown in Figure 4.1 (c). The total power radiated by the array can be increased by the additional radiating grating order; it enhanced the radiation damping and slight blue shift of the individual particle plasmon resonance. Otherwise, it can strongly modify the plasmon resonance and the damping. When the diffraction order is evanescent, the diffraction light propagated along the plane of the array. At this situation, the local optical fields in the plane become large since from an almost in-phase addition of the scattered light field of the nearby structures. Lamprecht et al. have investigated the far-field coupling and grating effect on Au nanodisks arranged in 2D patterns with different pitch sizes.¹² They found that the plasmon resonant wavelength evolves with the pitch size as shown in the dashed line of Figure 4.2. The plasmon peaks red shift first as increasing the pitch size. Then it blue shifts as increasing the pitch size after the pitch size bigger than the grating constant of the first grating order diffracted into substrate. After that slightly red shifts again as increasing the pitch size. At last, it slightly blue shifts after the pitch size bigger than the grating constant of the first grating order diffracted into free space. Furthermore, a

dramatic increase of the plasmon damping have been also observed when the pitch size close to the transition region from evanescent to radiative fields of the first grating order on the substrate and free space.¹² The results experimentally demonstrated that the pitch size of the 2D metallic nanoparticles array could dramatically influence the plasmon resonance as well as the plasmon damping.

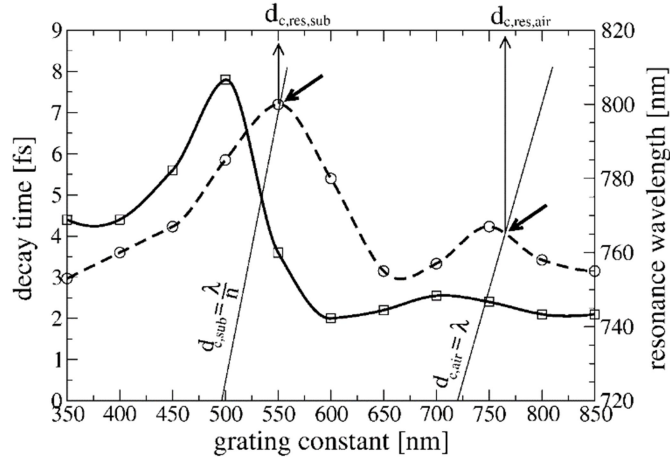


Figure 4.2 Experimental results of plasmon resonant wavelength and decay time plotted against the corresponding grating constant (pitch size).¹²

Otherwise, since the far field and near field are influenced by each other, such grating effect should also alter the near-field plasmon properties.¹² The near- and far-field plasmon coupling becomes more complex when complex NP aggregates are arranged in regular arrays, because the near-field coupling in complex NP already plays an important role in the plasmonic properties. The investigations of far- and near-field coupling on plasmonic nanostructures were mainly through far-field spectroscopic measurements. Near-field properties of such plasmon coupling may provide new insights into plasmon coupling in complex metallic NP arrays.

In this chapter, the far-field coupling especially the grating effect on Au nanostructures arrays with complex coupled nanostructures have been investigated through near-field measurement using PEEM. Au dolmen structures with different pitch sizes have been firstly investigated. The results demonstrated that the two hybridized plasmon modes can be influenced by the grating effect. The spectral shifts of the

anti-bonding plasmon mode and bonding plasmon mode as varying the pitch sizes can be clearly observed in experimentally. Furthermore, the anti-bonding mode was dramatically suppressed when the pitch size was similar to the grating constant. To better understanding the regime, simple nanoblock structures and complex heptamer structures have also been investigated, in which supports a superradiant plasmon mode and a subradiant plasmon mode, respectively. The spectral response of the two hybridized plasmon modes on the dolmen structures as the pitch size changed evolved in a manner similar to that of the bright dipole mode on the nanoblock structures can be observed, whereas the dark mode on the heptamer structures is less sensitive to the pitch size. These results deepen our understanding of the grating effect for complex coupled plasmonic nanostructures.

4.3 Experimental details

The Au nanostructures investigated in this chapter were also fabricated by EBL (ELS-F130MH, Elionix). The fabrication process is same as described in chapter 3. Near field properties were also performed by PEEM. The details of the PEEM measurements were same as described in chapter 3. Numerical simulation of the near-field properties of Au dolmen structures was performed using the FDTD Solutions software package (Lumerical, Inc.). The details were same as described in chapter 3. Here, two light source angels were used in this study. One is the normal incidence, another one is the oblique incidence with the angel of 24° . Under normal incidence excitation, the boundary conditions were same as that in chapter 3. However, the BEFAST boundary condition was used under the oblique incidence which can largely decrease the simulation time. Several simulation regions were used which also corresponded to the different pitch sizes of nanostructures investigated in this study.

4.4 Results and discussion

4.4.1 Far-field coupling and grating effect in nanoblock structures

The far-field coupling and grating effect on Au nanoblock structures have been investigated on the basis of the far-field spectroscopy and numerical simulations. Since the far field and near field are influenced by each other, such grating effect should also alter the near-field plasmon properties.¹² However, there is no experimental investigation of such plasmonic nanostructures in near field. In this study, I firstly investigated the far-field coupling and grating effect on Au nanoblock structures in near field by PEEM.

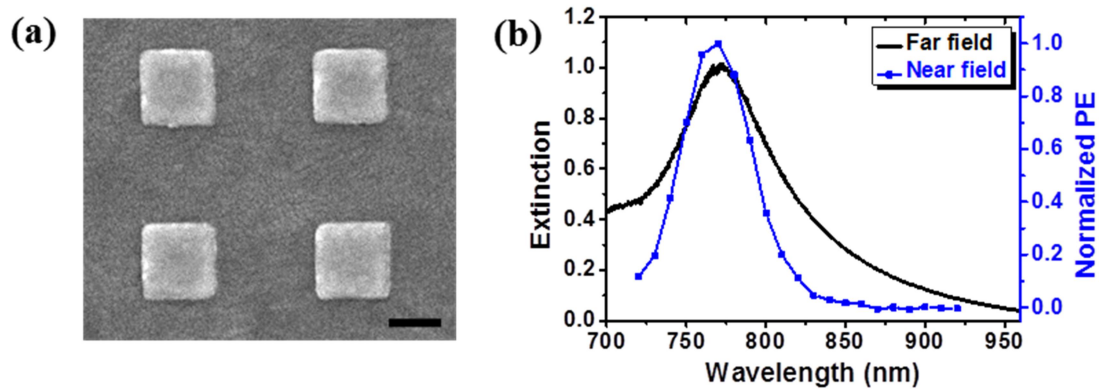


Figure 4.3 (a) SEM image of the Au nanoblock structures with the pitch size of 400 nm. The scale bar is 100 nm. (b) Far- (black) and near-field (blue) spectra of Au nanoblock structures with the pitch size of 400 nm.

The Au nanoblock structures were fabricated by EBL with different pitch size range from 400 nm to 1500 nm. The nanoblock structures have the size of $180 \times 180 \text{ nm}^2$, with a thickness of 30 nm. Figure 4.3 (a) shows the SEM image of the Au nanoblock structures with the pitch size of 400 nm. The near-field properties of plasmonic nanostructures in this study were also performed by PEEM with a wavelength-tunable (720 nm to 920 nm) fs laser as the excitation source. A nominal field of view (FOV) of $10 \mu\text{m}$ was primarily used in this experiment. The far- and near-field spectra of nanoblock structures were shown in Figure 4.3 (b). The black curve represents the

far-field extinction spectrum while the blue curve represents the near-field spectra obtained from PEEM. The dipole LSPRs can be observed at approximately 770 nm in both far-field and near-field spectra.

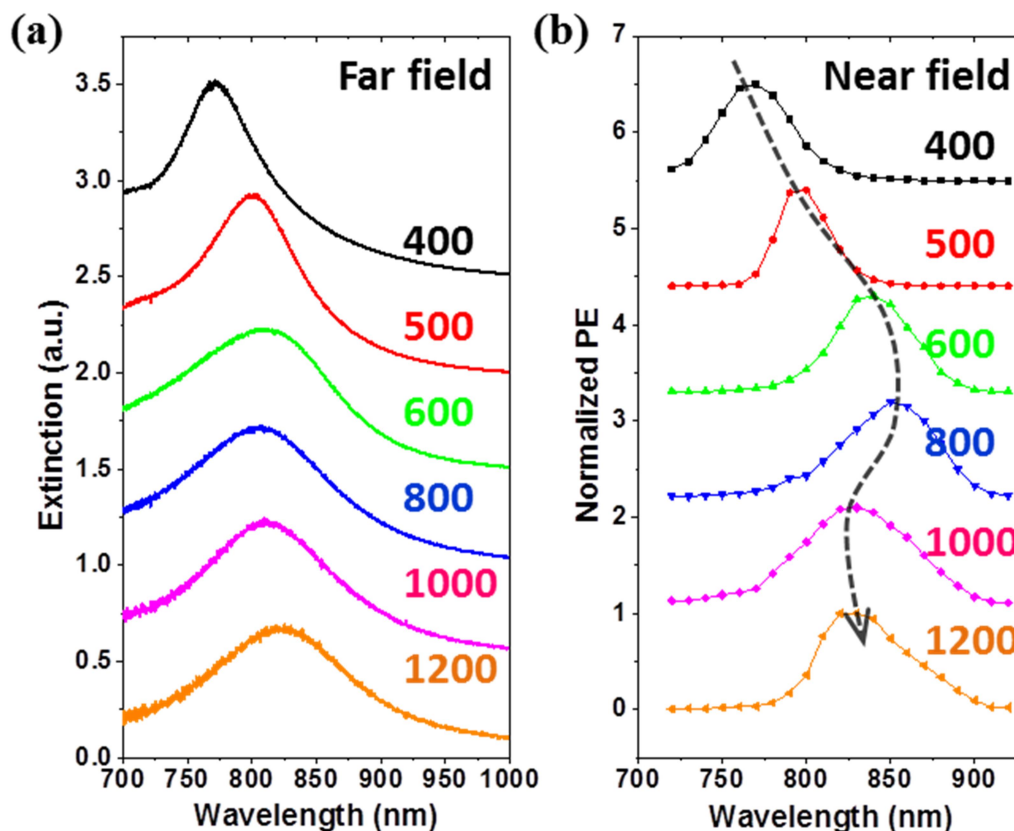


Figure 4.4 (a) Experimental far-field extinction spectra on Au nanoblock structures for different pitch sizes. For a clear view, each curve is normalized to the extinction strength of the curve for a pitch size of 400 nm in term of the same NP density, and an offset of 0.5 is applied. (b) Experimental near-field extinction spectra on Au nanoblock structures for different pitch sizes. Each curve is normalized by its maximum photoemission intensity, and an offset of 1 is applied. The black dashed arrow highlights the peak shift tendency as the pitch size increases.

Far- and near-field spectra for pitch sizes of 400 nm, 500 nm, 600 nm, 800 nm, 1000 nm and 1200 nm are shown in Figure 4.4 (a) and (b), respectively. In far-field extinction spectra, a slight shift of the plasmon peak wavelength can be observed. On contrast, in near-field spectra, the near-field peaks red shifted dramatically first, then blue shifted slightly, and finally, red shifted again. These shift tendencies can also be clearly observed following the black dashed arrow. A dramatic red shift can be observed when

the pitch size changing from 400 nm to 600 nm. This is in good agreement with the previous research on metallic nanostructures in square lattices. The research interpreted such phenomena as the radiative dipole coupling as $1/d$ dependence.^{12, 13, 15} The oscillation of the dipole plasmon peak wavelength was observed when the pitch size is larger than 600 nm. This attributed to the grating effect.

For 2D square grating of metallic NPs, there is a critical pitch size, d_c , it decided a new diffractive radiation order emerges for a given wavelength, λ . When $d < d_c$, the diffraction is evanescent. While increasing the pitch size, the diffraction order switches from the evanescent mode to the radiant mode, it alternates the damping property of the LSPR since the emergence of the new radiant mode increases the radiative loss. For normal incidence onto the sample on a substrate; there are two values of d_c for the first-order diffraction. One is λ/n which corresponds to radiation onto the substrate. Another one is λ which correspond to the radiation into the free space. The emergence of several values of d_c enable the LSPR peak wavelength to oscillate when the pitch size is larger than the first critical pitch size, λ/n . Such phenomena have been reported previously based on far-field spectroscopic measurements of simple nanostructure array.^{12, 13} The experimental results of the near-field properties in this study also revealed such behaviors. However, in the far-field spectra, the spectral response is less sensitive to the pitch size compared with near-field spectra. This is due to the specific light incidence angles during the far-field extinction spectra measurements. During the far-field spectra measurement by FTIR, light was focused on the sample by a Cassegrainian objective lens, which provided angles of incidence between 16° and 32° . The spectral properties of the plasmonic nanostructures in arrays are very sensitive to the angle of the incidence light.

4.4.2 Far-field coupling and grating effect in coupled dolmen structures

In chapter 3, the near-field properties of Au dolmen structures have been systematically investigated using PEEM. The anti-bonding plasmon mode and bonding plasmon mode have been spectrally and spatially resolved by near-field spectra and near-field mapping, respectively. The anti-bonding plasmon mode and bonding plasmon mode are generated from the plasmon hybridization through the strong interaction between the dipole plasmon mode in monomer part and quadrupole-like mode in dimer part. The hybridized anti-bonding mode generated from the hybridized anti-bonding state, the charge distribution in the monomer and dimer parts leads to a repulsive Coulomb force at the gap area. It makes the charges in the monomer easier concentrate at the two upper corners. While the hybridized bonding mode was generated from the hybridized bonding state, the charge distribution in the monomer and dimer parts leads to an attractive Coulomb force at the gap area. In this case, the charges in the monomer easier concentrated at the lower corners of the monomer. These formations of the two hybridized plasmon modes lead to the two hybridized plasmon peaks in both far- and near-field spectra. Even a quadrupole-like mode in dimer part can be resolved from the spatially resolved near-field intensity spectra, however, it only weak contribute to the near field. On the contrary, the two hybridized plasmon modes dominate the near field.

The far- and near-field properties will be more interesting in such kind of complex coupled plasmonic nanostructure systems with different pitch sizes which may exhibit the far-field coupling and the grating effect. In previous investigation, the pitch size of the Au dolmen structures was settled at 1 μ m. To better understanding the far-field coupling and the grating effect in complex coupled plasmonic nanostructures, the Au dolmen structures with several different pitch sizes were investigated. The Au dolmen structures have been fabricated by EBL with pitch sizes ranging from 400 nm to 1500 nm. The sizes of the dolmen structures were same as investigated in chapter 3 (The planar nanorod monomer had a dimension of 100 \times 150 nm². The dimension of each

nanorod in the planar nanorod dimer was $80 \times 140 \text{ nm}^2$. The edge-to-edge distance between two nanorods in the dimer part was 70 nm, and the gap distance between the monomer part and dimer part was chosen to be 25 nm.). The structures with the smallest pitch size (400 nm) were thought large enough to avoid the near-field interaction between the nearby particles.¹⁷

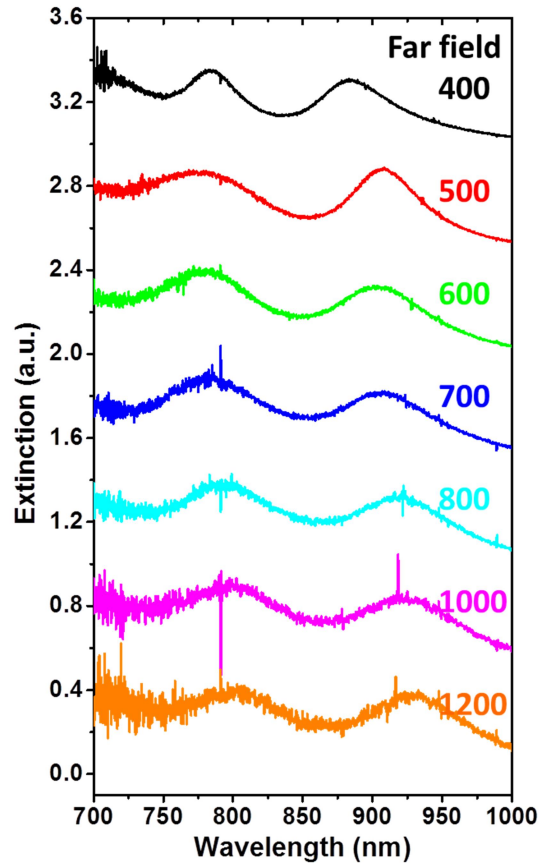


Figure 4.5 Experimental far-field extinction spectra of Au dolmen structures with different pitch sizes (400 nm, 500 nm, 600 nm, 700 nm, 800 nm, 1000 nm, 1200 nm) under horizontal polarization (the electric field vector is perpendicular to the symmetrical axis of the dolmen). For a clear view, each curve is normalized to the extinction strength of the curve for a pitch size of 400 nm in term of the same NP density, and an offset of 0.5 is applied.

The experimental far-field extinction spectra for the pitch sizes of 400 nm, 500 nm, 600 nm, 700 nm, 800 nm, 1000 nm, 1200 nm are shown in Figure 4.5. The polarization of the excitation light is horizontal polarization which the electric field vector is perpendicular to the symmetry axis. In this study, only the case under horizontal

polarization was investigated. In the figure, the two hybridized plasmon modes localized at approximately 780 nm and 900 nm can be clearly observed for each pitch size. The appearance of the extinction mode at a short wavelength is attributed to the transverse LSPR mode of the dimer rods. As changing the pitch sizes, the peak wavelengths slightly shift. The small shift values are different from the results of the investigation about the grating effect on simple nanostructures.

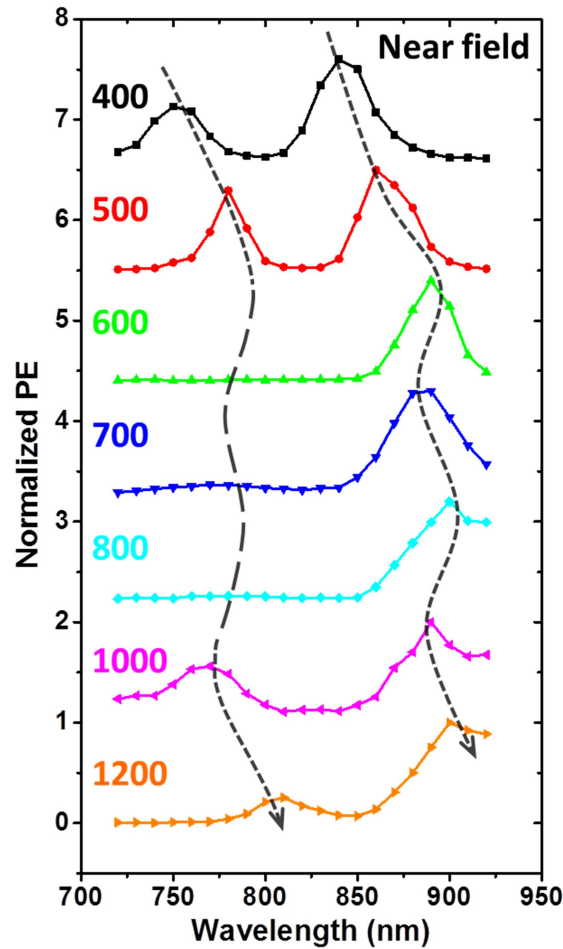


Figure 4.6 Experimental near-field extinction spectra of Au dolmen structures with different pitch sizes (400 nm, 500 nm, 600 nm, 700 nm, 800 nm, 1000 nm, 1200 nm) under horizontal polarization (the polarization vector along perpendicular to the symmetrical axis of the dolmen). Each curve is normalized by its maximum photoemission intensity, and an offset of 1 is applied. The black dashed line shows the peak shift tendency as the pitch size varies. The black dashed arrow in highlights the peak shift tendency as the pitch size increases.

Figure 4.6 shows the near-field spectra of Au dolmen structures for the pitch sizes of

400 nm, 500 nm, 600 nm, 700 nm, 800 nm, 1000 nm, 1200 nm. The peak wavelengths of the two hybridized plasmon modes were nearly identical for all pitch sizes under normal incidence. However, in near-field spectra, the two hybridized plasmon peaks red shifted first, then blue shifted slightly and red shifted slightly again as the pitch size increased. The black arrows also guided the peak shifts tendency. These shifts are similar to the results of previous investigation on the grating effect in plasmonic nanostructures through the far-field measurements.^{12, 13} Furthermore, for some specific pitch sizes (600 nm, 700 nm, 800nm), the shorter-wavelength peaks show weak intensity. It means that the shorter-wavelength peaks were dramatically suppressed with these specific pitch sizes.

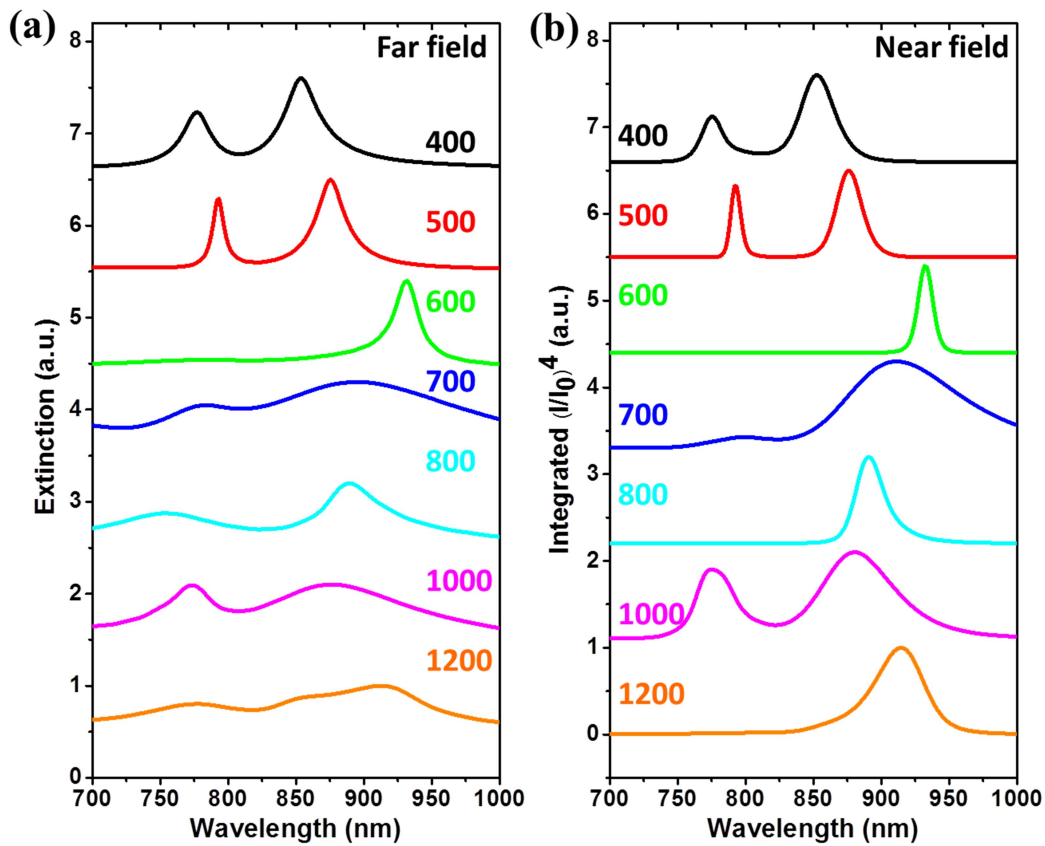


Figure 4.7 Simulated far- and near-field spectra of Au dolmen structures for different pitch sizes under normal excitation by FDTD simulation. (a) Far-field extinction spectra for different pitch sizes. (b) Near-field spectra for different pitch sizes. The normalized integrated value, $(I/I_0)^4$, over an area of $320 \text{ nm} \times 320 \text{ nm}$ at the interface between the dolmen structure and the substrate is shown for better comparison with the PEEM measurements, considering the nonlinearity of the multiphoton photoemission as 4. The

simulated far-field and near-field spectra are all normalized by the maximum extinction or PE intensity of each curve, and an offset of 1 is applied.

To understand the different observation in the spectra in far and near field, the simulated far- and near-field spectra have been performed. They were done by the FDTD simulation under the normal incidence light excitation. Figure 4.7 (a) and (b) shows the far- and near-field spectra of Au dolmen structures with pitch size of 400 nm, 500 nm, 600 nm, 700 nm, 800 nm, 1000 nm, 1200 nm, respectively. The results of simulated near-field spectra reproduced the experimental observations qualitatively. However, the simulated far-field spectra on the pitch size were not similar to the experimental far-field result; on the contrary, they were similar to the experimental near-field spectra.

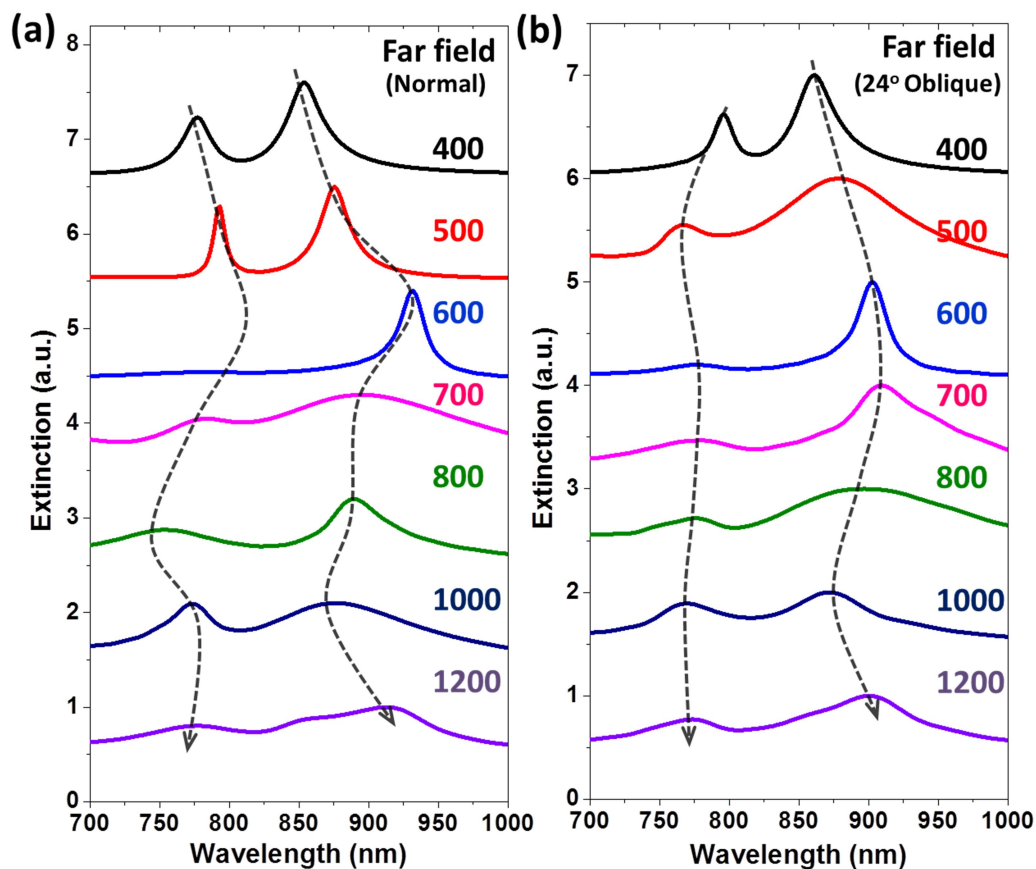


Figure 4.8 Far-field extinction spectra simulated by FDTD with the normal incidence excitation (a) and the oblique incidence excitation at 24° incidence angle (b). The black dashed arrow in highlights the peak shift tendency as the pitch size increases.

The difference between the experimental result and the numerical simulations in the

far field are resulted from the different angles of incidence of the light. During the far-field spectra measurement by FTIR, light was focused on the sample by a Cassegrainian objective lens, which provided angles of incidence between 16° and 32° . However, in the FDTD simulations, light was irradiated onto the structures under normal incidence. To verified the influence of the incidence angles, far-field extinction spectra under oblique incident excitation has been simulated. Figure 4.8 compared with the simulation results between the normal incidence (a) and oblique incidence at 24° (b). It is found that the LSPR peak wavelengths are less sensitive to the pith size for the oblique incidence compared to those for the normal incidence. In these simulated results, the anti-bonding mode at the pitch size of 600 nm can be seen more clearly at the oblique incidence. The spectral properties of the plasmonic nanostructures in arrays are very sensitive to the angle of the incidence light. This accounts for the difference in the properties of the far-field extinction spectra in the experiments and the simulations.

Furthermore, if compared with the spectral response on the Au nanoblock structures, the two hybridized modes in the dolmen structures affected by the pitch size are similar to the spectra response on nanoblock structures. This further demonstrated that the anti-bonding and bonding plasmon modes are either bright or superradiant plasmon mode. Because they are strongly modified by the grating effect which mainly due to the interaction between the scattering fields.

In dolmen structures, the dipole plasmon mode in monomer part induces the quadrupole-like mode in dimers, and the quadrupole-like mode interacts again with the dipole mode resulting in the two hybridized plasmon modes. The dipole plasmon mode is a bright superradiant plasmon mode while the quadrupole mode is dark subradiant plasmon mode. To better understand the grating effect in the complex Au dolmen structures, the spectral properties of quadrupole mode are also very important. Next, the grating effect on heptamer structures which exhibit a subradiant plasmon mode will be discussed.

4.4.3 Far-field coupling and grating effect in complex heptamer structures

To further explore the grating effect in complex coupled plasmonic systems in near field, the complex plasmonic heptamer structures have been investigated. Plasmonic heptamer structures have been investigated with exhibiting Fano resonance by several groups.¹⁸⁻²¹ In heptamer structures, the dipole LSPRs of the central nanodisks and the outer nanodisks are hybridized to a bonding bright mode with same phase in all nanodisks and an anti-bonding dark mode with the center nanodisks and outer nanodisks out of phase. The bonding mode and anti-bonding mode interference and induce the Fano resonance.^{19, 20} As introduced in chapter 3, Halas et al. demonstrated that SERS signals are most enhanced when the wavelength of the pump laser and the Raman Stokes mode of interest overlap the Fano dip wavelength.¹⁸ Additionally, their calculations performed that the wavelength of the Fano dip in the far-field scattering spectrum is very close to the wavelength of the maximum in the near-field enhancement spectrum. Their results indicated that the subradiant plasmon mode dominates the near-field enhancement.

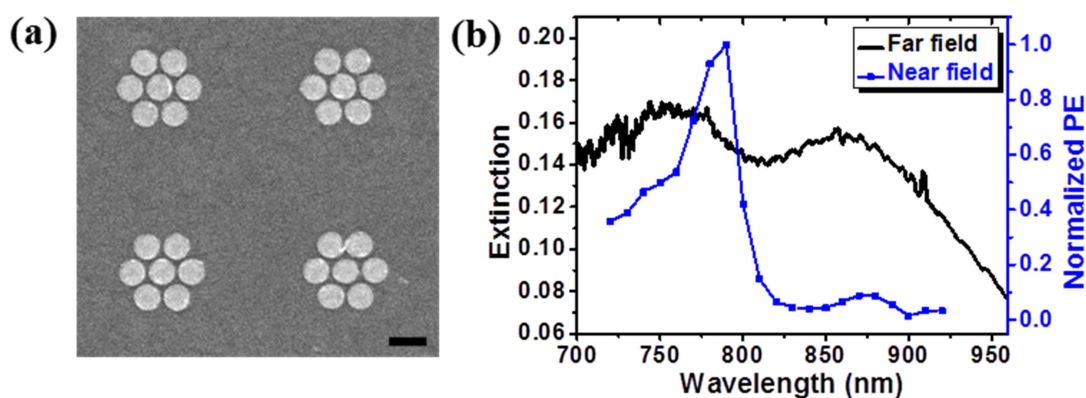


Figure 4.9 (a) SEM image of Au heptamer structures with the pitch size of 1000 nm. The scale bar is 200 nm. (b) Far-field extinction spectrum (black) and near-field spectrum (red) of Au heptamer structure with 1000 nm pitch size under horizontally polarized light.

In this study, Au heptamer structures were fabricated by EBL and the comprised circles with 140 nm in diameter and the gaps of 20 nm between them. Figure 4.9 shows

the SEM image of the heptamer array with the pitch size of 1000 nm. The far-field extinction spectrum (black) and near-field spectrum (blue) of Au heptamer structure with 1000 nm pitch size under horizontally polarized light are shown in Figure 4.9 (b), respectively. The Fano-like line-shape can be clearly observed in the far-field extinction spectrum. A dip located at 800 nm can be also identified. The near-field spectrum performs only one peak, which is located at approximately 780 nm, close to the dip wavelength of the far-field spectrum. These results indicate that in a heptamer system, the subradiant plasmon mode dominates the near-field enhancement, and the interference between the superradiant plasmon mode and subradiant plasmon mode leads to the Fano resonance resulting in the far-field line-shape.

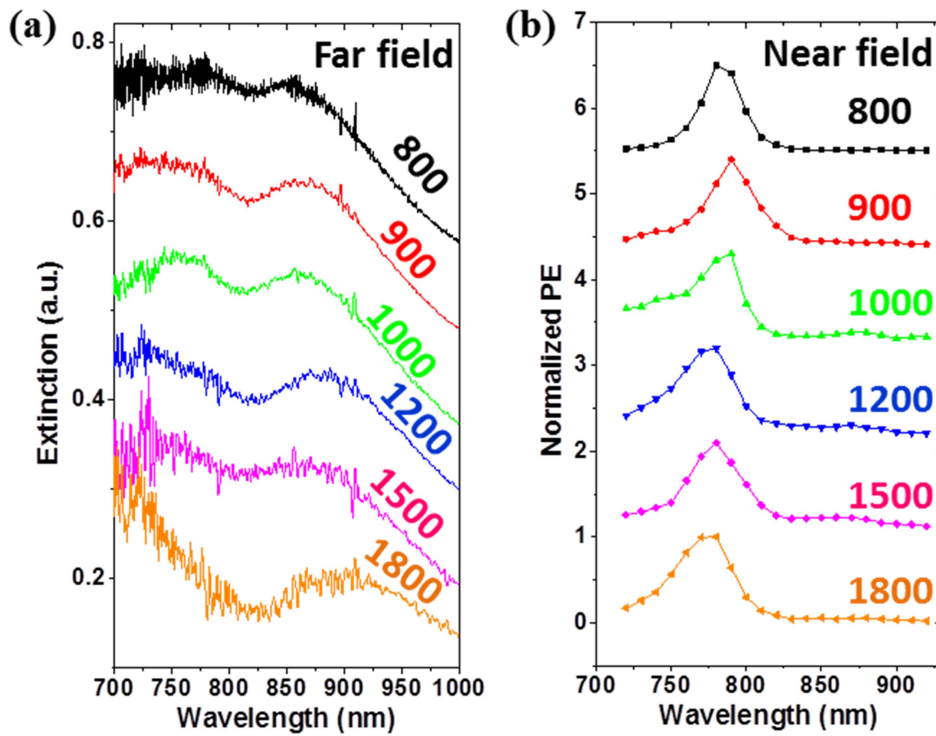


Figure 4.10 Experimental far-field extinction spectra (a) and near-field spectra (b) of Au heptamer structures for the different pitch sizes. In heptamer structures, to avoid near-field interaction between two adjacent units, the smallest pitch size was set to 800 nm. A pitch size of 1800 nm was also investigated.

The far-field extinction spectra and the near-field spectra of the heptamer structures with different pitch sizes are shown in Figure 4.10 (a) and (b), respectively. The smallest

pitch size was set to 800 nm is to avoid the near-field interaction between two adjacent units, since the entire heptamer structures was large. In the far-field extinction spectra, the pitch size ranged of 800 nm, 900 nm, 1000 nm, 1200 nm, 1500 nm, 1800 nm. The dip wavelengths in far-field spectra are almost constant when changing the pitch size. And each curve in near-field spectra shows only one dominant near-field enhancement peak around the dip wavelength in far-field spectra. These observations are different from the behaviors observed in Au dolmen structures and Au nanoblock structures. It is because of that in Au heptamer structure system, the superradiant plasmon mode dominates the near-field enhancement. The properties of the superradiant plasmon mode make it have very low scattering loss. Hence, this plasmon mode is dominated by absorption rather than scattering; therefore, it is insensitive to the pitch size.

4.4.4 Summary and discussions

The grating effects in plasmonic arrays of dolmen structures, nanoblock structures, and heptamer structures have been investigated using the near-field PEEM measurements. Figure 4.11 shows the experimental (a) and simulated (b) plasmon resonant wavelength as a function of the pitch size for different nanostructures, for comprehensive comparison. The black and green curves correspond to the hybridized bonding plasmon mode and anti-bonding mode in dolmen structure, respectively. The red curve represents the dipole plasmon mode in nanoblock structures, and the blue curve corresponds to the subradiant plasmon mode supports on the heptamer structures. Note that, for the anti-bonding plasmon mode it was strongly suppressed for the pitch sizes of 600 nm and 800 nm, so that, the corresponding data points are missing. The two hybridized plasmon modes (black and green) of the dolmen and the dipole plasmon mode (red) in nanoblock structure exhibited the same dependence on the pitch size. As the pitch size increasing, the plasmon modes red shifted dramatically first, and then oscillated. The initial red shift can be contributed to far-field dipole-dipole coupling.¹²⁻¹⁵

The resonance wavelengths of near-field plasmon mode (blue) in heptamer structures varied only slightly as the pitch size increasing. For all four plasmon modes, there is good agreement between the experiments and simulations. In Figure 4.11 (b), there are three dashed lines, namely λ/n , λ , and $2\lambda/n$. The three lines described the maximum wavelengths for each curve. They are corresponding to the grating constant in different situations. The three situations are the first-order grazing diffraction in the substrate, λ/n , first-order grazing diffraction in free space, λ , and the second-order grazing diffraction in the substrate, $2\lambda/n$. The plasmon peak oscillations depend on the pitch size all followed this three grating effect mode. It can be concluded that for the two hybridized plasmon mode and dipole plasmon mode, not only the far-field spectra but also the near-field spectra are affected by far-field coupling and the grating effect.¹³⁻¹⁵ The slight shift of the plasmon mode in heptamer structures demonstrated that the superradiant plasmon mode is less sensitive to the far-field coupling and grating effect.

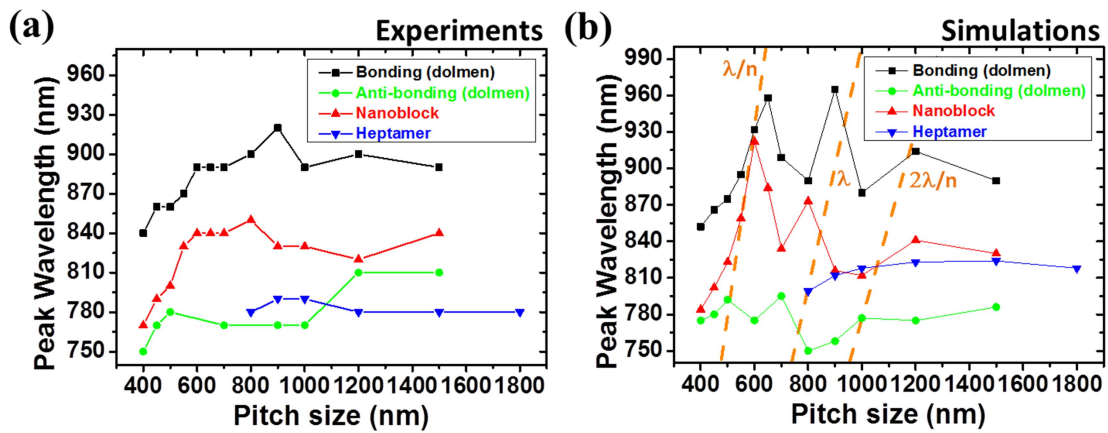


Figure 4.11 Experimental (a) and simulated (b) near-field plasmon resonant wavelength as a function of the pitch size for different plasmon modes in different nanostructures. The colors represent the different plasmon mode, the hybridized bonding mode in dolmens (black), the hybridized anti-bonding mode in dolmens (green), the bright dipole mode in nanoblocks (red), and the subradiant mode in heptamers (blue). The gray dashed lines in (b) show the three modes of the grating effect: first-order grazing diffraction on the substrate, λ/n , first-order grazing diffraction in free space, λ , and second-order grazing diffraction in the substrate, $2\lambda/n$.

The dolmen structures and heptamer structures have been investigated in this study, and they exhibit absolutely different near-field spectra response. Among this thesis, it is

assumed that the near-field spectra can be used to distinguish the contribution to the near-field enhancement of the plasmon hybridization and Fano resonance, which are difficult to be distinguished only from the far-field extinction or scattering spectra. In dolmen structures, two hybridized plasmon mode dominate the near-field enhancement, while in heptamer structures the subradiant plasmon mode dominates the near-field enhancement. The results indicate the far-field line shapes are decided by plasmon hybridization in dolmen structure and the Fano resonance in heptamer structures. Furthermore, in this study, the different roles of the grating effect in dolmen and heptamer structures further prove the difference in the near-field properties of these two structures. In dolmen structures, the hybridized anti-bonding mode and bonding mode dominate the near field; however, both hybridized plasmon modes are superradiant mode and can interact with other structures within the array through the far-field coupling and grating effect. In heptamer structures, subradiant plasmon mode dominates the near field; the subradiant plasmon mode is very weak to the far-field coupling and is insensitive to the grating effect.

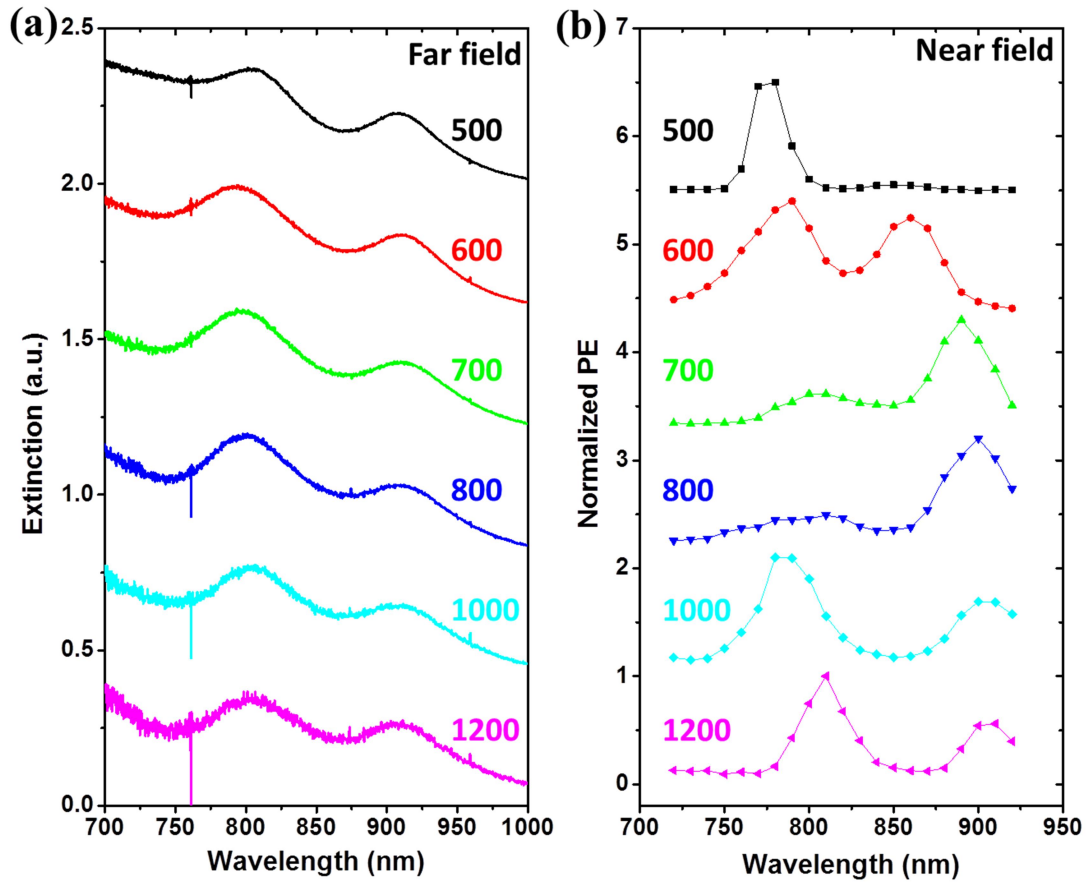


Figure 4.12 (a) Far-field extinction spectra of Au dolmen structures for different pitch sizes, in which the anti-bonding mode is much stronger than the bonding mode. Each curve is normalized to the extinction strength of the curve for a pitch size of 400 nm in term of the same NP density, and an offset of 0.5 is applied. (b) Near-field spectra of Au dolmen structures same in (a). In this group of the dolmen arrays, the near-field anti-bonding peak in the pitch size of 600 nm to 800 nm arrays can still be observed although it has been strongly suppressed by grating effect.

As discussed above, the two hybridized plasmon modes in dolmen structures performed different sensitivity to the pitch size, especially, only the anti-bonding plasmon mode strongly suppressed in the pitch size from 600 nm to 800 nm. For these pitch sizes, the anti-bonding mode seemed to vanish. Since the relative strengths between the anti-bonding mode and bonding mode of dolmen structures can be controlled by slightly adjusting the geometry. Figure 4.12 shows the far- (a) and near-field spectra (b) of Au dolmen structures for different pitch sizes, in which the anti-bonding mode was much stronger than the bonding mode in the far-field spectra. In

the figure, the anti-bonding mode can be clearly identified for all pitch sizes. However, it was significantly attenuated for the pitch sizes between 600 nm and 800 nm as shown in the near-field spectra. The difference responses between anti-bonding mode and bonding mode may be understood based on the formation of these two hybridized mode. The anti-bonding mode is generated from the repulsive Coulomb force between the monomers and the dimers resulting in the maximum near-field enhancement located at the two outside corners of the monomer and give a higher energy peak in the shorter wavelength range. The bonding mode is generated from the attractive Coulomb force between the monomers and dimers resulting in the maximum near-field enhancement located at the two down side corners of the monomer near the gap and give a lower energy peak in the longer wavelength range. The anti-bonding mode is unstable compared to the bonding mode. Therefore, the anti-bonding plasmon mode may be affected by the far-field coupling and grating effect more strongly. Nevertheless, details of the mechanism underlying the attenuation of the anti-bonding mode due to the far-field coupling and grating effect need further investigation.

4.5 Conclusions

In this chapter, the far-field coupling and grating effect on different types of Au nanostructures arrays have been investigated using near-field measurements by PEEM. The two plasmon hybridization in complex coupled dolmen structures, dipole plasmon mode in simple nanoblock structures and subradiant plasmon mode in complex coupled heptamer structures were studied and compared. The two hybridized plasmon modes on dolmen structures exhibit the dependence of their near-field spectral properties depend on the pitch size in a manner similar to the dipole mode on the nanoblock structures. The plasmon peaks were found red shifted first, and oscillated due to the far-field coupling and grating effect as the pitch size increasing in the two hybridized plasmon modes and dipole plasmon mode. In contrast, the spectral response of the plasmon mode in heptamer structures exhibit insensitive behaviors to the far-field coupling and grating effect. Furthermore, the plasmon hybridization and Fano resonance supports on dolmen structures and heptamer structures, respectively, have been successfully distinguished through the near-field spectra. This investigation deepens our understanding of far-field coupling and especially the grating effect in complex plasmonic nanostructures and may help for optimizing the design of plasmonic nanostructures for wide applications.

4.6 References

1. Halas, N. J.; Lal, S.; Chang, W. S.; Link, S.; Nordlander, P., Plasmons in Strongly Coupled Metallic Nanostructures. *Chemical Reviews* **2011**, 111, 3913-3961.
2. Taubert, R.; Ameling, R.; Weiss, T.; Christ, A.; Giessen, H., From Near-Field to Far-Field Coupling in the Third Dimension: Retarded Interaction of Particle Plasmons. *Nano Letters* **2011**, 11, 4421-4424.
3. Maier, S. A.; Atwater, H. A., Plasmonics: Localization and Guiding of Electromagnetic Energy in Metal/Dielectric Structures. *Journal of Applied Physics* **2005**, 98, 10.
4. Ritchie, R. H.; Arakawa, E. T.; Cowan, J. J.; Hamm, R. N., Surface-Plasmon Resonance Effect in Grating Diffraction. *Physical Review Letters* **1968**, 21, 1530.
5. DeJarnette, D.; Roper, D. K.; Harbin, B., Geometric Effects on Far-Field Coupling between Multipoles of Nanoparticles in Square Arrays. *Journal of the Optical Society of America B-Optical Physics* **2012**, 29, 88-100.
6. Sanchez-Gil, J. A.; Maradudin, A. A., Near-Field and Far-Field Scattering of Surface Plasmon Polaritons by One-Dimensional Surface Defects. *Physical Review B* **1999**, 60, 8359-8367.
7. Wang, X. L.; Gogol, P.; Cambriel, E.; Palpant, B., Near- and Far-Field Effects on the Plasmon Coupling in Gold Nanoparticle Arrays. *Journal of Physical Chemistry C* **2012**, 116, 24741-24747.
8. Vecchi, G.; Giannini, V.; Rivas, J. G., Shaping the Fluorescent Emission by Lattice Resonances in Plasmonic Crystals of Nanoantennas. *Physical Review Letters* **2009**, 102.
9. Jain, P. K.; El-Sayed, M. A., Plasmonic Coupling in Noble Metal Nanostructures. *Chemical Physics Letters* **2010**, 487, 153-164.
10. Jensen, T. R.; Duval, M. L.; Kelly, K. L.; Lazarides, A. A.; Schatz, G. C.; Van Duyne, R. P., Nanosphere lithography: Effect of the External Dielectric Medium on the Surface Plasmon Resonance Spectrum of a Periodic Array of Silver Nanoparticles. *Journal of Physical Chemistry B* **1999**, 103, 9846-9853.
11. Meier, M.; Wokaun, A.; Liao, P. F., Enhanced Fields on Rough Surfaces - Dipolar Interactions among Particles of Sizes Exceeding the Rayleigh Limit. *Journal of the*

Optical Society of America B-Optical Physics **1985**, 2, 931-949.

12. Lamprecht, B.; Schider, G.; Lechner, R. T.; Ditlbacher, H.; Krenn, J. R.; Leitner, A.; Aussenegg, F. R., Metal Nanoparticle Gratings: Influence of Dipolar Particle Interaction on The Plasmon Resonance. *Physical Review Letters* **2000**, 84, 4721-4724.

13. Felidj, N.; Laurent, G.; Aubard, J.; Levi, G.; Hohenau, A.; Krenn, J. R.; Aussenegg, F. R., Grating-Induced Plasmon Mode in Gold Nanoparticle Arrays. *Journal of Chemical Physics* **2005**, 123, 221103.

14. Pinchuk, A. O.; Schatz, G. C., Nanoparticle Optical Properties: Far- and Near-Field Electrodynamic Coupling in a Chain of Silver Spherical Nanoparticles. *Materials Science And Engineering B-Advanced Functional Solid-State Materials* **2008**, 149, 251-258.

15. Haynes, C. L.; McFarland, A. D.; Zhao, L. L.; Van Duyne, R. P.; Schatz, G. C.; Gunnarsson, L.; Prikulis, J.; Kasemo, B.; Kall, M., Nanoparticle Optics: The Importance of Radiative Dipole Coupling in Two-Dimensional Nanoparticle Arrays. *Journal of Physical Chemistry B* **2003**, 107, 7337-7342.

16. You, Y. M.; Du, C. L.; Ma, Y.; Kasim, J.; Yu, T.; Shen, Z. X., Effect of Near-Field Coupling on Far-Field Inelastic Scattering Imaging of Gold Nanoparticles. *Nanotechnology* **2008**, 19, 395705.

17. Yan, C.; Martin, O. J. F., Periodicity-Induced Symmetry Breaking in a Fano Lattice: Hybridization and Tight-Binding Regimes. *ACS Nano* **2014**, 8, 11860-11868.

18. Ye, J.; Wen, F. F.; Sobhani, H.; Lassiter, J. B.; Van Dorpe, P.; Nordlander, P.; Halas, N. J., Plasmonic Nanoclusters: Near Field Properties of the Fano Resonance Interrogated with SERS. *Nano Letters* **2012**, 12, 1660-1667.

19. Lassiter, J. B.; Sobhani, H.; Fan, J. A.; Kundu, J.; Capasso, F.; Nordlander, P.; Halas, N. J., Fano Resonances in Plasmonic Nanoclusters: Geometrical and Chemical Tunability. *Nano Letters* **2010**, 10, 3184-3189.

20. Hentschel, M.; Saliba, M.; Vogelgesang, R.; Giessen, H.; Alivisatos, A. P.; Liu, N., Transition from Isolated to Collective Modes in Plasmonic Oligomers. *Nano Letters* **2010**, 10, 2721-2726.

21. Frimmer, M.; Coenen, T.; Koenderink, A. F., Signature of a Fano Resonance in a Plasmonic Metamolecule's Local Density of Optical States. *Physical Review Letters* **2012**, 108, 077404.

Chapter 5

Conclusions and future perspectives

5.1 Conclusions

This thesis aimed at the near-field properties of complex coupled metallic nanostructures which exhibit striking optical properties such as plasmon hybridization and Fano resonance. The near-field properties of different kinds of simple and complex metallic nanostructures have been investigated using photoemission electron microscopy (PEEM). From the high spatial resolution PEEM images for different structures with different wavelength excitation, the near-field enhancement distribution and the near-field photoemission intensity spectra can be obtained. These measurements help for better understanding the plasmon modes supported by different kinds of metallic nanoparticles. The temporal domain can also be investigated by time-resolved PEEM for better understanding the dynamics of the plasmon modes. Furthermore, the thesis emphasized that the crossover between the plasmon hybridization and Fano resonance in terms of their near-field properties. The near-field photoemission intensity spectra allowed to distinguish the contribution to the near-field enhancement from the two phenomena. I believe that the investigations in this thesis deepen our understanding to the near-field properties of the plasmonic nanostructures, and may help us for better understanding plasmon coupling in complex plasmonic nanostructures.

In the chapter 1, I introduce the concept of surface plasmon resonance and particularly I discuss the optical properties of localized surface plasmon resonances (LSPRs). Plasmon coupling of LSPRs in both near-field and far-field regions are introduced. Two striking properties of coupled plasmonic nanostructures as plasmon

hybridization and Fano resonance are also introduced. In addition, several approaches which can pinpoint the near field are introduced and compared with their advantages and disadvantages.

In the chapter 2, the application of PEEM in plasmonics has been demonstrated using the simple Au nanoblock structures as the example. Most of the experimental details related to this thesis are introduced. The near-field mapping and near-field spectra are the two fundamental applications of PEEM. With the help of these two applications, it is demonstrated that the quadrupole and dipole LSPR modes can be selectively excited by changing the polarization of the oblique incident light. Furthermore, time-resolved PEEM allows to investigate the ultra-fast dynamics of the LSPRs. In particular, it is experimentally proved that the quadrupole LSPR mode has longer dephasing time than the dipole plasmon mode. The applications of PEEM to investigate the near field have been demonstrated as a promising approach to investigate the plasmonic systems both in spatial domain and temporal domain.

In the chapter 3, the near-field properties of a complex coupled Au dolmen structures have been experimentally investigated using PEEM. The spatial evolution of the near-field patterns revealed the near-field plasmon coupling occurring in the coupled dolmen system. The evolution of near-field mapping with high spatial resolution under different wavelength excitation presented the coupled anti-bonding and bonding plasmon modes which hybridized from the interaction between a dipole plasmon mode in the monomer part and a quadrupole mode in the dimer part. It is found that the two hybridized plasmon mode dominate the near-field enhancement. Although the quadrupole-like mode in the dimer part can be identified by the spatially resolved near-field spectra, it only contributes weakly to the near-field enhancement. Furthermore, for the first time, it is proposed to employ the near-field spectra to distinguish the plasmon hybridization and Fano resonance.

In chapter 4, the far-field coupling and grating effect on different types of Au nanostructures arrays have been investigated using near-field measurements by PEEM.

The two hybridized plasmon modes on dolmen structures exhibit the dependence of their near-field spectral properties on the pitch size in a manner similar to the dipole mode on the nanoblock structures. The plasmon peaks were found red shifted first, and oscillated due to the far-field coupling and grating effect as the pitch size increasing in the two hybridized plasmon modes and dipole plasmon mode. In contrast, the spectral response of the plasmon mode in heptamer structures exhibit insensitive behaviors to the far-field coupling and grating effect. Furthermore, the plasmon hybridization and Fano resonance supports on dolmen structures and heptamer structures, respectively, have been successfully distinguished through the near-field spectra.

In conclusion, the near-field properties of different plasmon modes supported by different kind of plasmonic nanostructures have been investigated using PEEM. Firstly, the dipole and quadrupole plasmon modes on Au nanoblock structures were investigated and it demonstrated that the dipole and quadrupole plasmon modes can be selectively excited by changing the polarization of the oblique incident light. It is also demonstrated that the quadrupole mode has longer dephasing time than the dipole mode by time-resolved PEEM measurements. Secondly, hybridized anti-bonding and bonding plasmon modes in dolmen structures were revealed by the spatial evolution of near-field intensity distributions (PEEM images) with the excitation wavelengths. It is demonstrated that the plasmon hybridization dominate the near-field enhancement rather than Fano resonance in such dolmen system. Thirdly, the far-field coupling and grating effect on different plasmonic nanostructures revealed that different plasmon mode give different response to the far-field coupling and grating effect. The bright plasmon mode is sensitive to the pitch size while the dark plasmon mode is insensitive to the pitch size. Furthermore, the near-field spectrum was demonstrated that it can be used to distinguish the crossover between the plasmon hybridization and Fano resonance. The results deepen our understanding of the LSPRs on plasmonic nanostructures and may help for optimizing the design of the structures and making development for plasmonic applications.

5.2 Future perspectives

Based on this thesis, the investigations were concentrated on the near-field properties on plasmonic nanostructures. The near-field properties of dipole mode, quadrupole mode and the plasmon coupling such as plasmon hybridization and Fano resonances have been systematically investigated. On the basis of the mechanisms of each plasmon modes, their near-field properties can be different. It was further demonstrated that PEEM can be used for investigating the near-field properties of complex coupled plasmonic nanostructures. According to these investigations by PEEM, near field imaging, near-field spectra, and the time-resolved measurement are the three main applications of PEEM in plasmonics. However, as a new developed technique for investigating the plasmonics, PEEM still have other potential applications.

The further outlook of this thesis study can be extended to:

- (1) The near-field imaging and near-field spectra are the two important properties to value the near-field enhancement for different plasmon modes. In this thesis, the dipole, quadrupole plasmon modes and also the coupling between these two modes have been investigated using nanoblock, dolmen and heptamer structures as examples. However, there are also huge research interests on more complex coupled plasmonic nanostructures which can exhibit much complicated plasmon coupling phenomena by multipolar plasmon modes. Such investigation will help for further understanding the mechanism of plasmon coupling.
- (2) In this study, only the near-field imaging and near-field spectra on complex dolmen and heptamer structures have been investigated. PEEM allows the investigation of the dynamics of the LSPRs by time-resolved PEEM. Therefore, in complex plasmonic nanostructures the dynamics of the LSPRs modes and couplings are also very important for comprehensive understanding the coupled plasmon regime in temporal domain and will help for developing the performance of the plasmonic applications.
- (3) The super high-spatial resolution of PEEM make it possible to reveal the spatially

resolved near-field intensity spectra for different areas in one plasmonic structure, which has been used in this study for resolving a weak quadrupole-like plasmon mode in dimer part of a dolmen structure. Combining this technique with the time-resolved measurements, the dynamics of different plasmon modes coexist in one complex plasmonic structure can be investigated by the spatially time-resolved measurements. The results after comparing with the entire response for the couplings of these modes may reveal much more important information about the dynamics of a single complex coupled plasmonic structure.

(4) The hot electron attracts more and more research attention since a huge number of plasmonic applications are based on it such as photocurrent generation and water splitting system using LSPRs. Till now, in such systems, the electron transfer from metallic nanoparticles to the semiconductor substrate has been theoretically demonstrated. However, the dynamic of the electrons after that is not so clear. On the basis of the spatial and temporal resolution of PEEM as well as the ability in resolving the kinetic energy of the photoemitted electrons, such dynamics of the hot electrons can be potentially investigated by time-resolved PEEM measurements with another two-color pump-probe technique.

PEEM has unimaginable potential applications for investigating the SPR. We look forward to the investigations of the SPR by PEEM to be progressed in the future.

List of Publications

1. **H. Yu**, Q. Sun, J. Yang, K. Ueno, T. Oshikiri, A. Kubo, Y. Matsuo, Q. Gong, H. Misawa,
“Near-Field Spectral Properties of Coupled Plasmonic Nanoparticle Arrays”
Optics Express **2017**, 25(6), 6883-6894.
2. **H. Yu**, Q. Sun, K. Ueno, T. Oshikiri, A. Kubo, Y. Matsuo, H. Misawa,
“Exploring Coupled Plasmonic Nanostructures in the Near Field by Photoemission
Electron Microscopy”
ACS Nano **2016**, 10(11), 10373–10381.
3. Q. Sun, **H. Yu**, K. Ueno, A. Kubo, Y. Matsuo, H. Misawa,
“Dissecting the Few-Femtosecond Dephasing Time of Dipole and Quadrupole
Modes in Gold Nanoparticles Using Polarized Photoemission Electron Microscopy”
ACS Nano **2016**, 10(3), 3835–3842.
4. J. Yang, Q. Sun, **H. Yu**, K. Ueno, H. Misawa, Q. Gong,
“Spatial Evolution of the Near-Field Distribution on Planar Gold Nanoparticles with
the Excitation Wavelength across Dipole and Quadrupole Modes”
Photonics Research **2017**, 5(3), 187-193.